JETP Letters, Vol. 75, No. 8, 2002, pp. 363–367. Translated from Pis'ma v Zhurnal Éksperimental'noĭ i Teoreticheskoĭ Fiziki, Vol. 75, No. 8, 2002, pp. 435–439.

Ionization from a Short-Range Potential under the Action of Electromagnetic Fields of a Complex Configuration

V. N. Rodionov[1]*, G. A. Kravtsova[2], and A. M. Mandel'[1]

[1] *Moscow State Geological Prospecting Academy (MGRA), ul. Miklukho-Maklaya 23, Moscow, 117873 Russia*
**e-mail: physics@msgpa.msgpa.ru*
[2] *Faculty of Physics, Moscow State University, Vorob'evy gory, Moscow, 119899 Russia*
Received December 7, 2001; in final form, March 11, 2002

A transcendent equation for complex energy is derived on the basis of the exactly soluble 3D model of short-range potential and the time-dependent Green's function in a strong electromagnetic field representing the combination of a constant magnetic field and the field of a circularly polarized wave. The parameters of the quasistationary states of an electron in δ potential are calculated with account taken of the action of a strong external field of complex configuration. The possibility of stabilizing the decay of the bound states of spinor and scalar particles by a strong magnetic field is analyzed. The results require revision of the commonly accepted view on the stabilizing role of a strong magnetic field in the ionization of atoms. © *2002 MAIK "Nauka/Interperiodica".*

PACS numbers: 32.80.Fb

Although the ionization of atoms and ions, as well as photoabsorption by crystals in strong electromagnetic fields, has been studied for more than 35 years [1–6], a number of problems that are important for both atomic and solid state physics are not yet adequately understood. In particular, this relates to nonlinear phenomena in strong fields of rather complex configurations. Recently, interest in studying these phenomena has been revived [7–12]. A specific feature of these approaches is that they deal with exactly soluble models and the analytic analysis of the results for electromagnetic fields of arbitrary intensity.

Among the indicated studies, works [9, 10], where the interesting possibility of decreasing the rate of atomic decay with an increase in laser intensity (so-called stabilization regime) was studied, can be highlighted. A similar problem of decreasing the width of a quasienergy level in a magnetic field was analyzed in [7]. It is significant that in the cited works only the *scalar* charged particles were considered, irrespective of the configuration of the electromagnetic field.

In this paper, the exactly soluble 3D model of short-range potential is used to derive analytic expressions describing the action of a strong electromagnetic field of Redmond configuration, i.e., the combination of a constant magnetic field and the field of a circularly polarized wave, on the states of an electron. In particular, the possibility of stabilizing the decay of the bound state of a spinor or scalar particle in a strong magnetic field is analyzed. The approach is based on known exact solutions of quantum equations for charged particles moving in an electromagnetic field of the above-mentioned configuration with the wave propagating along the magnetic field [13].

Let the constant magnetic field H be oriented along the z axis and the wave field specified by amplitude ε, frequency ω, and polarization $g = \pm 1$. The state of an electron with spin oriented along the magnetic field can be described by considering the nonrelativistic limit of corresponding solutions presented in [14]. The propagator $G(2, 1)$ averaged over the electron polarizations in the magnetic field can be represented in the form

$$G(2,1) = \frac{\mathrm{Tr}}{2} G_{i,j}(2,1) = \frac{\sqrt{m\omega_H}}{2(2\pi)^2} \sum_{n=0}^{\infty} \int_{-\infty}^{\infty} dp_2 dp_3 \Psi(2)\hat{\Psi}(1). \quad (1)$$

Omitting the details of standard calculations, we finally write

$$G(r_2, t_2; r_1, t_1) = \left(\frac{m}{2\pi i}\right)^{3/2} \frac{\omega_H}{2\sqrt{t}} \cot\frac{\varphi_H}{2} e^{iS}. \quad (2)$$

Here,

$$S = -\frac{m\xi_0^2}{2\delta}t + \frac{m(z_2 - z_1)^2}{2t} + m\omega_H\left[-\frac{1}{2}(y_2 - y_1)(x_2 + x_1) + \frac{1}{4}((y_2 - y_1)^2 + (x_2 - x_1)^2)\cot\frac{\varphi_H}{2}\right]$$

0021-3640/02/7508-0363$22.00

$$-\frac{\xi_0^2 m\omega_H}{\omega^2\delta^2}\frac{\sin(\varphi/2)\sin\dfrac{(\varphi_H-\varphi)}{2}}{\sin(\varphi_H/2)} \tag{3}$$

$$+ m\xi_0(y_2-y_1) + \frac{\xi_0 m\omega_H}{\omega\delta}\frac{\sin\dfrac{(\varphi_H-\varphi)}{2}}{\sin(\varphi_H/2)}$$

$$\times\left[(y_2-y_1)\cos\frac{\varphi_1+\varphi_2}{2} - (x_2-x_1)\sin\frac{\varphi_1-\varphi_2}{2}\right],$$

where

$$\varphi_H = t\omega_H, \quad \varphi_1 = t_1\omega, \quad \varphi_2 = t_2\omega,$$

$$\varphi = \varphi_2 - \varphi_1 = \omega t;$$

$$\omega H = eH/m; \quad \xi_0 = e\varepsilon/m\omega; \quad \delta = 1 - g\omega H/\omega,$$

and the system of units $\hbar = c = 1$ is used.

By passing to $G(r, t; 0)$, one can easily see that Eqs. (2) and (3) in the limit $H \longrightarrow 0$ yield the well-known relationship for the Green's function in the field of a circularly polarized wave [5, 6]. At $\omega \longrightarrow 0$, the above expressions give results determining the Green's function of an electron moving in mutually perpendicular constant electric and magnetic fields $\boldsymbol{\varepsilon}$ and $\mathbf{H}$, with $\boldsymbol{\varepsilon} \neq \mathbf{H}$. Note that Eqs. (1) and (2) for a scalar charged particle give $G(r, t; r', 0)$ in the form consistent with the similar result obtained in [7].

Generalizing the familiar technique developed in [5–10] for an electromagnetic wave to the case of the Redmond field configuration, one can obtain a transcendent equation relating the complex energy E in an external field to the unperturbed energy E_0 and the parameters ε, ω, and $\mathbf{H}$ of the external field:

$$\sqrt{\beta} = \sqrt{\beta_0} + \frac{1}{\sqrt{4i\pi}}\int_0^\infty du\exp(-i\beta u)R(u), \tag{4}$$

$$R(u) = \frac{(1-\delta)\cot[(1-\delta)u]}{\sqrt{u}}$$

$$\times\exp\left[-i\beta_0\xi^2\frac{u}{\delta}\left(1 - \frac{1-\delta}{\delta}\frac{\sin u\sin(\delta u)}{u\sin(u(1-\delta))}\right)\right] - \frac{1}{u^{3/2}}, \tag{5}$$

where $u = \omega t/2$, $\beta_0 = 2(-E_0)/\omega$, $\beta = 2(-E)/\omega$, and $\xi = e\varepsilon/\omega\sqrt{2m|E_0|}$ is the dimensionless wave intensity related to the Keldysh adiabaticity parameter by the simple expression $\gamma = 1/\xi$.

One can easily see that, in the limit $H \longrightarrow 0$, Eq. (4) leads to the equation coinciding with a similar formula for an electromagnetic wave [5, 6]. In the limit $\omega \longrightarrow 0$, one can obtain from Eq. (4) the expression for the complex energy of an electron bound by a short-range potential well in a constant crossed electromagnetic field of the general form $\boldsymbol{\varepsilon} \perp \mathbf{H}$, $\boldsymbol{\varepsilon} \neq \mathbf{H}$:

$$\alpha = \alpha_0 + \frac{1}{\sqrt{2\pi i}}\int_0^\infty \frac{dt}{t^{3/2}}e^{iEt}$$

$$\times\left\{\nu\cot\nu\exp\left[-i\frac{\varepsilon^2}{8\nu^2}(1-\nu\cot\nu)t^3\right] - 1\right\}, \tag{6}$$

where $\nu = t\omega_H/2$, $\alpha_0 = \sqrt{-2E_0}$, and $\alpha = \sqrt{-2E}$. Note that the replacement of $\cot\nu$ by $(\sin\nu)^{-1}$ in the preexponential factor in Eq. (6) gives the expression presented in [7]. In that work, the ejection of a scalar particle from a short-range potential well by crossed electric and magnetic fields was considered.

An important feature of the procedure of deriving the equations for complex energy $E = E_r - i\Gamma/2$ by the Green's function method [5–10] is the exponential divergence of integrals on the right-hand side of Eqs. (4)–(6) at the upper limit. Therefore, in order to obtain physically justified results, these integrals must be regularized.

Equations similar to Eqs. (4)–(6) were derived by a different method in [12], where the threshold phenomena were studied in a strong external electromagnetic field of the same configuration. This was accomplished using the dispersion relations, while the properties of the Green's functions were not used. To apply this method, it is necessary to prove preliminarily that the energy distribution functions characterizing the cross sections of interacting particles can be appropriately continued to the upper half-plane of the complex energy. This can be proved, e.g., using the optical theorem, i.e., the relationship between the cross section and the imaginary part of the amplitude of forward elastic scattering.

The only difference between the relationships obtained in [12] and Eqs. (4)–(6) is that the right-hand sides of the former contain only real quantities β_0, α_0, and E_0 instead of the complex quantities β, α, and E. In other words, these relationships are explicitly resolved with respect to complex energy. They can be treated as the first step in the iterative method of solving Eqs. (4)–(6). This approach applies to the case under consideration, because the shift of level E_0 is physically meaningful only if the condition

$$|(E - E_0)/E_0| < 1 \tag{7}$$

is satisfied. Therefore, at the first step one can put $E_{(1)} = E_0$, i.e., $\Gamma_{(1)} = 0$ in the exponentials in Eqs. (4) and (6). As a result, the integrals converge and determine the analytic functions in the upper half-plane of complex energy. This allows a complex energy depending on the

unperturbed energy E_0 and on the field parameters to be determined.

The vicinity of zero makes the dominant contribution to the integral in Eq. (6) [15]. Using the computational method described in detail in that paper and passing over to atomic units for fields and binding energies

$$\varepsilon_a = \frac{m^2e^5}{\hbar^4} = 5.14\times10^9 \text{ V/cm};$$

$$H_a = \frac{m^2e^3c}{\hbar^3} = 2.35\times10^9 \text{ G};$$

$$E_0 = -\frac{k^2me^4}{2\hbar^2},$$

we obtain the expressions

$$\left(\frac{-E}{-E_0}\right)^{1/2} = 1 + \frac{h}{\pi\varepsilon^{1/3}}\left\{\frac{1}{2}\mathrm{Ai}(z_0)\mathrm{Bi}(z_0) - \frac{\pi}{4z_0^{1/2}} + \sum_{n=1}^{\infty}\left[\mathrm{Ai}(z_n)\mathrm{Bi}(z_n) - \frac{\pi}{2z_n^{1/2}}\right] + \frac{i}{2}\mathrm{Ai}^2(z_0) + i\sum_{n=1}^{\infty}\mathrm{Ai}^2(z_n)\right\} + \frac{1}{2}\left(\frac{\hbar}{2\pi}\right)^{1/2}\int_0^{\infty}\frac{dt}{t^{1/2}}\left(\coth t - \frac{1}{t}\right)\exp\left(-\frac{2t}{h}\right), \quad (8a)$$

and

$$\left(\frac{-E}{-E_0}\right)^{1/2} = 2 + \frac{h}{\pi\varepsilon^{1/3}} \times \sum_{n=0}^{\infty}\left[\mathrm{Ai}(y_n)\mathrm{Bi}(y_n) - \frac{\pi}{2y_n^{1/2}} + i\mathrm{Ai}^2(y_n)\right] - \frac{1+h/4}{(1+h/2)^{1/2}} + \frac{1}{2}\left(\frac{\hbar}{2\pi}\right)^{1/2} \times \int_0^{\infty}\frac{dt}{t^{1/2}}\left(\coth t - \frac{1}{t}\right)\exp\left[-t\left(1+\frac{2}{h}\right)\right] \quad (8b)$$

for the complex energy of particles with spins $\left(s = \frac{1}{2}\right)$ and 0, respectively. Here, Ai and Bi are the Airy functions [15] which are regular and irregular at infinity, respectively, with augments

$$z_n = (1 + nh)/\varepsilon^{2/3};$$

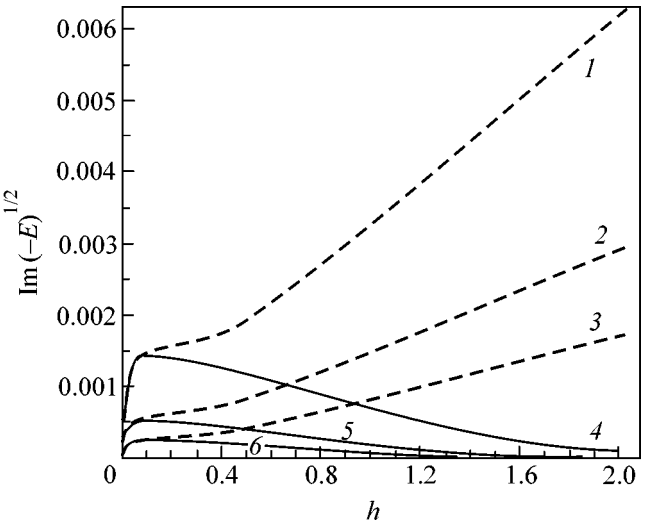

The ionization probability vs. magnetic field h for different values of electric field ε for (solid curves) scalar and (dashed curves) spinor particles.

$$y_n = (1 + h/2 + nh)/\varepsilon^{2/3},$$

where

$$\varepsilon = 2\boldsymbol{\varepsilon}/k^3\boldsymbol{\varepsilon}_a, \quad h = 2H/k^2H_a \quad (9)$$

are the normalized intensities of external fields.

Formulas (8a) and (8b) indicate that the shift and width of a level are determined by only two parameters, ε and h. It should be emphasized that the argument z_0 of the Airy function in the first term in the braces in Eq. (8a) (for a spinor particle) is independent of h, whereas Eq. (8b) does not contain such terms. This circumstance acquires fundamental importance in a sufficiently strong magnetic field.

The figure shows the quantity $\mathrm{Im}(-E)^{1/2}$ as a function of h, as calculated by Eqs. (8a) and (8b). The solid and dashed lines correspond to the scalar and spinor particles, respectively. The calculations were performed for the normalized electric field ε = 0.354, 0.414, and 0.544. It follows from Eq. (9) that, for a fixed electric field at the level $\boldsymbol{\varepsilon} = 0.1\boldsymbol{\varepsilon}_a$, curves *3* and *6* correspond to $k = 0.827$ [^{4}Be(2*s*) and ^{79}Au(6*s*) atoms]; curves *2* and *5*, to $k = 0.785$ [^{5}B(2*p*) atom]; and curves *1* and *4*, to $k = 0.716$ [the value closest to the ^{24}Cr(4*s*) atom].[1] In contrast, for a fixed binding energy [e.g., k = 0.075 for the easily ionized negative helium ion He(2*p*)], curves *1* and *4* correspond to $\boldsymbol{\varepsilon} = 5.9\times10^5$ V/cm; curves *2* and *5*, to $\boldsymbol{\varepsilon} = 4.49\times10^5$ V/cm; and curves *3* and *6*, to $\boldsymbol{\varepsilon} = 3.84\times10^5$ V/cm. It seems likely that such electric fields can be produced by focused laser beams.

[1] Atomic characteristics are taken from [7].

One can easily see that the dependences of $\sqrt{-E}$ on magnetic field h in weak fields are virtually the same for the scalar and spinor particles. Indeed, both Eqs. (8a) and (8b) for $\varepsilon \ll 1$ and $h \ll 1$ yield, regardless of the particle spin,

$$\left(\frac{-E}{-E_0}\right)^{1/2} = 1 + \frac{\varepsilon^2}{32} + \frac{h^2}{48} + \frac{35}{1536}h^2\varepsilon^2 + i\left(\frac{\varepsilon}{8} + \frac{h^2}{24\varepsilon}\right)\exp\left(-\frac{4}{3\varepsilon}\right). \quad (10)$$

This relationship is quite expectable: the probability of ionization in a weak electromagnetic field is exponentially suppressed, while the real correction to energy describes the quadratic Stark shift and the quadratic Zeeman shift of energy levels.

In a strong magnetic field, the imaginary part of the square root of energy for a spinless particle attains a maximum at $h \sim 0.03$–0.05 and then decreases with increasing h. For the above-mentioned He($2p$) ion, the maximum corresponds to the magnetic field $H \sim 6.6 \times 10^2$ G. By contrast, $\mathrm{Im}\sqrt{-E}$ for a particle with spin increases almost linearly with the field at $h > 0.1$.

At $h \gg \varepsilon^{2/3}$ and $\varepsilon \ll 1$, Eqs. (8a) and (8b) give

$$\left(\frac{-E}{-E_0}\right)^{1/2} = 1 + \frac{h}{4}\left(1 + \frac{5}{32}\varepsilon^2\right) - \frac{1}{2}\left(\frac{h}{2\pi}\right)^{1/2}\ln\left[1 + \left(\frac{h}{2}\right)^{1/2}\right] + i\frac{h}{8}\exp\left(-\frac{4}{3\varepsilon}\right) \quad (11a)$$

and

$$\left(\frac{-E}{-E}\right)^{1/2} = 2 - 0.302h^{1/2} + \frac{i}{4}(2h)^{1/2}\exp\left(-\frac{2^{1/2}}{3}\frac{h^{3/2}}{\varepsilon}\right), \quad (11b)$$

respectively.

Thus, the results obtained require the revision of the commonly accepted viewpoint on the stabilizing role of a magnetic field in the ionization of atoms [7]. In the semiclassical approximation, the stabilization regime is associated with the fact that the magnetic field "twists" the subbarrier electron trajectory and, thereby, elongates the electron path through the potential barrier. Expression (11b) is quite consistent with this statement: its imaginary part is suppressed exponentially. However, according to Eq. (11a) allowing for the spin states of a particle in a magnetic field, the imaginary part of the square root of energy and the level width increase with increasing h. This increase is close to linear in the most interesting case of a weak electric field. Note that, in a weak field $\Gamma \ll (-E_0)$, the level width virtually coincides with the ionization probability. In a strong electric field ($\varepsilon \gg 1$), the level width increases proportionally to $(e\boldsymbol{\varepsilon}/m^2)^{2/3}$, but $\Gamma > (-E_0)$ in this region, so that the simple relationship between the level width and the ionization probability is lost. The case of a strong electric field was considered in [10] and, earlier, in [12]. Although the approaches were different, the results of both works virtually coincide and indicate that the energy level is completely smeared because its width is larger than the shift by a factor of $\sqrt{3}$. The same conclusion follows from Eqs. (8a) and (8b).

It is evident that the unusual behavior of ionization probability in a strong magnetic field is due to the fact that the lowest Landau level is accessible only to the spinor particle with its spin oriented against the magnetic field. The quantizing magnetic field twists the trajectory and suppresses the contribution from all doubly degenerate energy electron states to the ionization. However, the ground nondegenerate state makes a dominant contribution to the level width in the strong magnetic field. As a result, the probability of ionization is not suppressed but increases with the intensity of the magnetic field. Such distinctions in the behavior of reaction cross sections in a strong magnetic field are well known (see, e.g., [4, 14]) for the spinor and scalar particles. This is particularly true for photoproduction of e^+e^- pairs [16] and for the photoabsorption of nonconducting crystals in a quantizing magnetic field [17].

This work was supported by the Russian Foundation for Basic Research (project no. 02-02-16784), the Foundation for Support of Leading Scientific Schools (project no. 00-15-96046), and the St. Petersburg State University Foundation for Basic Research (project no. E00-3.1-457).

REFERENCES

1. L. V. Keldysh, Zh. Éksp. Teor. Fiz. **47**, 1945 (1964) [Sov. Phys. JETP **20**, 1307 (1964)].
2. A. M. Perelomov, V. S. Popov, and M. V. Terent'ev, Zh. Éksp. Teor. Fiz. **50**, 1393 (1966) [Sov. Phys. JETP **23**, 924 (1966)]; Zh. Éksp. Teor. Fiz. **51**, 309 (1966) [Sov. Phys. JETP **24**, 207 (1967)].
3. A. I. Nikishov and V. I. Ritus, Zh. Éksp. Teor. Fiz. **50**, 255 (1966) [Sov. Phys. JETP **23**, 168 (1966)].
4. A. I. Nikishov and V. I. Ritus, Tr. Fiz. Inst. Akad. Nauk SSSR **111**, 84 (1979).
5. N. B. Delone and V. P. Kraĭnov, *Atom in a Strong Light Field* (Atomizdat, Moscow, 1978).
6. L. P. Rapoport, B. A. Zon, and N. L. Manakov, *Theory of Multiphoton Processes in Atoms* (Atomizdat, Moscow, 1978).
7. V. S. Popov, B. M. Karnakov, and V. D. Mur, Zh. Éksp. Teor. Fiz. **113**, 1579 (1998) [JETP **86**, 860 (1998)].
8. V. D. Mur, V. S. Popov, and B. M. Karnakov, Zh. Éksp. Teor. Fiz. **115**, 521 (1999) [JETP **88**, 286 (1999)].

9. V. P. Kraĭnov and M. A. Preobrazhenskiĭ, Zh. Éksp. Teor. Fiz. **103**, 1143 (1993) [JETP **76**, 559 (1993)].
10. N. P. Manakov, M. V. Frolov, B. Borca, and A. F. Starace, Pis'ma Zh. Éksp. Teor. Fiz. **72**, 426 (2000) [JETP Lett. **72**, 294 (2000)].
11. N. B. Delone and V. P. Kraĭnov, Usp. Fiz. Nauk **168**, 531 (1998) [Phys. Usp. **41**, 469 (1998)].
12. V. G. Kadyshevskiĭ and V. N. Rodionov, Teor. Mat. Fiz. **125**, 432 (2000).
13. P. J. Redmond, J. Math. Phys. **6**, 1163 (1965).
14. I. M. Ternov, V. R. Khalilov, and V. N. Rodionov, *Interaction of Charged Particles with Strong Electromagnetic Field* (Mosk. Gos. Univ., Moscow, 1982).
15. V. N. Rodionov and A. M. Mandel', Vestn. Mosk. Univ., Ser. 3: Fiz., Astron., No. 3, 25 (2001).
16. V. N. Rodionov, Zh. Éksp. Teor. Fiz. **113**, 23 (1998) [JETP **86**, 11 (1998)].
17. V. N. Rodionov, Vestn. Mosk. Univ., Ser. 3: Fiz., Astron., No. 2, 5 (1999).

Translated by R. Tyapaev

JETP Letters, Vol. 75, No. 8, 2002, pp. 368–372. Translated from Pis'ma v Zhurnal Éksperimental'noĭ i Teoreticheskoĭ Fiziki, Vol. 75, No. 8, 2002, pp. 440–444.

Spontaneous Radiation of Molecules in Open Cavities

V. V. Datsyuk

Shevchenko Kiev National University, Kiev, Vladimirskaya ul. 64, Kiev, 01033 Ukraine

e-mail: datsyuk@ups.kiev.ua

Received March 12, 2002

Within the framework of classical electrodynamics, a formula is derived for the spontaneous radiation rate of molecules and atoms in an arbitrary open cavity in the weak coupling approximation with allowance made for radiation absorption or amplification by the cavity material. The formula agrees well with microdroplet luminescence data. The effect of suppression of the spontaneous resonance radiation rate by the active laser medium is predicted. © *2002 MAIK "Nauka/Interperiodica"*.

PACS numbers: 41.60.-m; 33.20.-t

1. The rapid progress in new technologies has resulted in the observation of new data concerning the use of microscopic particles for changing the properties of optical radiation. For example, new optical effects involving plasma clusters [1], nanosized bodies [2], and microdroplets [3] were reviewed in [1–3]. In the mid-20th century, it was realized that the spontaneous radiation rate $\mathcal{R}$ of a dipole can be changed by several orders of magnitude if it is placed in a high-Q cavity [4, 5]. Today, this idea still stimulates both experimental [6– 8] and theoretical [9–15] studies. In particular, an algorithm for calculating $\mathcal{R}$ in an arbitrarily shaped cavity with an arbitrary distribution of the real dielectric constant $\varepsilon_r$was developed in [13, 14]. A number of recent studies [15] are devoted to the development of the quantum theory of atomic spontaneous radiation in the presence of dielectric bodies absorbing radiation.

In this letter, a solution to the problem of spontaneous radiation of a molecule in an arbitrary open cavity is given. The formula obtained for $\mathcal{R}$ allows for radiation absorption and amplification inside the cavity. The main purpose of this letter is to demonstrate that these factors should necessarily be taken into account, because they may revise modern concepts of the spontaneous radiation of molecules.

2. Let us consider the well-known problem of classical electrodynamics of cavity excitation by a current with volume density $\mathbf{j}(\mathbf{r}, t) = \mathrm{Re}[\mathbf{j}_\omega(\mathbf{r})\exp(-i\omega t)]$, where $\mathbf{r}$ is the radius vector and t is time. The solution to this problem is presented below mainly to determine the quantities entering the formula for $\mathcal{R}$.

Assume that the properties of electromagnetic modes in an open cavity with real dielectric constant ε_r are known. Each cavity mode is characterized by a set of indices s, the electric field vector $\mathbf{E}_s$, the circular frequency ω_s, and the quality factor $Q_s = \omega_s/\gamma_s$. The quantity Q_s allows for the radiation loss $dU_s/dt = -(\omega_s/Q_s)U_s$, where $U_s = U_s^e + U_s^m$ is the sum of electric- and magnetic-field energies.

The oscillating dipole with dipole moment $\mathbf{p}$ and $\mathbf{j}_\omega(\mathbf{r}) = -i\omega\mathbf{p}\delta(\mathbf{r} - \mathbf{r}_p)$ excites the cavity modes with amplitudes a_s. The electric-field energy in the cavity is $U = \frac{1}{2}\sum_s |a_s|^2 U_s$. The radiation power is given by the expression

$$\frac{dU}{dt} = \frac{1}{2}\sum_s |a_s|^2 \frac{dU_s}{dt}. \quad (1)$$

The conditions under which one can pass from the wave equation to the equations for slowly varying amplitudes are well known. These are, first, the mode orthogonality conditions, which are satisfied for the open cavity with a relative accuracy of about $1/Q_s$ [16]. Second, the inequalities

$$1/(\Delta\omega) \ll t \ll 1/\mathcal{R} \quad (2)$$

must be fulfilled, where $\Delta\omega$ (s^{-1}) is the radiation linewidth [17]. When written in the form $\mathcal{R}/\Delta\omega \ll 1$, condition (2) is referred to as the condition for weak oscillator–cavity coupling [18, 19].

In classical electrodynamics, the light absorption or amplification by the cavity material can be taken into account through adding an imaginary part $i\varepsilon_i$ to the dielectric constant. For simplicity, it will be assumed that the function ε_i is smoother than $\mathbf{E}_s(\mathbf{r})$. In this case, the effects of intermode energy exchange can be ignored [20] and the quantities a_s are

$$a_s = -\frac{1}{2U_s^e}\mathbf{p}\mathbf{E}_s^*(\mathbf{r}_p)\frac{\omega}{\omega - \omega_s + i(\gamma_s + \gamma_a)/2}, \quad (3)$$

where $\omega \simeq \omega_s$, $\gamma_a \equiv \omega/Q_a$, and $Q_a \equiv \varepsilon_r/\varepsilon_i$.

Substituting Eq. (3) into Eq. (1), one can find the ratio of the dipole radiation rate $\mathcal{R} = -(2\pi/h\omega)(dU/dt)$ in the cavity to the rate $R_V = p^2\omega^3/6\varepsilon_0 hc^3$ of the same radiation in an infinite vacuum:

$$\frac{\mathcal{R}}{R_V} = \frac{2\pi c^3}{\varepsilon_r V\omega^3}\sum_s f_s(\mathbf{e}, \mathbf{r}_p)F_s(\omega), \quad (4)$$

where ε_0 is the dielectric constant, h is the Planck's constant, c is the speed of light, V is the cavity volume, $f_s(\mathbf{e}, \mathbf{r}_p)$ is the factor allowing for the orientation $\mathbf{e} \equiv \mathbf{p}/p$ of the dipole and its position in the cavity,

$$f_s(\mathbf{e}, \mathbf{r}_p) \equiv \frac{3\varepsilon_r|\mathbf{e}\mathbf{E}_s(\mathbf{r}_p)|^2 V}{\int \varepsilon_r|\mathbf{E}_s(\mathbf{r})|^2 dV}, \quad (5)$$

and $F_s(\omega)$ is the dimensionless radiation line shape in the vicinity of the sth resonance,

$$F_s(\omega) \equiv \frac{1}{Q_s}\left[4\left(\frac{\omega-\omega_s}{\omega}\right)^2 + \left(\frac{1}{Q_s}+\frac{1}{Q_a}\right)^2\right]^{-1}. \quad (6)$$

When deriving Eq. (4), it was taken into account that $U_s/U_s^e = 2$ to within the terms on the order of $1/Q_s$.

One can see from Eq. (5) that the excitation efficiency of the sth cavity mode and, hence, $\mathcal{R}$ strongly depend on the dipole position and orientation in the cavity. The f_s value averaged over the directions $\mathbf{e}$ and the coordinates $\mathbf{r}_p$ is $\langle f_s(\mathbf{e}, \mathbf{r}_p)\rangle = 1$. Below, the averaged radiation rate is denoted by R.

By substituting $\langle f_s(\mathbf{e}, \mathbf{r}_p)\rangle$ into Eq. (4) and assuming that $\omega = \omega_s$ and $\varepsilon_i = 0$, one arrives at the formula for the mean spontaneous radiation rate at the resonant frequency

$$\frac{R(\omega_s)}{R_V} = \frac{Q_s\lambda^3}{4\pi^2 V\varepsilon_r}, \quad (7)$$

where $\lambda \equiv 2\pi c/\omega$. For $\varepsilon_r = 1$, the right-hand side of Eq. (7) differs by a factor of 1/3 from the result of frequently cited work [4], where the orientational averaging was not carried out. The obtained result is also different from the result of Bunkin and Oraevskiĭ [5] by a factor of 2, because of a difference in the definitions of the cavity-mode Q factors. An experiment devoted to the verification of the formula of type (4) is described in [7].

In spite of the long-standing interest in the spontaneous radiation in cavities [2–5] and recent theoretical developments [8–15], Eq. (4), in which $\mathcal{R}$ depends on the light absorption or amplification, is, probably, obtained for the first time.

Before turning to the comparison of the obtained formulas with the experimental data, the following should be pointed out. When deriving Eq. (4), it was assumed implicitly that the dipole interaction with the external electromagnetic field could be ignored. That is why the dipole radiation was termed spontaneous. It turns out that the rate (4) is independent of the sign of $\gamma \equiv \gamma_s + \gamma_a$. However, the properties of the initial differential equations for slowly varying amplitudes $a_s(t)$ depend essentially on this sign. At $\gamma < 0$, the steady-state solution (3) is unstable. A small addition to a_s increases by a factor of e at time $t = 1/|\gamma|$. Consequently, an active cavity may pass on to the lasing regime. However, this does not mean that solution (3) loses physical meaning, because the spontaneous radiation is, by definition, independent of the stimulated radiation.

3. Equations (4)–(6) involve cavity characteristics ω_s and Q_s, whose calculation may become a complicated mathematical problem. For a cavity of simple shape, the solution for $\mathcal{R}$ can be brought to numerical estimates. The problem of electric radiation of a dipole inserted into an ideal dielectric sphere is most simple. Its solution was given using both classical [19] and quantum [18] electrodynamics [2, 3].

The classical and quantum theories both give the same formula for R/R_V. However, contrary to the quantum approach, classical electrodynamics allows one to consider the radiation from a sphere with a complex dielectric constant. For example, the properties of heat radiation from a microsphere with positive imaginary part ε_i were studied in [21]. It was found in [22] that the use of asymptotic expansions for the Bessel and Hankel functions leads to the form (6) for the line shape of electric dipole radiation. Equation (6) was suggested in [22], where it involved the resonance mode frequencies and the radiation Q factors introduced by Vaĭnshteĭn in [16].

4. The inclusion of light absorption is important for the understanding of radiation physics in a high-Q cavity. Let us first consider the ideal case without light absorption in the cavity; i.e., $\varepsilon_i = 0$. One has for this case $F_s(\omega_s) = Q_s$ and $\int F_s(\omega)d\omega = (\pi/2)\omega_s$. Therefore, the spontaneous transition rate at the resonant frequency increases with Q_s; i.e., $R(\omega_s) \longrightarrow \infty$ as $Q_s \longrightarrow \infty$. At the same time, the frequency-integrated quantity $\int R(\omega)d\omega$ is independent of Q_s.

In practice, light absorption is always present. For this reason, let us determine the probability of spontaneous radiation for $|\varepsilon_i| \neq 0$ and $Q_s \gg |Q_a|$. If the latter inequality is fulfilled, one has

$$F_s(\omega_s) \simeq \frac{Q_a^2}{Q_s} \ll 1, \quad \int F_s(\omega)d\omega \simeq \frac{\pi\omega_s}{2}\frac{|Q_a|}{Q_s} \ll 1. \quad (8)$$

Therefore, the spontaneous transition rate at the resonant frequency decreases with increasing Q_s; i.e., $R(\omega_s) \longrightarrow 0$ and $\int R(\omega)d\omega \longrightarrow 0$ as $Q_s \longrightarrow \infty$.

The fact that radiation into high-Q modes is forbidden in a real ($|\varepsilon_i| \neq 0$) cavity restricts the possibility of

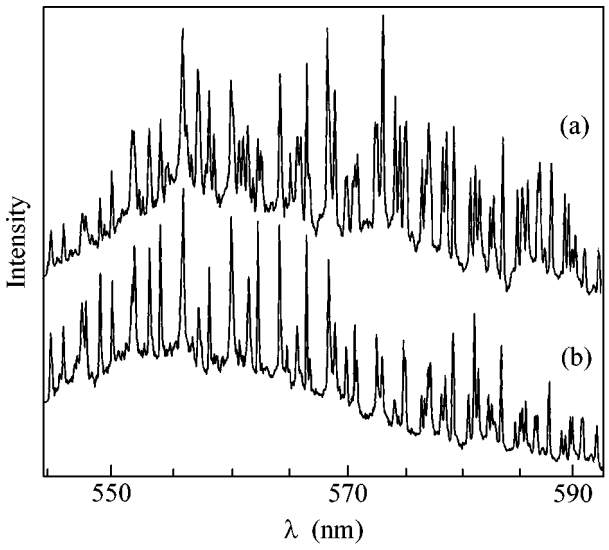

Fluorescence spectra of rhodamine 6G (b) in the droplets of pure liquid and (a) with dissolved nanoparticles [26].

experimentally implementing the states with strongly coupled oscillator and cavity [9–12].

5. In the experiments with luminescent microdroplets [3], the radiation Q factors of the whispering gallery modes (WGM) may be very high. For example, according to the calculations carried out in [23], $Q_s > 10^{27}$ for the first-order modes in water droplets with $x = 2\pi a/\lambda > 180$. At the same time, in ordinary liquids, light is absorbed with $Q_a = 10^8$–10^{12} [24, 23]. Such a ratio between Q_s and Q_a and Eqs. (8) explains the fact that the low-order modes (with $Q_s \gg |Q_a|$) are sometimes not observed in the luminescence spectra of microdroplets [24, 25, 8].

To reduce the Q factors for low-order modes, polymer nanoparticles were added to a liquid in [26, 27]. In [26], the influence of a poly(styrene) sphere of diameter 87 nm on the luminescence spectrum of monodispersion droplets with a diameter of 20 μm was studied. The droplets consisted of a solution of rhodamine 6G in a mixture of equal volumes of ethanol and water. Let us compare the fluorescence spectra that are obtained in [26] and shown in the figure. At $\lambda \geq 585$ nm, the light absorption is negligibly weak. For this reason, the resonant modes in spectra (a) and (b) are of the first to fifth orders. As λ decreases, the light absorption by the rhodamine molecules increases. The first- and second-order resonance peaks at, respectively, $\lambda \leq 575$ nm and $\lambda \leq 566$ nm disappear sequentially from the fluorescence spectrum (b). These peaks appear upon the addition of scattering particles to the liquid. The greatest distinction between spectra (a) and (b) is observed in the vicinity of $\lambda \simeq 560$ nm. In the range $\lambda \simeq 555$–562 nm, the number of resonances in the spectrum (a) is more than twice the number of resonances in the droplets of pure liquid. At $\lambda \simeq 550$ nm, the absorption coefficient rapidly increases with a decrease in λ and appreciably exceeds the scattering coefficient. For this reason, only the fourth- and fifth-order modes appear in the spectra (a) and (b).

In the experiment conducted in [8], the first-order peaks disappeared and appeared again due to the surface oscillations of a droplet suspended in an electromagnetic trap.

The observed spectral features were explained heuristically by introducing the cavity-mode efficiency φ [25, 26]. It was pointed out in [26] that the peak amplitude is proportional to $\phi = (1/Q_0 + 1/Q_b)/(1/Q_0 + 1/Q_b + 1/Q_a)$, where $Q_b \equiv (1/\beta)\sqrt{\varepsilon_r\mu}\,(\omega/c)$; β is the light scattering coefficient; and Q_0 is the WGM quality factor in an ideal droplet, as calculated without inclusion of light scattering and absorption. The mode Q factor in a real droplet was taken to be $1/Q \simeq 1/Q_0 + 1/Q_b + 1/Q_a$. This relationship coincides with the theoretical estimate obtained in [28]. Thus, according to [26], the product of peak amplitude by peak width should not depend on Q_a. This conclusion is in contradiction with the figure and Eqs. (6) and (8), where $1/Q_s = 1/Q_0 + 1/Q_b$. The heuristic explanation given in [26] would be correct if φ was introduced as an integrated quantity $(2/\pi\omega)\int F(\omega)d\omega$ in the vicinity of the sth resonance.

Thus, the suggested theory explains the fact that the spectral composition of the microdroplet luminescence spectra is enriched upon the artificial lowering of the WGM Q factor.

6. Let us turn back to the analysis of Eqs. (18). The light propagation in a medium with negative ε_i can be characterized by the gain $g = -\varepsilon_i\sqrt{\mu/\varepsilon_r}\,(\omega/c)$, where μ is the permeability of cavity material. According to Eq. (6), the spontaneous radiation rate at a resonance frequency increases to infinity with increasing g, while Δω decreases to zero as $\omega \longrightarrow \omega_s$ and $Q_s + Q_a \longrightarrow 0$. If $R(\omega_s)$ increases in the $Q_s \simeq -\varepsilon_r/\varepsilon_i$ regime, condition (2) breaks down and Eq. (3) becomes inappropriate. This constraint on the possibility of using Eq. (4) is removed if $|\varepsilon_i| \gg \varepsilon_r/Q_s$. In the regime of strong light amplification in an active medium, the spontaneous radiation into resonant modes is suppressed: $R(\omega_s) \longrightarrow 0$ and $\int R(\omega)d\omega \longrightarrow 0$ as $g \longrightarrow \infty$. The effect of resonance radiation suppression in an active microdroplet was explored in recent work [22] numerically, analytically, and by analyzing the experimental data.

Therefore, an increase of $|\varepsilon_i|$ (decrease of $|Q_a|$) in the cavity should suppress the resonance radiation, irrespective of the sign of ε_i.

7. In the commonly accepted paradigm of laser physics, the Einstein coefficient A for the spontaneous phototransitions is a constant. Let us consider the main properties of A for the molecular transition in a linear laser. A linear laser is a laser whose length L far exceeds

the characteristic cross section d. The Q factor of the longitudinal modes in such a laser can be estimated by the formula [29]

$$Q = \frac{\omega L\sqrt{\varepsilon_r\mu}}{c(1-M)}, \quad (9)$$

where M is the mirror gross reflectivity.

The Einstein coefficient A for the spontaneous transitions between two groups of levels with energies E_u and E_l can be introduced the same way as in [5]:

$$A = \int dE_l \rho_l(E_l) \int dE_u \rho_u(E_u) h(E_u) R\left(\frac{E_i - E_l}{\hbar}\right), \quad (10)$$

where $\rho_n(E_n)dE_n$ is the number of states in the energy interval from E_n to $E_n + dE_n$ ($n = u, l$); $\int \rho_n(E_n)dE_n = G_n$; G_u and G_l are the degrees of degeneracy of the upper (u) and lower (l) states; and $h(E)$ is the probability that the excited molecule will have energy E, so that $\int \rho_u(E)h(E)dE = 1$. Of fundamental importance is that the result of calculating A will be independent of the cavity-mode Q factor only if $|Q_a| \gg Q_s$.

Let us calculate the rate (4), which enters the right-hand side of Eq. (10), by integrating only over the longitudinal modes of the linear laser. The resulting A_L is smaller than A. In the calculation of laser intensity in [29–31], the corresponding decrease in the Einstein coefficient was allowed for by multiplying A by $\Delta\Omega/4\pi$, where $\Delta\Omega = (\pi/4)(d/L)^2$.

The molecular transition linewidth is ordinarily larger than ω/Q_s and $\omega/|Q_a|$. Assuming that these conditions and the inequality $gL \gg 1 - M$ are fulfilled and ignoring the fact that R changes at the line wings, one obtains from Eqs. (8) and (9) the following relations:

$$A_L(g) \simeq \frac{1-M}{gL} A_L(0). \quad (11)$$

The theoretically obtained decrease in the Einstein coefficient A_L should be taken into account when calculating the characteristics of laser superradiance [30, 32].

One may take a molecular F_2 laser (wavelength 157 nm) as an object for experimentally testing the validity of Eq. (11). This laser is of considerable interest, because it holds promise for use in fabricating computer chips with a 0.1-μm architecture [33]. According to [34], the value of gL in an electric-discharge F_2 laser is as large as 29. The signal power amplified in such a laser with $g = 0.37$ cm^{-1} and $L = 40$ cm in the saturation regime [35] was found to be five times lower than the predicted value.

8. The influence of a cavity on the spontaneous radiation rate $\mathcal{R}$ of molecules is ordinarily believed to be a well-known physical phenomenon. However, in the calculation of $\mathcal{R}$ or the Einstein coefficient A, the light absorption and amplification effects are, as a rule, ignored. In this letter, a very simple theoretical model has been used to demonstrate that these factors are of fundamental importance. The model suggested accords well with the results of previous theoretical and experimental studies. Equations (4)–(6) can be used to determine $\mathcal{R}$ in cavities filled with a light-absorbing, amplifying, or scattering medium. It is shown that a number of effects, called laser effects, can be explained by the specific properties of spontaneous radiation in a cavity. For example, a nonlinear increase in peak amplitudes may be caused by an increase of light scattering in a medium. At the same time, it is predicted that spontaneous resonance radiation can be suppressed and broadened in an amplifying medium.

This work was supported in part by the INTAS (grant nos. 99- 00701 and 2000-556).

REFERENCES

1. B. M. Smirnov, Usp. Fiz. Nauk **170**, 495 (2000).
2. V. V. Klimov, M. Ducloy, and V. S. Letokhov, Kvantovaya Élektron. (Moscow) **31**, 569 (2001).
3. V. V. Datsyuk and I. A. Izmaĭlov, Usp. Fiz. Nauk **171**, 1117 (2001).
4. E. M. Parcell, Phys. Rev. **69**, 681 (1946).
5. F. V. Bunkin and A. N. Oraevskiĭ, Izv. Vyssh. Uchebn. Zaved., Radiofiz. **2** (2), 181 (1959).
6. A. J. Campillo, J. D. Eversole, and H. B. Lin, Mod. Phys. Lett. **6**, 447 (1992).
7. J. M. Gérard, B. Sermage, B. Gayral, *et al.*, Phys. Rev. Lett. **81**, 1110 (1998).
8. H. Yukawa, S. Arnold, and K. Miyano, Phys. Rev. A **60**, 2491 (1999).
9. H. M. Lai, P. T. Leung, and K. Young, Phys. Rev. A **37**, 1597 (1988).
10. V. V. Klimov and V. S. Letokhov, Pis'ma Zh. Éksp. Teor. Fiz. **68**, 115 (1998) [JETP Lett. **68**, 124 (1998)].
11. V. V. Klimov and V. S. Letokhov, Pis'ma Zh. Éksp. Teor. Fiz. **70**, 192 (1999) [JETP Lett. **70**, 189 (1999)].
12. V. V. Klimov, M. Ducloy, and V. S. Letokhov, Phys. Rev. A **59**, 2996 (1999).
13. Y. Xu, R. K. Lee, and A. Yariv, Phys. Rev. A **61**, 033807 (2000).
14. Y. Xu, R. K. Lee, and A. Yariv, Phys. Rev. A **61**, 033808 (2000).
15. H. T. Dung, L. Knöll, and D.-G. Welsch, Phys. Rev. A **62**, 053804 (2000).
16. L. A. Vainshtein, *Open Resonators and Open Waveguides* (Sov. Radio, Moscow, 1964; Golem Press, Boulder, 1969).
17. A. S. Davydov, *Quantum Mechanics* (Fizmatgiz, Moscow, 1963; Pergamon, Oxford, 1976).
18. S. C. Ching, H. M. Lai, and K.Young, J. Opt. Soc. Am. B **4**, 2004 (1987).
19. H. Chew, Phys. Rev. A **38**, 3410 (1988).
20. A. N. Oraevskiĭ, M. O. Scully, and V. L. Velichanskiĭ, Kvantovaya Élektron. (Moscow) **25**, 211 (1998).
21. S. Lange and G. Schweiger, J. Opt. Soc. Am. B **11**, 2444 (1994).

22. V. V. Datsyuk, J. Opt. Soc. Am. B **19**, 142 (2002).
23. A. Serpengüzel, J. C. Swindal, R. K. Chang, and W. P. Acker, Appl. Opt. **31**, 3543 (1992).
24. S. C. Hill and R. E. Benner, J. Opt. Soc. Am. B **3**, 1509 (1986).
25. P. Chýlek, H.-B. Lin, J. D. Eversole, and A. J. Campillo, Opt. Lett. **16**, 1723 (1991).
26. H.-B. Lin, A. L. Huston, J. D. Eversole, *et al.*, Opt. Lett. **17**, 970 (1992).
27. T. Kaiser, G. Roll, and G. Schweiger, J. Opt. Soc. Am. B **12**, 281 (1995).
28. V. V. Datsyuk, Appl. Phys. B **54**, 184 (1992).
29. S. A. Losev, *Gas-Dynamic Lasers* (Nauka, Moscow, 1977).
30. A. V. Eletskiĭ and B. M. Smirnov, *Gas Lasers* (Atomizdat, Moscow, 1971).
31. F. Kannari, M. Obara, and T. Fujioka, J. Appl. Phys. **57**, 4309 (1985).
32. E. C. Harvey, C. J. Hooker, M. H. Key, *et al.*, J. Appl. Phys. **70**, 5238 (1991).
33. C. J. Sansonetti, J. Reader, and K. Vogler, Appl. Opt. **40**, 1974 (2001).
34. M. Kakehata, C.-H. Yang, Y. Ueno, and F. Kannari, J. Appl. Phys. **74**, 2241 (1993).
35. M. Kakehata, Y. Ueno, K. Tamura, and F. Kannari, J. Appl. Phys. **75**, 1304 (1994).

Translated by V. Sakun

JETP Letters, Vol. 75, No. 8, 2002, pp. 373–377. Translated from Pis'ma v Zhurnal Éksperimental'noĭ i Teoreticheskoĭ Fiziki, Vol. 75, No. 8, 2002, pp. 445–449.

What Initiates the Explosion of a Current-Carrying Conductor?

V. S. Vorob'ev[1]*, S. P. Malyshenko[2], S. I. Tkachenko[1], and V. E. Fortov[1]

[1] *Institute of Thermal Physics of Extremal States, Russian Academy of Sciences, Moscow, 127412 Russia*

** e-mail: vrbv@mail.ru*

[2] *Institute of High Temperatures, Russian Academy of Sciences, Moscow, 127412 Russia*

Received March 13, 2002

It is shown that the explosion of a conductor heated by a high-power current pulse is initiated by the nuclei of liquid phase that appear in the layer of a supersaturated vapor surrounding the liquid current-carrying core. The instant of electric explosion and the expansion velocity predicted by this scenario are confirmed by the experimental and computational data on current-induced heating of a tungsten conductor. © *2002 MAIK "Nauka/Interperiodica".*

PACS numbers: 64.70.Fx; 64.60.My

A conductor heated by a high-power current pulse evolves through several stages: slow heating with thermal expansion and melting is followed by heating in a liquid phase (thermal expansion of a liquid is accompanied by evaporation from its surface). At a certain energy input, less than that required for the complete evaporation of the conductor, there comes a point after which the abrupt increase in the conductor radius cannot be explained by these effects alone. The hypotheses involving the propagation of the evaporation wave from the wire surface and the loss of thermodynamic stability of a superheated liquid have not been confirmed experimentally and are incapable of elucidating the cause for such a rapid transition from the slow expansion regime to the regime of abrupt increase in expansion velocity (see [1, 2] and references cited therein).

Analysis of the experimental data has shown [2] that a fine-dispersed mass remaining after the metal explosion is a sol with its particle size dependent on the instant of current breaking and that the energy input into the conductor is always lower than the energy required for the complete evaporation of the wire. If the current does not break until explosion, the characteristic particle size is comparable with the electron mean free path equal to $\sim 2 \times 10^{-6}$ cm. The physical nature of the processes initiating the transformation of a liquid conducting wire surrounded by vapor to a weakly conducting sol rapidly expanding in the radial direction remains to be clarified.

It is shown in [3, 4] that, in the fast heating regimes, the two-phase system consisting of a liquid conductor with current flowing in it and a vapor in equilibrium with the conductor may become thermodynamically unstable. In such regimes, the liquid phase with current does not reach its boiling state (because of the magnetic-field-induced compression), while the equilibrium pressure of a vapor coexisting with the liquid exceeds the saturation vapor pressure p_s. The system consisting of a liquid with current flowing in it and vapor surrounding it may become thermodynamically absolutely unstable if the vapor pressure reaches the limiting value corresponding to the spinodal gas branch. As a result, this two-phase system will undergo a thresholdless jumpwise transition to a new state, namely, to liquid droplets dispersed in the vapor.

Below, we consider the mechanism of the threshold initiation of electric explosion. At the stage of heating of a liquid current-carrying conductor, the vapor is in equilibrium with the conductor but is metastable relative to the liquid phase without current. For this reason, liquid droplets may spontaneously appear and grow upon achieving certain supersaturation. As a result, the system "liquid conductor–vapor" with current may become thermodynamically unstable and decay before the vapor achieves the spinodal parameters. The possibility of this decay occurring is determined by the ratio between the heating characteristic time for the conductor and the expectation time for the appearance of droplets with critical size in the vapor.

In this work, the semiempirical broad-range equation of state [5, 6] describing high-temperature phase transitions to the metastable states is used to study the phase states through which a tungsten conductor passes during the current-induced heating and to determine the limiting degree of vapor supersaturation above which the vapor spontaneously condenses in the boundary layer. It is shown that the probability of large critical-sized droplets appearing increases with temperature. The growth of these droplets initiates an abrupt increase in the evaporation rate, as a result of which the cylindrical shape of the liquid conductor becomes unstable, the conductor breaks down into small-sized

0021-3640/02/7508-0373$22.00

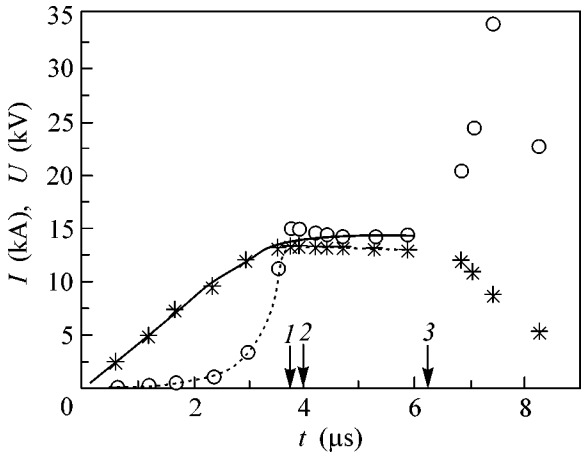

Fig. 1. Time dependences of the (solid line) current and (dashed line) voltage drop in a current-heated conductor [7]. The points are for the experimental data [8].

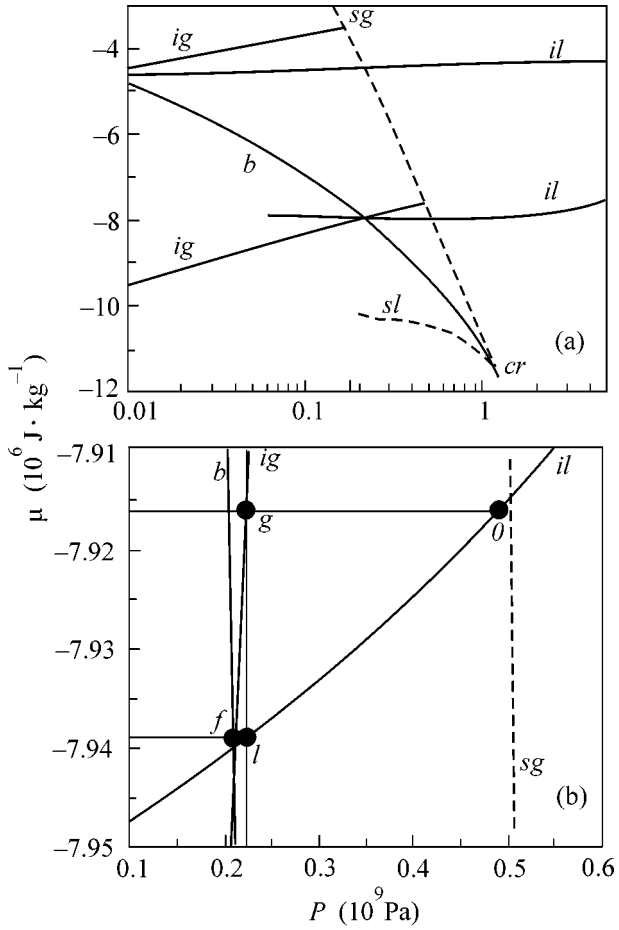

Fig. 2. (a) Tungsten phase diagram in the μ–P plane, as constructed according to the equation of state given in [6]. (b) The same on an enlarged scale.

droplets, and the system transforms into a weakly conducting sol [2]. The time instant of this transition is determined for a heating regime described in [7, 8] for a tungsten conductor.

In the presence of current, the equilibrium condition for a cylindrical conductor (of radius R) and its vapor, whose conductivity is lower than the conductor conductivity, is written as

$$\mu_g = \mu_l + \int_0^R \frac{\mathbf{f}_A}{\rho_l} d\mathbf{r}, \qquad (1)$$

where μ_g and μ_l are the chemical potentials of gas and liquid, respectively; ρ_l is the liquid density; and the integral in Eq. (1) is the potential of Ampere force f_A per unit mass. The Ampere force is directed to the center of the conductor and has the form $f_A = \mu_0 j^2 r/2$ for the homogeneous current density, where μ_0 is the permeability of free space, and r is the distance from the conductor axis. Condition (1) is supplemented by the requirement that the pressures on both sides of the interface be equal. For small deviations from equilibrium, the chemical potentials can be linearized with respect to pressure: $\mu \approx \mu_s + (p - p_s)/\rho$ (index s labels the quantities corresponding to the equilibrium at a given temperature in the absence of current). Combining this with the condition that the liquid density depends weakly on the conductor radius, one obtains

$$(p - p_s)(1 - \rho_g/\rho_l) = \Delta p \frac{\rho_g}{\rho_l}; \quad \Delta p = \frac{\mu_0 j^2 R^2}{4}, \qquad (2)$$

where p is the pressure of gas and liquid, and ρ_g is the gas density at the interface. One can see from Eq. (2) that the pressure at the interface is always higher than the pressure p_s corresponding to the equilibrium in the absence of current.

Figure 1 shows the calculated [7] and measured [8] time dependences of current and voltage in the course of heating a tungsten conductor. The conductor and circuit parameters are as follows: the radius of the conductor is $a_0 = 0.175$ mm; its length is $l = 8.7$ cm; the inductance is $L = 4.5$ μH; the capacitance is $C = 6$ μF; and the initial voltage is $U_0 = 20$ kV. The arrows in Fig. 1 indicate (*1*) the onset of melting, (*2*) the completion of melting, and (*3*) the beginning of an abrupt growth of the conductor radius.

Figure 2 shows the "pressure–chemical potential" phase diagram at a fixed temperature, as constructed using the semiempirical equation of state for tungsten [6]. The following notation is introduced for the lines: *b* is the binodal; *sl* and *sg* are the liquid and gas spinodals, respectively; and *ig* and *il* are the isotherms of chemical potential of gas and liquid, respectively. The points of intersection of the lines *ig* and *il* correspond to the equilibrium state of the liquid–gas system with pressure p_s and chemical potential μ_s in the absence of

current. The horizontal line in Fig. 2b is the total chemical potential, which is constant throughout the system. The point O denotes the state of the conductor on its axis (a contribution of the Ampere potential to the liquid chemical potential at this point is zero, so that the total chemical potential coincides with the liquid potential), and the points l and g denote, respectively, the liquid and gas states at the interface at pressure p. One can see that the liquid chemical potential $\mu_l(p)$ is lower than the gas potential $\mu_g(p)$, which is equal to the total chemical potential of the system. A balance is achieved after adding the Ampere potential to the liquid chemical potential. Therefore, the total chemical potentials in both media are the same.

To determine the conditions for the formation of critical-sized droplets in a supersaturated vapor surrounding a conductor with current, we use the theory of homogeneous nucleation [9], according to which the probability of formation of a liquid droplet is proportional to $\exp(-A/T)$, where A is the minimal work necessary for droplet formation and T is temperature. For a spherical droplet of radius a, the minimal work is given by the expression

$$A = 4\pi a^2\sigma - \frac{4\pi a^3}{3}\left[(p_g - p_s)\left(1 - \frac{\rho_l}{\rho_g}\right)\right], \qquad (3)$$

where σ is the surface tension and p_g is the gas pressure. Both the liquid conductor with current and a droplet of condensed vapor may be in equilibrium with the supersaturated vapor. The pressures and chemical potentials of the condensed droplet and the liquid must coincide on the conductor axis. The critical radius and the work of formation of a critical-sized droplet can be found from the expressions

$$a_c = 2\sigma/\Delta p; \quad A_c = 16\pi\sigma^3/3(\Delta p)^2, \qquad (4)$$

where Δp is given by Eq. (2). The surface tension $\sigma(T)$ was determined using the data reported in [10].

At temperatures $T \sim 10$–14 kK, the equilibrium vapor density is $n = (5 \times 10^{20}$–$3 \times 10^{21})$ cm^{-3}; the equilibrium concentration of tungsten ions, as calculated from the Saha formula, is $n_i = (10^{19}$–$1.8 \times 10^{20})$ cm^{-3}; the Debye radius is $r_d \sim (17$–$6) \times 10^{-8}$ cm; and the mean interaction energy (normalized to temperature) between charged particles at a distance equal to the Debye length is as large as ≤ 1.4, indicating substantial nonideality. The role of charged particles in the nucleation process [11] should also be taken into account at distances smaller than the Debye radius, because the field of an individual charge is "felt" only inside the sphere of this radius.

Using [12], we write the following expressions for the critical radius and the work of formation of a critical-sized droplet on an ion under the condition that the droplet radius is markedly smaller than the Debye radius:

$$A_c = 4\pi a_c^2\sigma - \frac{4\pi a_c^3}{3}\left[(p_g - p_s)(\rho_l/\rho_g - 1) - \frac{3e^2}{8\pi a_c^4}\right], \qquad (5)$$

$$(p_g - p_s)(1 - \rho_l/\rho_g) = 2\sigma/a_c - e^2/8\pi a_c^4 = \Delta p. \qquad (6)$$

The set of Eqs. (5) and (6) has two solutions. The first corresponds to small critical sizes, i.e., to the case where both terms on the right-hand side of Eq. (6) are large compared to their difference. This gives the well-known Rayleigh result $a_c = (e^2/16\pi\sigma)^{1/3}$. In this case, the surface electric force is counterbalanced by the surface tension force. One can easily show that the corresponding work A is minimum, so that the droplets of this size are stable and represent, in actuality, the cluster ions typical of metal vapor plasmas [13]. For the regime of current-induced heating of a tungsten conductor considered in this work, the size of these droplets changes weakly [$a_c = (1.5$–$3) \times 10^{-8}$ cm] with changing temperature in the range $T \sim 7$–14 kK and never exceeds the Debye radius. These "droplets" contain from one to five atoms.

The solution, for which the second term on the right-hand side of Eq. (6) can be ignored, corresponds to larger radii a_c and to the maximum of function A. In the same temperature range, the size of large droplets corresponding to this maximum changes within $a_c = (9$–$1) \times 10^{-7}$ cm. Inasmuch as these values are larger than the corresponding Debye radii, the influence of ion charge on the nucleation processes becomes insignificant for the droplets of sizes as large as those.

At a certain critical degree of vapor supersaturation, the critical radii corresponding to minimal and maximal work start to coincide; i.e., the extremums of A as a function of nuclear size disappear. As a result, liquid droplets of every size start to grow [12]. In the heating regime considered in this work for the tungsten conductor, the degree of supersaturation is markedly lower than this critical value.

The mean expectation time τ for the appearance of a nucleus in the volume V of a metastable vapor is usually written as [9]

$$\tau = (10^{10} n \exp(-G) V)^{-1}, \qquad (7)$$

where $G = A_c/T$ is the Gibbs number and n is the number of nucleation centers in unit volume. We are interested in the time it takes for the droplets of critical size a_c to appear in a layer of thickness R_r near the liquid conductor–vapor interface; $V = 2\pi R l R_r$ is the volume of this layer, and l is the conductor length.

Small-sized nuclei are universally present on ions, because the expectation time for them is $\tau_k \sim 0.6$ μs even at $T \sim 6$ kK and rapidly decreases with a rise in temperature. The nuclei of larger size become stable at

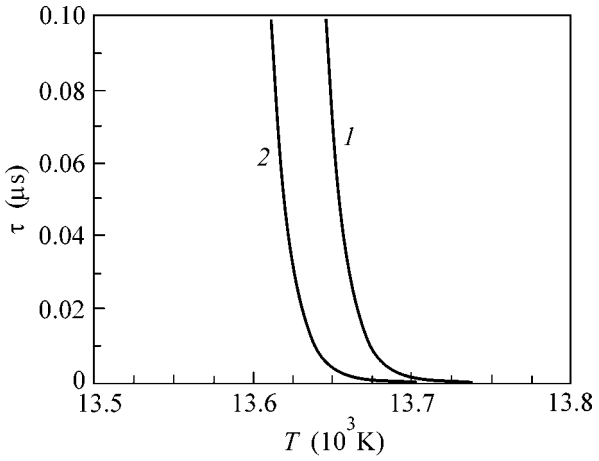

Fig. 3. Expectation time for the appearance of liquid droplet vs. vapor temperature: $R_r = (1)\ 2a_c$ and $(2)\ 20a_c$.

a certain temperature. As soon as the mean expectation time for them becomes comparable with the characteristic time of the process, the critical-sized droplets appear in the near-surface vapor layer and start to grow. In Fig. 3, the mean expectation time for the appearance of a liquid-phase nucleus is shown as a function of temperature. For the regime considered, the temperature, after which large-sized droplets start to grow catastrophically fast, equals $T_l \sim 13.6$ kK. Note that this temperature depends weakly on the thickness of the boundary layer [we used $R_r \sim (2–20)a_c$ in our calculations]. According to [6], the instant of time at which this temperature is achieved is $t = 6.03$ μs, which coincides with the onset of intense wire expansion (arrow in Fig. 1).

Assume that a ring waist with radius $r_n \ll R$ appears in the cylindrical conductor. Below, we show that such a waist makes the formation of liquid-phase nuclei easier. The equilibrium pressure vapor near the waist changes for two reasons: it decreases by a value of $2\sigma\rho_g/r_n\rho_l$ due to surface curving and increases due to a decrease in the conductor radius in the waist ($R \longrightarrow R - 2r_n$) and, hence, a local increase in the current density in this cross section. Combining both these effects, one can write the change in the vapor pressure in the presence of the waist as $\Delta p' = \Delta p(1 - a_c R/6r_n^2)$. It follows that the cylindrical conductor surface becomes unstable upon the formation of critical-sized droplets, provided that the waist radius satisfies the condition $r_n > (Ra_c/6)^{0.5}$. For $T = T_l$, one has $r_n > 10^{-4}$ cm.

Hence, a system "current-carrying conductor–vapor collapsing into liquid droplets" becomes unstable and should transform into a new state with a lower total chemical potential. Before the decay, the states of the liquid conductor at the interface (the point *l* in Fig. 2b) had minimal chemical potential. After the decay, the chemical potential of the currentless system of liquid droplets and vapor must be equal to this minimal value. The chemical potential marked by the point *f* in Fig. 2b corresponds to the vapor in equilibrium with these droplets. The droplet size a_f after the decay can be estimated from the Laplace formula $a_f = 2\sigma/\Delta p_f$, where Δp_f is the difference in the droplet and vapor pressures after the decay, to obtain $a_f \sim 3.5 \times 10^{-6}$ cm for the regime considered. This value is close to the experimental data given in [14], where the diameter of particles in a fine-dispersed tungsten powder obtained after the electric explosion of the conductor was $\sim 3 \times 10^{-6}$ cm. The number of droplets appearing per unit length of a conductor after its destruction can be found from the relationship $N = 3R^2/4a_f^3$. The excessive energy is expended on the formation of the droplet surfaces and droplet kinetic energy. The corresponding balance is written as

$$\pi R^2 \Delta\mu\rho_l = N\left(4\pi a_f^2\sigma + \frac{4\pi\rho_l a_f^3 u^2}{6}\right), \qquad (8)$$

where $\Delta\mu$ is the difference in the total chemical potentials of the system before and after its decay. Then, the droplet expansion velocity after the decay can be found from the relationship

$$u = \sqrt{2\Delta\mu - 3\Delta p_f/\rho_l}. \qquad (9)$$

According to the graph in Fig. 2, $\Delta\mu \approx 2.5 \times 10^4$ J/kg and $\Delta p_f \approx 0.02$ GPa. Thus one finds that the initial expansion velocity is $u \approx 200$ m/s. The vapor pressure in the mixture is ~0.21 GPa; in the calculations [7], the pressure of the ambient medium was 0.1 GPa. For this reason, the liquid–vapor two-phase system adiabatically expands at the final stage of the process (according to [15], the droplets with size $a < 10^{-5}$ cm are in thermodynamic equilibrium with the surrounding vapor), the mixture temperature decreases by ~4 kK, and the velocity increases by ~500 m/s. Therefore, the maximal velocity of adiabatic expansion of the two-phase system reaches ~700 m/s. This value is close to the value of ~900 m/s observed experimentally for the velocity of changing conductor radius at the instant of time $t \sim 6$ μs.

This work was supported by the Russian Foundation for Basic Research, project nos. 99-02-16596, 99-02-16619, and 00-15-96529.

REFERENCES

1. V. A. Burtsev, N. V. Kalinin, and A. V. Luchinskiĭ, *Electrical Explosion of Semiconductors and Its Application in Electrophysical Plants* (Énergoatomizdat, Moscow, 1990).
2. S. V. Lebedev and A. A. Savvatimskiĭ, Usp. Fiz. Nauk **144**, 273 (1984) [Sov. Phys. Usp. **27**, 749 (1984)].
3. V. S. Vorob'ev and S. P. Malyshenko, Zh. Éksp. Teor. Fiz. **111**, 2016 (1997) [JETP **84**, 1098 (1997)].
4. V. S. Vorob'ev, A. A. Eronin, and S. P. Malyshenko, Teplofiz. Vys. Temp. **39**, 101 (2001).

5. A. V. Bushman, I. V. Lomonosov, and V. E. Fortov, *Equations of Metal State under High Energy Densities* (IKhFCh Ross. Akad. Nauk, Chernogolovka, 1992).
6. S. I. Tkachenko, K. V. Khishchenko, V. S. Vorob'ev, *et al.*, Teplofiz. Vys. Temp. **39**, 728 (2001).
7. S. I. Tkachenko, K. V. Khishchenko, V. S.Vorob'ev, *et al.*, in *Physics of Extremal States of Mattes-2002* (Chernogolovka, 2002), p. 11.
8. S. V. Koval', N. I. Kuskova, and S. I. Tkachenko, Teplofiz. Vys. Temp. **35**, 876 (1997).
9. V. P. Skripov, *Metastable Liquid* (Nauka, Moscow, 1972).
10. V. K. Semenchenko, *Surface Phenomena in Metals and Alloys* (Gostekhizdat, Moscow, 1957).
11. V. E. Fortov and A. A. Leont'ev, Teplofiz. Vys. Temp. **14**, 711 (1976).
12. V. S. Vorob'ev and S. P. Malyshenko, Zh. Éksp. Teor. Fiz. **120**, 863 (2001) [JETP **93**, 753 (2001)].
13. B. M. Smirnov, Usp. Fiz. Nauk **170**, 495 (2000).
14. V. V. Valevich and V. S. Sedoĭ, Izv. Vyssh. Uchebn. Zaved., Fiz., No. 6, 70 (1998).
15. S. I. Anisimov, Ya. A. Imas, V. S. Romanov, and Yu. V. Khodyko, *High Power Radiation Action on Metals* (Nauka, Moscow, 1970).

Translated by V. Sakun

JETP Letters, Vol. 75, No. 8, 2002, pp. 378–382. Translated from Pis'ma v Zhurnal Éksperimental'noĭ i Teoreticheskoĭ Fiziki, Vol. 75, No. 8, 2002, pp. 450–454.

The Strong Effect of Three-Center Interactions on the Formation of Superconductivity with $d_{x^2-y^2}$ Symmetry in the *t–J** Model

V. V. Val'kov[1, 2]*, T. A. Val'kova[2], D. M. Dzebisashvili[1, 3], and S. G. Ovchinnikov[1, 2, 3]

[1] *Institute of Physics, Siberian Division, Russian Academy of Sciences, Krasnoyarsk, 660036 Russia*
**vvv@iph.krasn.ru*
[2] *Krasnoyarsk State Technical University, Krasnoyarsk, 660074 Russia*
[3] *Krasnoyarsk State University, Krasnoyarsk, 660075 Russia*
Received December 25, 2001; in final form, March 4, 2002

The effect of three-center interactions on the formation of a superconducting phase with $d_{x^2-y^2}$ symmetry is considered using the diagram technique for Hubbard operators and irreducible Green's functions. It is shown that these interactions lead to a decrease in T_c by a factor of several tens.© *2002 MAIK "Nauka/Interperiodica".*

PACS numbers: 74.20.De; 71.27.+a; 74.90.+n

1. It is known that, in spite of its relative simplicity, the Hubbard model [1] reflects the most essential feature of the behavior of an ensemble of strongly correlated electrons and is frequently used as a base model for constructing the effective Hamiltonian H_{eff} acting in a truncated Hilbert space. The expedience of constructing H_{eff} is determined by the possibility of explicitly obtaining interactions that open, for example, additional ways for Cooper instability. Thus, when the *t–J* model is derived [2, 3], an interaction leading to the magnetic mechanism of Cooper pairing is distinguished.

In this work, it is shown that the three-center interactions arising in constructing H_{eff} and having the same parametric smallness as exchange interactions radically affect the properties of the superconducting phase, decreasing (*by more than an order of magnitude*) T_c with model parameters remaining unchanged.

2. Using an atomic representation, let us write the Hamiltonian in the Hubbard model

$$H = H_0 + V,$$
$$H_0 = \sum_f \left\{ \sum_\sigma (\epsilon - \mu) X_f^{\sigma\sigma} + (2\epsilon + U - 2\mu) X_f^{22} \right\},$$
$$V = \sum_{fm\sigma} t_{fm} \{ X_f^{\sigma 0} X_m^{0\sigma} + X_f^{2\bar{\sigma}} X_m^{\bar{\sigma}2} + \sigma (X_f^{\sigma 0} X_m^{\bar{\sigma}2} + X_m^{2\bar{\sigma}} X_f^{0\sigma}) \}, \quad (1)$$

where H_0 takes into account contributions of one- and two-electron states on one site with energies ϵ and $2\epsilon + U$, respectively; U is the Coulomb interaction parameter between two electrons located on one site; and μ is the chemical potential of the system. The operator V describes the hopping of electrons within the lower and the upper Hubbard subbands and also hopping from one subband to another; X_f^{nm} are the Hubbard operators

$$X_f^{nm} \equiv |n, f\rangle\langle f, m|, \quad X_f^{nm}|p, f\rangle = \delta_{mp}|n, f\rangle. \quad (2)$$

The symbol σ in Eq. (1) designates the quantity that takes values ± 1 and corresponds to two possible projections of the electron spin moment $\bar{\sigma} = -\sigma$.

In addition to the energy parameters of the model, an essential factor is the electron concentration on a per-site basis $n = N_e/N$ (N_e is the total number of electrons in the system, N is the number of sites in the lattice). At $n < 1$ and large Coulomb repulsion $U \gg |t_{fm}|$, electrons will tend to fill the lower Hubbard subband. The effect of states with two electrons on one site can be taken into account by perturbation theory based on the use of the small parameter $|t_{fm}|/U \ll 1$. An elegant implementation of such a program is provided, for example, by perturbation theory in the operator form [4] indicating a particular algorithm for constructing the effective Hamiltonian.

In the case under consideration, H_{eff} acts in the Hilbert subspace containing no doubles. The contributions of double states are reflected in H_{eff} as additional terms that represent an operator series in increasing order of the smallness parameter. With an accuracy quadratic in

t_{fm}/U, the effective Hamiltonian is determined by the equation [4]

$$H_{\text{eff}} = PH_0P + PVP + PV(H_0 - E_0)^{-1}(PV - V)P, \quad (3)$$

where P is the operator of projection onto the Hilbert subspace without doubles. Using the multiplication rules for Hubbard operators $X_f^{nm}X_f^{lq} = \delta_{ml}X_f^{nq}$, we obtain

$$P = \Pi_f(X_f^{00} + X_f^{\uparrow\uparrow} + X_f^{\downarrow\downarrow}),$$
$$PVP - VP = -\sum_{fm\sigma} t_{mf}\sigma X_m^{2\bar{\sigma}}X_f^{0\sigma}P. \quad (4)$$

With regard to these relationships, we find the form of the third term in H_{eff},

$$PV(H_0 - E_0)^{-1}(PV - V)P$$
$$= P\sum_{fmg\sigma}\left(\frac{t_{fm}t_{mg}}{U}\right)(X_f^{\sigma 0}X_m^{\bar{\sigma}\sigma}X_g^{0\bar{\sigma}} - X_f^{\sigma 0}X_m^{\bar{\sigma}\bar{\sigma}}X_g^{0\sigma})P. \quad (5)$$

Addition of the first two terms from Eq. (3) leads to the following structure of H_{eff}:

$$H_{\text{eff}} = \sum_{f\sigma}(\epsilon - \mu)X_f^{\sigma\sigma} + \sum_{fm\sigma} t_{fm}X_f^{\sigma 0}X_m^{0\sigma}$$
$$+ \sum_{fmg\sigma}\left(\frac{t_{fm}t_{mg}}{U}\right)(X_f^{\sigma 0}X_m^{\bar{\sigma}\sigma}X_g^{0\bar{\sigma}} - X_f^{\sigma 0}X_m^{\bar{\sigma}\bar{\sigma}}X_g^{0\sigma}).$$

In this equation, the projection operator is omitted, because the Hilbert subspace of states without doubles is invariant with respect to the action of H_{eff}. Among others, the last summand in H_{eff} contains terms with $f = g$, which, taken together with the two first terms of H_{eff}, give the Hamiltonian of the t–J model

$$H_{t-J} = \sum_{f\sigma}(\epsilon - \mu)X_f^{\sigma\sigma} + \sum_{fm\sigma} t_{fm}X_f^{\sigma 0}X_m^{0\sigma}$$
$$+ \frac{1}{2}\sum_{fm\sigma} J_{fm}(X_f^{\sigma\bar{\sigma}}X_m^{\bar{\sigma}\sigma} - X_f^{\sigma\sigma}X_m^{\bar{\sigma}\bar{\sigma}}). \quad (6)$$

Thus, H_{eff} (thereafter H_{t-J^*}) can be written as

$$H_{t-J^*} = H_{t-J} + H_{(3)},$$
$$H_{(3)} = \sum_{\substack{fmg\sigma \\ f\neq g}}\left(\frac{t_{fm}t_{mg}}{U}\right)(X_f^{\sigma 0}X_m^{\bar{\sigma}\bar{\sigma}}X_g^{0\bar{\sigma}} - X_f^{\sigma 0}X_m^{\bar{\sigma}\bar{\sigma}}X_g^{0\sigma}). \quad (7)$$

Let us discuss the differences between H_{t-J^*} for the metallic phase and for the case of half-filling. At $n = 1$, each site is occupied by one electron. Therefore, the Hilbert subspace for H_{t-J^*} represents a set of homopolar states, when not only doubles but holes as well are absent. In this case, the projection operator can be written as $P = \Pi_f(X_f^{\uparrow\uparrow} + X_f^{\downarrow\downarrow})$, and, to a given accuracy, H_{t-J^*} is reduced to the Heisenberg model [5]. On the other hand, if $n < 1$, holes are present in the system. Therefore, electron hopping processes (the second term in Eq. (6)) and three-center interactions $H_{(3)}$ are included in H_{t-J^*}.

It is evident from Eq. (7) that the parametric smallness of three-center interactions $H_{(3)}$ is the same as for the exchange part of the t–J model, but it is considerably lower than for the kinetic part. This fact explains the smallness of the effect of $H_{(3)}$ on the spectral properties of the system in the normal phase [2, 3].

The situation is different when a superconducting state with the d-type symmetry of the order parameter (OP) is formed. In this case, the coupling constant in the superconducting phase $J \sim t^2/U$ is of the same order of magnitude as three-center interactions. This is why one should expect that $H_{(3)}$ will strongly affect superconductivity with the d-type symmetry of OP. Below, the truth of this statement will be confirmed by numerical calculations.

3. Two methods were used in the solution of the problem. In the first case, the diagram technique for the Hubbard operators [6, 7] was generalized to the case where three-center interaction is taken into account. In the second approach, the apparatus of two-time irreducible Green's functions was used in the same way as in the consideration of the t–J in [8, 9]. Self-consistent equations obtained within the above methods coincide completely.

The linearized system of equations for normal and anomalous Green's functions is reduced to the standard form of the Gor'kov equations:

$$(E - \tilde{\varepsilon}_{\mathbf{k}} + \mu)\langle\langle X_{\mathbf{k}\sigma}|X_{\mathbf{k}\sigma}^+\rangle\rangle$$
$$- \Delta_{\mathbf{k}}\langle\langle X_{-\mathbf{k}\bar{\sigma}}^+|X_{\mathbf{k}\sigma}^+\rangle\rangle = 1 - n/2,$$
$$-(\Delta_{\mathbf{K}})^*\langle\langle X_{\mathbf{k}\sigma}|X_{\mathbf{k}\sigma}^+\rangle\rangle$$
$$+ (E + \tilde{\varepsilon}_{\mathbf{k}} - \mu)\langle\langle X_{-\mathbf{k}\bar{\sigma}}^+|X_{\mathbf{k}\sigma}^+\rangle\rangle = 0. \quad (8)$$

In Eq. (8), the renormalized electron spectrum $\tilde{\varepsilon}_{\mathbf{k}}$ is described by the equation

$$\tilde{\varepsilon}_{\mathbf{k}} = \epsilon - \frac{n^2}{4}\frac{1 - n/4}{1 - n/2}J_0 + \left(1 - \frac{n}{2}\right)t_{\mathbf{k}} - \frac{n}{2}\left(1 - \frac{n}{2}\right)\frac{t_{\mathbf{k}}^2}{U}$$
$$- \frac{1}{N}\sum_{\mathbf{q}}\left\{t_{\mathbf{q}} + \frac{n}{2}J_{\mathbf{k}-\mathbf{q}} + [(2-n)t_{\mathbf{k}} + (1-n)t_{\mathbf{q}}]\frac{t_{\mathbf{q}}}{U}\right\}n_{\mathbf{q}\sigma}, \quad (9)$$

where the Fourier transform of the hopping integral $t_{\mathbf{q}} = 2t(\cos q_x + \cos q_y)$ is written in the nearest neighbor

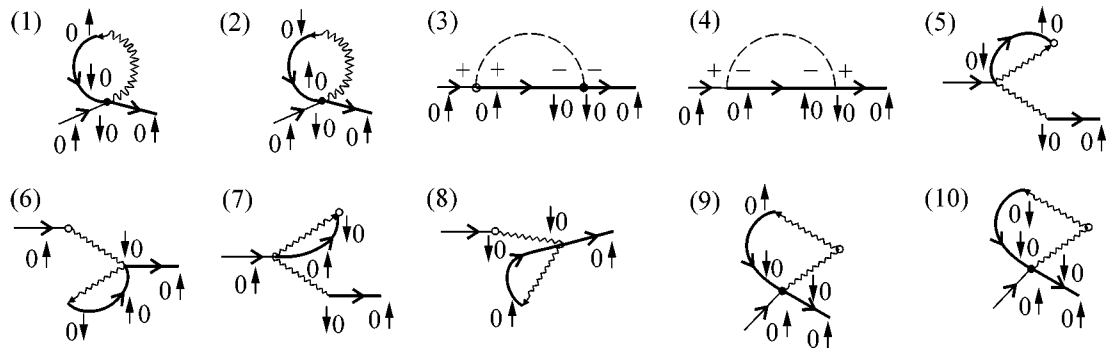

Fig. 1. Diagrams for the anomalous component of the mass operator in the *t–J** model.

approximation, $J_{\mathbf{q}} = (2t/U)t_{\mathbf{q}}$, and $n_{\mathbf{q}\sigma}$ is determined by the equation

$$n_{\mathbf{q}\sigma} = \frac{E_{\mathbf{q}} - \xi_{\mathbf{q}}}{2E_{\mathbf{q}}} + \frac{\xi_{\mathbf{q}}}{E_{\mathbf{q}}}(\exp(E_{\mathbf{q}}/T) + 1)^{-1}, \qquad \xi_{\mathbf{q}} = \tilde{\varepsilon}_{\mathbf{q}} - \mu. \tag{10}$$

Here, $E_{\mathbf{q}} = \sqrt{(\tilde{\varepsilon}_{\mathbf{q}} - \mu)^2 + |\Delta_{\mathbf{q}}|^2}$ is the spectrum of quasiparticle excitations, and $\Delta_{\mathbf{q}}$ designates the OP of the superconducting state.

To demonstrate the relative role of three-center interactions, the contributions of the mass operator $\Sigma_{0\uparrow,\downarrow 0}(\mathbf{p}, \omega_n)$ to the component are given. This contribution determines the superconducting order parameter. Ten graphs are shown in Fig. 1, whose analytical expressions in total determine

$$\Sigma_{0\uparrow,\downarrow 0}(\mathbf{p}, \omega_n) = -\frac{T}{N} \times \sum_{\mathbf{q}\omega_m} [2t_{\mathbf{q}} + (J_{\mathbf{p}+\mathbf{q}} + J_{\mathbf{p}-\mathbf{q}}) + A_{\mathbf{q}}^{(3)}] G_{0\uparrow,\downarrow 0}(\mathbf{p}, \omega_m), \tag{11}$$

$$A_{\mathbf{q}}^{(3)} = \left(1 - \frac{n}{2}\right)\frac{4t_{\mathbf{p}}t_{\mathbf{q}}}{U} - n\left(\frac{t_{\mathbf{q}}^2}{U} - \frac{J_0}{2}\right) - \left(1 - \frac{n}{2}\right)(J_{\mathbf{p}+\mathbf{q}} + J_{\mathbf{p}-\mathbf{q}}).$$

In Eq. (11), the contribution $\sim 2t_{\mathbf{q}}$ originates from the first two graphs and determines the kinematic mechanism [10]; the term in round brackets reflects the contribution determined by the third and fourth graphs [7] and is responsible for the magnetic mechanism of the *t–J* model. Finally, the term $\sim A_{\mathbf{q}}^{(3)}$ is induced by three-center interactions $H_{(3)}$ and is determined by the last six graphs in Fig. 1.

The last term in $\sim A_{\mathbf{q}}^{(3)}$ is the most significant factor for the *d*-symmetry OP. It leads in the total $\Sigma_{0\uparrow,\downarrow 0}$ to the renormalization of the coupling constant by the scenario $J \longrightarrow J[1 - (1 - n/2)] = (n/2)J$. It is this renormalization that determines the strong effect of $H_{(3)}$ on the formation of superconductivity with the *d* symmetry of OP. The self-consistent equation for OP can be found in the conventional way:

$$\Delta_{\mathbf{k}} = \frac{1}{N}\sum_{\mathbf{q}}\left\{2t_{\mathbf{q}} + \frac{n}{2}(J_{\mathbf{k}+\mathbf{q}} + J_{\mathbf{k}-\mathbf{q}}) + 4\left(1 - \frac{n}{2}\right)\frac{t_{\mathbf{k}}t_{\mathbf{q}}}{U} - n\left(\frac{t_{\mathbf{q}}^2}{U} - \frac{J_0}{2}\right)\right\}\left(\frac{\Delta_{\mathbf{q}}}{2E_{\mathbf{q}}}\right)\tanh\left(\frac{E_{\mathbf{q}}}{2T}\right).$$

There are two things distinguishing this equation from the corresponding equation for the *t–J* model. First, additional terms appear, which can be easily distinguished by the explicit dependence on the parameter *U*. The second distinction is more important and is associated with the renormalization of the coefficient before the terms $J_{\mathbf{k}\pm\mathbf{q}}$ indicated above.

4. Within the nearest neighbor approximation, the equation for OP possesses solutions differing in the symmetry types of the order parameter $\Delta_{\mathbf{k}}$. The solution with the *s* type of symmetry $\Delta_{\mathbf{k}} = \Delta_0$ does not obey the sum rule [9] and is not considered here. The solution with the *d* symmetry of OP $\Delta_{\mathbf{k}} = \Delta_0(\cos k_x - \cos k_y)$ is of prime interest. In this case, the equations for determining the temperature dependence $\Delta_0(T)$ and for calculating the critical temperature T_c can be written as follows:

$$1 = \frac{nJ}{2N}\sum_{\mathbf{q}}\frac{(\cos q_x - \cos q_y)^2}{E_{\mathbf{q}}}\tanh\left(\frac{E_{\mathbf{q}}}{2T}\right), \qquad 1 = \frac{nJ}{2N}\sum_{\mathbf{q}}\frac{(\cos q_x - \cos q_y)^2}{\tilde{\varepsilon}_{\mathbf{q}} - \mu}\tanh\left(\frac{\tilde{\varepsilon}_{\mathbf{q}} - \mu}{2T_c}\right). \tag{12}$$

The results of the numerical solution of the equation for T_c are given in Fig. 2 at various *n* for the *t–J** model (curve *2*). For comparison, the dependence of T_c on the electron concentration obtained without regard for $H_{(3)}$ is also given in this figure (curve *1*). The numerical cal-

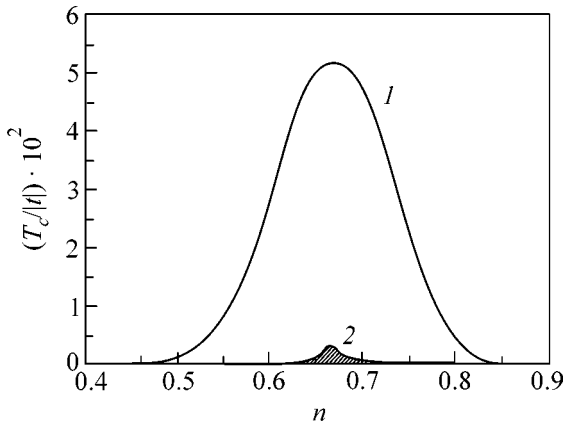

Fig. 2. Regions of the superconducting state in the (*1*) *t–J* and (*2*) *t–J** models.

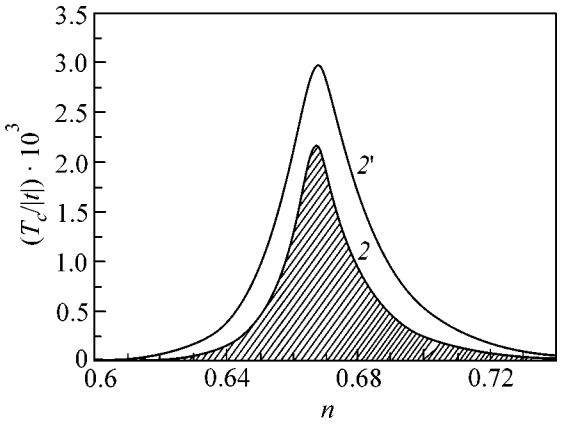

Fig. 3. Variations of T_c caused by the renormalization of the spectrum due to $H_{(3)}$.

culations were performed under the assumption that the ratio $2|t|/U$ equals 0.25. It is evident that the inclusion of $H_{(3)}$ leads to a significant decrease in the superconducting transition temperature (hatched region).

The decrease in the critical temperature caused by $H_{(3)}$ is due to two factors. The first (and the main) factor is in the renormalization of the coupling constant. The second factor is the additional renormalization of the electron energy spectrum. In order to demonstrate the role of the second factor, Fig. 3 displays (on an enlarged scale as compared with Fig. 2) the critical temperature in the *t–J** model as a function of electron concentration both with regard for the contributions of $H_{(3)}$ to the renormalization of the electron spectrum (curve *2*) and without these contributions (curve *2*'). It is evident that the second factor affects T_c much more weakly.

Figure 4 shows the dependence of T_c on the ratio $2|t|/U$ obtained without regard for three-center interactions (curve *1*) and with regard for these interactions (curve *2*). The electron concentration in the plots corresponds to the optimal doping level ($n = 0.665$). It is evident that, at $2|t|/U = 0.25$ (dashed lines), T_c obtained taking into account the effect of $H_{(3)}$ is 25 times smaller than T_c calculated without taking the three-center interactions into account.

5. In order to demonstrate clearly the physical nature of the renormalization of the coupling constant by three-center interactions obtained in this work, consider the action of the H_{t-J} and $H_{(3)}$ operators on a singlet pair. If there are no other electrons, the state of a system with this pair is described by the ket vector

$$|\psi(f, f+\Delta)\rangle = \frac{1}{\sqrt{2}}(X_f^{\uparrow 0}X_{f+\Delta}^{\downarrow 0} - X_f^{\downarrow 0}X_{f+\Delta}^{\uparrow 0})|0\rangle,$$

where $|0\rangle$ is the state without electrons. This pair corresponds to an eigenvector of H_{t-J}

$$H_{t-J}|\psi(f, f+\Delta)\rangle = (2\epsilon - 4t^2/U)|\psi(f, f+\Delta)\rangle.$$

After the action of $H_{(3)}$ on the singlet pair, a superposition of states is obtained:

$$H_{(3)}|\psi(f, f+\Delta)\rangle = (-2t^2/U)$$

$$\times \sum_{\Delta_1 \neq -\Delta} \{|\psi(f, f+\Delta_1)\rangle + |\psi(f+\Delta+\Delta_1, f+\Delta)\rangle\}.$$

It is evident that the effect of $H_{(3)}$ is reduced to rotations through the angles $\pi/2$, π, and $3\pi/2$ of the singlet pair under consideration around sites f and $f+\Delta$. It is essential that the energy parameter in this case equals $-2t^2/U$. Because of this, when the right-hand side of the last equation is written in the form that does not contain the restriction $\Delta_1 \neq \Delta$ (one has to make an operation of this

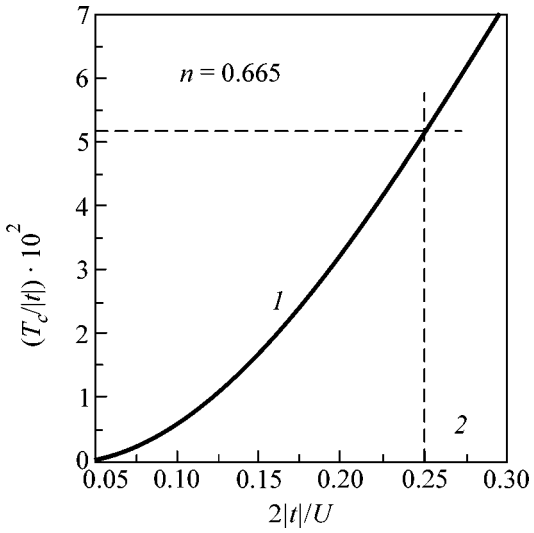

Fig. 4. Effect of $H_{(3)}$ on the dependence of T_c on the parameter $2t/U$.

kind when passing on to the Fourier representation), the term $(+4t^2/U)|\psi(f, f + \Delta)\rangle$ should be added, and this term fully compensates the action of the exchange part of the Hamiltonian H_{t-J}. Thus, it can be seen that three-center interactions make a significant contribution to the dynamics of singlet pairs, whose formation underlies the mechanism of superconducting pairing. Therefore, in the case where the system contains only one singlet pair, one can talk about the full compensation of the corresponding two-center terms of the effective Hamiltonian. If the system contains other electrons, three-center terms act in such a way that the states arising because of changes in the lattice sites adjacent to the singlet pair under consideration start to make a contribution to the resulting superposition. These additional contributions increase as electrons fill the sites adjacent to the pair. These circumstances explain the appearance of the concentration factor, which leads to the renormalization of the coupling constant mentioned above.

We note in conclusion that the analysis performed unambiguously points to the essential role of three-center interactions in the formation of a superconducting state with the *d*-type symmetry of OP. Since it was found that without $H_{(3)}$ $T_c \sim 100$ K at typical values of parameters [2], we found, with regard to these terms, that $T_c \sim 4$ K for the same parameters.

The authors are grateful to E.V. Kuz'min and V.I. Zinenko for useful discussions of the results of this work.

This work was supported by the Russian Foundation for Basic Research, project no. 00-02-16110, and by the Russian Foundation for Basic Research and KKFN "Eniseĭ," project no. 02-02-97705. One of the authors (D.M.D) is grateful for financial support from the Science Support Foundation, grant for talented young researchers.

REFERENCES

1. J. Hubbard, Proc. R. Soc. London, Ser. A **276**, 238 (1963).
2. Yu. A. Izyumov, Usp. Fiz. Nauk **167**, 465 (1997) [Phys. Usp. **40**, 445 (1997)].
3. S. G. Ovchinnikov, Usp. Fiz. Nauk **167**, 1043 (1997) [Phys. Usp. **40**, 993 (1997)].
4. N. N. Bogoliubov, *Lectures on Quantum Statistics* (Naukova Dumka, Kiev, 1949; Gordon and Breach, London, 1967).
5. É. L. Nagaev, *Magnetics with Compound Exchange Interactions* (Nauka, Moscow, 1988).
6. R. O. Zaĭtsev, Zh. Éksp. Teor. Fiz. **70**, 1100 (1976) [Sov. Phys. JETP **43**, 574 (1976)].
7. Yu. A. Izyumov, M. I. Katsnel'son, and Yu. N. Skryabin, *Magnetism of Collective Electrons* (Fizmatlit, Moscow, 1994).
8. N. M. Plakida, V. Yu. Yushankhay, and I. V. Stasyuk, Physica C (Amsterdam) **162–164**, 787 (1989).
9. V. Yu. Yushankhay, N. M. Plakida, and P. Kalinay, Physica C (Amsterdam) **174**, 401 (1991).
10. R. O. Zaĭtsev and V. A. Ivanov, Pis'ma Zh. Éksp. Teor. Fiz. **46** (S1), 140 (1987) [JETP Lett. **46**, S116 (1987)].

Translated by A. Bagatur'yants

JETP Letters, Vol. 75, No. 8, 2002, pp. 383–386. Translated from Pis'ma v Zhurnal Éksperimental'noĭ i Teoreticheskoĭ Fiziki, Vol. 75, No. 8, 2002, pp. 455–458.

Conductance of SIN and SIS Junctions with Chiral Superconductors

A. M. Bobkov

Lebedev Physical Institute, Russian Academy of Sciences, Moscow, 117924 Russia

e-mail: bobkov@lpi.ru

Received March 7, 2002

Low-temperature conductance peaks due to the surface Andreev bound states in SIN and SIS junctions with chiral superconductors are considered. It is shown that, in SIN junctions, the conductance as a function of voltage, $G(V)$, is highly sensitive to the dependence of the barrier transparency on the direction of the quasiparticle momentum. A weak magnetic field applied to the junction shifts the conductance peaks. In symmetric SIS junctions, the presence of chiral levels of Andreev bound states on both sides of the barrier gives rise to a conductance peak at $V = 0$. © *2002 MAIK "Nauka/Interperiodica".*

PACS numbers: 74.80.Fp; 74.70.Pq

Possible examples of chiral superconductors are Sr_2RuO_4 and the *B* phase of UPt_3. These compounds are characterized by highly anisotropic order parameters. The latter property is confirmed by the strong suppression of T_c by nonmagnetic impurities [1]. Muonic experiments testify to the presence of spontaneous magnetic fields and, hence, the spontaneous violation of time inversion in these superconductors [2].

The conductance of SIN junctions with superconductors characterized by anisotropic pairing was theoretically studied first in relation to high-T_c superconductors (see, e.g., [3]) and, later, in relation to chiral superconductors [4–6]. Experimentally, the conductance of SIN junctions with Sr_2RuO_4 was studied in [7]. The conductance of SIS junctions with anisotropic superconductors was experimentally studied in [8, 9]. The characteristic feature revealed in these experiments was the presence of a zero-bias conductance peak, which was found to grow lower and broader with increasing temperature.

In the analysis of the conductance behavior in [4–6], the barrier transparency was interpreted in terms of the simplest model of a δ-like barrier. Below, it is shown that the conductance as a function of voltage is highly sensitive to the particular dependence of the barrier transparency on the momentum direction. Therefore, the actual dependence of the barrier transparency on the momentum can fundamentally influence the interpretation of experimental data.

Let us consider an SIN junction. The *x* coordinate is directed along the normal to the tunneling barrier, and the chiral superconductor (S) is oriented so that the *c* axis of the crystal is directed along the *z* axis. For the quasiparticle current and, hence, the conductance in the tunneling junction, the following relationships are valid [3]:

$$j_x(V, T) = -\int\limits_{v_{f,x}>0} \frac{d\Omega}{4\pi} e N_f v_{f,x} D(\mathbf{p}_f) \times \int\limits_{-\infty}^{+\infty} d\varepsilon \left(\tanh\frac{\varepsilon + eV}{2T} - \tanh\frac{\varepsilon}{2T} \right) \nu_l(\mathbf{p}_f, \varepsilon), \quad (1)$$

$$G(V, T) = -\frac{e^2}{2T} \times \int\limits_{v_{f,x}>0} \frac{d\Omega}{4\pi} N_f v_{f,x} D(\mathbf{p}_f) \int\limits_{-\infty}^{+\infty} d\varepsilon \frac{\nu_l(\mathbf{p}_f, \varepsilon)}{\cosh^2\left(\frac{\varepsilon + eV}{2T}\right)}. \quad (2)$$

In Eqs. (1) and (2), the density of states in the superconductor, $\nu_l(\mathbf{p}_f, \varepsilon)$, is taken as in the case of an opaque boundary. Here and below, $e = -|e|$; $h = 1$; and $V = \Phi_r - \Phi_l$, where $\Phi_{r,l}$ represents the potentials to the left and to the right of the barrier. For simplicity, let us denote the quantity $|e|V$ by V, i.e., $eV \longrightarrow -V$, and normalize the conductance to the inverse normal resistance G_N of the junction (the NIN junction),

$$G_N = -2e^2 N_f \int\limits_{v_{f,x}>0} \frac{d\Omega}{4\pi} v_{f,v} D(\mathbf{p}_f). \quad (3)$$

It is also convenient to introduce the renormalized barrier transparency

$$\bar{D}(\mathbf{p}_f) = D(\mathbf{p}_f) \left(\int\limits_{v'_{f,x}>0} \frac{d\Omega}{4\pi} \frac{v'_{f,x}}{v_f} D(\mathbf{p}'_f) \right)^{-1}. \quad (4)$$

As a result, the conductance at zero temperature can be represented in the form

$$G(V, T = 0)/G_N = \int\limits_{v_{f,x}>0} \frac{d\Omega}{4\pi} \frac{v_{f,x}}{v_f} \bar{D}(\mathbf{p}_f) \nu_l(\mathbf{p}_f, V). \quad (5)$$

In chiral superconductors, near their surfaces, surface Andreev states are formed with the energies $\varepsilon_B(\mathbf{p}_f)$ [10]. Then, the density of states in a superconductor, $\nu_l(\mathbf{p}_f, \varepsilon)$, can be divided into two components:

$$\nu(\mathbf{p}_f, \varepsilon) = \tilde{g}(\mathbf{p}_f)\delta(\varepsilon - \varepsilon_B(\mathbf{p}_f)) + \nu_c(\mathbf{p}_f, \varepsilon). \quad (6)$$

Here, the first (δ-like) term describes the bound state, where $\tilde{g}(\mathbf{p}_f)$ represents the residue of the polar term of the quasiclassical Green's function and depends on both the suppression of the order parameter and the type of pairing in the superconductor. The second term in Eq. (6), $\nu_c(\mathbf{p}_f, \varepsilon)$, represents the component of the density of states corresponding to the continuous spectrum. This component is zero below the gap, and at $\varepsilon \gg |\Delta|$ it tends to the density of states of a normal metal: $\nu_c(\mathbf{p}_f, \varepsilon) \longrightarrow 1$. The quantity g is explicitly determined from the expression for the coordinate-dependent order parameter $\Delta(\mathbf{p}, x)$ [11]. The part of conductance corresponding to $\nu_c(\mathbf{p}_f, \varepsilon)$ contains no peaks in the case of chiral-type pairing. For the part of conductance corresponding to the bound states, the following expression is valid at $T = 0$:

$$G_B(V)/G_N = \int\limits_{v_{f,x}>0} \frac{d\Omega}{4\pi} \frac{v_{f,x}}{v_f} \bar{D}(\mathbf{p}_f) \tilde{g}(\mathbf{p}_f) \delta(V - \varepsilon_B(\mathbf{p}_f)). \quad (7)$$

For Sr_2RuO_4, the Fermi surface can be considered as cylindrical, and Eq. (7) can be integrated in the general form:

$$G_B(V)/G_N = \frac{1}{2\pi v_f} \sum_i \frac{\tilde{g}(v_{f,y})\bar{D}(v_{f,y})}{|\partial \varepsilon_{B,i}(v_{f,y})/\partial v_{f,y}|}. \quad (8)$$

Here, $v_{f,y}$ is determined from the equation $V = \varepsilon_B(v_{f,y})$, and the summation goes over all possible solutions for this equation. For a step model of the order parameter and a δ-like barrier, Eq. (8) takes the form of the expression obtained in [6]. However, one should note the crucial role played by the dependence of the barrier transparency on the direction at the Fermi surface. Conductance peaks occur at the voltages corresponding to the extrema of the bound-state energy: $\partial \varepsilon_{B,i}(v_{f,y})/\partial v_{f,y} = 0$. The direction φ corresponding to this energy is determined by the quantity v. For a δ-like barrier in the tunneling limit, the following dependence of the barrier transparency on the direction is obtained (the polar angle φ is measured in the xy plane relative to the normal): $D(\varphi) = D_0 \cos^2\varphi$. This $D(\varphi)$ dependence does not qualitatively affect the form of the $G(V)$ dependence. However, for the actual tunneling barrier, the range of angles φ for which the barrier transparency is not vanishingly small can be rather narrow. Then, the very possibility of the formation of conductance peaks depends on the value of $D(\varphi)$ in the direction corresponding to the extremum of $\varepsilon_B(v_{f,y})$. This can clearly be seen from Fig. 1, which shows the dependence of $G(V, T = 0)/G_N$ on $|e|V/\Delta_{\max}$ for an SIN junction with a superconductor characterized by the $f_{x^2-y^2}$-type pairing. In this case, the energy dispersion of the surface Andreev bound states is described by the expression $\varepsilon_B(\varphi) = \pm\Delta_{\max}|\cos(2\varphi)|\sin(\varphi)$ [10], and the corresponding conductance peak occurs at $|e|V/\Delta_{\max} \approx 0.27$. The barrier transparency is taken in the form $D(\varphi) = D_0 \exp(-A\sin^2\varphi)$. The order parameter is modeled by a step function, and a slight broadening of the bound levels is introduced: $\gamma = 0.01\Delta_{\max}$. One can see that, as the parameter A increases (i.e., the transparency cone decreases), the conductance peaks vanish. It should also be noted that the narrower the transparency cone of the barrier, the higher the central part of the dependence of G on the voltage. This occurs because at voltages close to zero, the conductance actually depends only on the absolute value of the barrier transparency along the normal, D_0, whereas the normalizing quantity G_N also depends on the cone angle of the barrier transparency region.

To take into account the effect of a weak magnetic field in the case $\xi \ll \lambda$, one can use the approximate expression

$$\varepsilon_B(\mathbf{p}_f) \longrightarrow \varepsilon_B(\mathbf{p}_f) + \frac{e v_y(\mathbf{p}_f)}{c} A_y(x = 0) = \varepsilon_B(\mathbf{p}_f) + \frac{v_y(\mathbf{p}_f)}{v_f} \varepsilon_M. \quad (9)$$

Generally speaking, it is necessary to include the spontaneous current in Eq. (9), which is always present at the surface of a chiral superconductor [12, 13, 10]. However, the estimate of ε_M made on the basis of numerical calculations [10] shows that the contribution of spontaneous currents to ε_M is small and $\varepsilon_M \sim 10^{-1}\frac{\xi}{\lambda}\Delta_{\max}$.

The Doppler shift of dispersionless zero levels in d-wave superconductors leads to a splitting of the conductance peak in a magnetic field [14]. When ε_B is initially characterized by a dispersion (which far exceeds ε_M in amplitude), the effect of the magnetic field manifests itself in a different way. For chiral types of pairing, for which no conductance peaks are observed (the p-type pairing with $\varepsilon_B = \Delta v_{f,y}/v_f$), the presence of a weak magnetic field cannot cause such peaks to appear and, hence, does not lead to any qualitative changes in the $G(V)$ dependence. However, if the $\varepsilon_B(v_{f,y})$ dependence has extrema at some points $v^0_{f,y}$ (as in the case of the f-

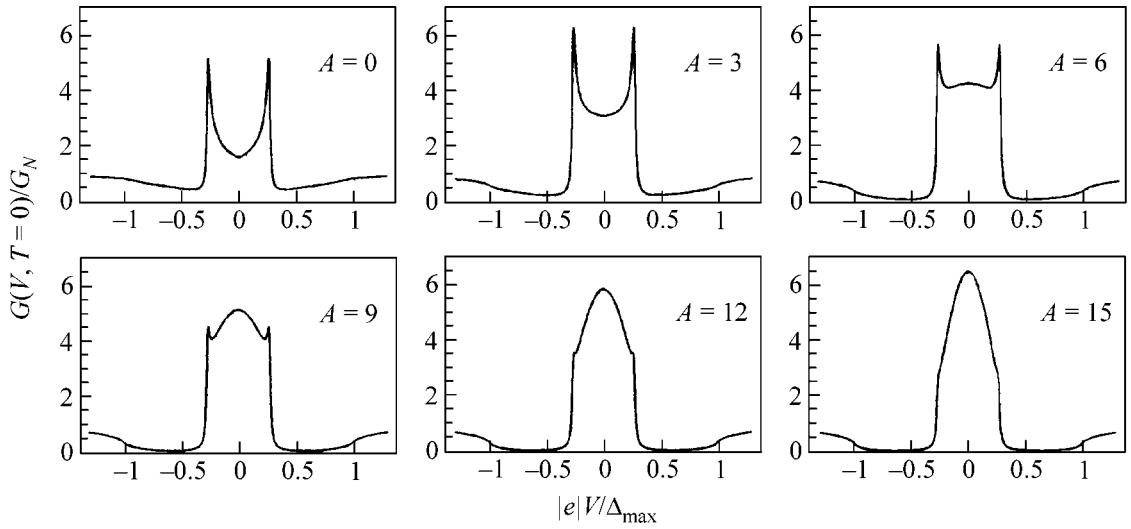

Fig. 1. Dependence of the conductance on the voltage for an SIN junction with a superconductor with the $f_{x^2-y^2}$-type pairing. The barrier transparency is determined as $D(\varphi) = D_0\exp(-A\sin^2\varphi)$. The plots correspond to different values of parameter A. The energy levels of the surface bound states have a finite width $\gamma = 0.01\Delta_{max}$.

type pairing), the conductance exhibits peaks at $V = \varepsilon_B(v^0_{f,y})$, and, in the presence of a weak magnetic field, the points corresponding to the peaks of $G(V)$ are displaced by the distance $V - V_0 \approx \varepsilon_M v^0_{f,y}/v_f$, which is proportional to the magnetic flux penetrating the superconductor. Figure 2 shows the changes in the $G(V, T = 0)/G_N$ dependence in the presence of a weak magnetic field in the superconductor resulting in $\varepsilon_M = \pm 0.1\Delta_{max}$.

Now, let us consider a symmetric SIS junction with two identical chiral superconductors. Although, on both sides of the barrier, the energy levels of the surface Andreev bound states strongly depend on the momentum direction, they can give rise to conductance peaks at zero voltage. The component of quasiparticle current determined by the presence of bound states on both sides of the barrier has the form

$$j_B(V, T) = -eN_f \int_{v_{f,x}>0} \frac{d\Omega}{4\pi} v_{f,x} D(\mathbf{p}_f)\tilde{g}_r(\mathbf{p}_f)\tilde{g}_l(\mathbf{p}_f) \times\left(\tanh\frac{\varepsilon_{B,r}(\mathbf{p}_f)}{2T} - \tanh\frac{\varepsilon_{B,l}(\mathbf{p}_f)}{2T}\right) \times\delta(\varepsilon_{B,r}(\mathbf{p}_f) - \varepsilon_{B,l}(\mathbf{p}_f) + V). \quad (10)$$

For the chiral superconductors under consideration, two cases are possible: either $\varepsilon_{B,l}(\mathbf{p}_f) = \varepsilon_{B,r}(\mathbf{p}_f) \neq 0$ when the chiralities on the two sides of the barrier are different [10], or $\varepsilon_{B,l}(\mathbf{p}_f) = -\varepsilon_{B,r}(\mathbf{p}_f) \neq 0$ when the chiralities are identical. In the first case, the aforementioned current component is zero, whereas, in the second case, for a cylindrical Fermi surface, the following expression is valid:

$$J_B(V, T) = -\frac{eN}{2\pi}\tanh\frac{V}{4T}\sum_i \frac{\tilde{g}^2(v_{f,y})D(v_{f,y})}{|\partial\varepsilon_{B,i}(v_{f,y})/\partial v_{f,y}|}, \quad (11)$$

where $v_{f,y}$ is determined from the equation $V = -2\varepsilon_{B,r}(v_{f,y})$. Thus, the presence of extrema in $\varepsilon_B(v_{f,y})$ gives rise to peaks not only in the conductance of a

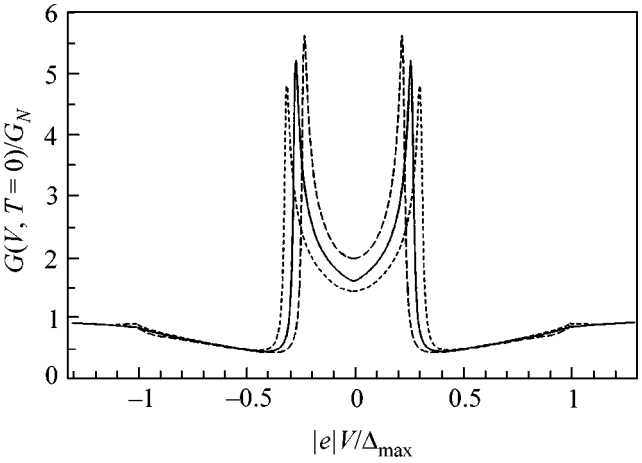

Fig. 2. Conductance for an SIN junction with a superconductor characterized by the $f_{x^2-y^2}$-type pairing in the presence of a weak magnetic field. The solid curve corresponds to zero magnetic flux through the superconductor, the dotted curve corresponds to the magnetic flux leading to $\varepsilon_M = +0.1\Delta_{max}$, and the dashed curve, to the magnetic flux giving $\varepsilon_M = -0.1\Delta_{max}$.

symmetric SIS junction but also in the quasiparticle current through it. At the same time, experimental observations revealed no double peaks for SIN junctions with Sr_2RuO_4. The absence of such peaks in the experiment argues against the presence of the *f*-type pairing (or any other pairing for which the derivative $\partial\varepsilon_{B,i}(v_{f,y})/\partial v_{f,y}$ becomes zero at some points) in Sr_2RuO_4. Another explanation is based on the considerable broadening of the bound states or on cutting off the peaks by a low barrier transparency in the corresponding directions. In addition, from Eq. (11), one can see that, for any type of chiral pairing, the conductance exhibits a zero-bias peak of width ~T and height ~1/T, which seems to agree well with the results obtained from the experiments [8, 9].

I am grateful to Yu.S. Barash for useful discussions. This work was supported by the Russian Foundation for Basic Research, project no. 02-02-16643.

REFERENCES

1. A. P. Mackenzie, R. K. W. Haselwimmer, A. W. Tyler, *et al.*, Phys. Rev. Lett. **80**, 161 (1998); Z. Q. Mao, Y. Mori, and Y. Maeno, Phys. Rev. B **60**, 610 (1999).
2. G. M. Luke, Y. Fudamoto, K. M. Kojima, *et al.*, Nature (London) **394**, 558 (1998).
3. Yu. S. Barash, A. A. Svidzinsky, and H. Burkhardt, Phys. Rev. B **55**, 15282 (1997).
4. M. Yamashiro, Y. Tanaka, and S. Kashiwaya, Phys. Rev. B **56**, 7847 (1997); M. Yamashiro, Y. Tanaka, Y. Tanuma, and S. Kashiwaya, J. Phys. Soc. Jpn. **67**, 3224 (1998); N. Yoshida, Y. Tanaka, J. Inoue, and S. Kashiwaya, J. Phys. Soc. Jpn. **68**, 1071 (1999); M. Yamashiro, Y. Tanaka, N. Yoshida, and S. Kashiwaya, J. Phys. Soc. Jpn. **68**, 2019 (1999).
5. C. Honerkamp and M. Sigrist, J. Low Temp. Phys. **111**, 895 (1998).
6. K. Sengupta, Hyok-Jon Kwon, and Victor M. Yakovenko, Phys. Rev. B **65**, 104504 (2002).
7. F. Laube, G. Goll, H. V. Löhneysen, *et al.*, Phys. Rev. Lett. **84**, 1595 (2000).
8. Z. Q. Mao, K. D. Nelson, R. Jin, *et al.*, Phys. Rev. Lett. **87**, 037003 (2001).
9. L. Alff, S. Kleefisch, U. Schoop, *et al.*, Eur. Phys. J. B **5**, 423 (1998).
10. Yu. S. Barash, A. M. Bobkov, and M. Fogelström, Phys. Rev. B **64**, 214503 (2001).
11. Yu. S. Barash, Phys. Rev. B **61**, 678 (2000).
12. G. E. Volovik, Pis'ma Zh. Éksp. Teor. Fiz. **66**, 492 (1997) [JETP Lett. **66**, 522 (1997)].
13. M. Matsumoto and M. Sigrist, J. Phys. Soc. Jpn. **68**, 994 (1999); **68**, 3120 (1999).
14. M. Fogelström, D. Rainer, and J. A. Sauls, Phys. Rev. Lett. **79**, 281 (1997).

Translated by E. Golyamina

JETP Letters, Vol. 75, No. 8, 2002, pp. 387–390. Translated from Pis'ma v Zhurnal Éksperimental'noĭ i Teoreticheskoĭ Fiziki, Vol. 75, No. 8, 2002, pp. 459–462.

Nonlinear Susceptibilities of a Weakly Disordered Uniaxial Ferromagnet in the Critical Region

D. V. Pakhnin[1]*, A. I. Sokolov[1], and B. N. Shalaev[2]

[1] *St. Petersburg State Electrotechnical University (LÉTI), St. Petersburg, 197376 Russia*

[2] *Ioffe Physicotechnical Institute, Russian Academy of Sciences, St. Petersburg, 194021 Russia*

**e-mail: ais@sokol.usr.etu.spb.ru*

Received March 11, 2002

For a weakly disordered three-dimensional Ising model in the critical region, the sixth-order effective coupling constant and the fourth- and sixth-order nonlinear susceptibilities are determined. The values of these quantities are found to differ radically (by a factor of 1.5–3) from the corresponding values in a pure ferromagnet, and their measurement is suggested for the identification of the critical behavior of impure systems.© *2002 MAIK "Nauka/Interperiodica".*

PACS numbers: 75.10.Hk; 75.40.Cx; 05.50.+q; 05.70.Jk

From the mid-1970s, the critical thermodynamics of three-dimensional impurity systems has been the object of intensive studies, both theoretical and experimental. Theoretical achievements, such as the determination of the mechanism governing the effect of impurities on the critical behavior, the formulation of the Harris criterion, the construction of the $\sqrt{\epsilon}$ expansion, and the calculation of the critical indices and critical amplitude ratios in the framework of the perturbation theory [1–13], have stimulated subsequent studies, the development of which in the last few years acquired the character of an explosion. Advancement in this field of research was, to some extent, caused by the discovery of the fact that, for the systems under discussion, an increase in the order of the renormalized perturbation theory does not lead to stabilization of the numerical results for the critical indices and other universal physical quantities. This feature is in contradiction with the known properties of renormalized group expansions for pure systems, which allow one, by applying the appropriate resummation procedures, to determine the universal parameters with an accuracy progressively increasing from order to order [14–22]. Most likely, the aforementioned anomaly, which manifests itself only in the five-loop and six-loop approximations [23–26], reflects the much discussed Borel nonsummability of renormalization group expansions for impurity systems (see, e.g., [27–29] and recent reviews [30–32]).

The absence of convergence of the iteration procedures based on the renormalization group theory of perturbations does not, however, preclude one from obtaining numerical estimates of the critical indices with an acceptable accuracy. The latter implies a relatively small scatter of the results obtained from different approximations, the insensitivity of the results to changes in the resummation technique, and, evidently, a good agreement between the theoretical predictions and the results of physical and computer experiments. For example, for the critical index of susceptibility γ of the impurity three-dimensional Ising model, the four-, five-, and six-loop approximations yield the values 1.326–1.321 [10, 11], 1.325 [25], and 1.330 [26], respectively, and the variations of γ in passing from one resummation technique to another do not exceed 0.01. This suggests that the field-theoretical renormalization group method can be used for calculating other universal critical parameters of three-dimensional impurity systems.

Below, we determine the nonlinear susceptibilities of the fourth (χ_4) and sixth (χ_6) orders and the effective coupling constant v_6 for a weakly disordered three-dimensional Ising ferromagnet in the critical region. At $T \longrightarrow T_c$, these quantities, just like the linear susceptibility χ and other equilibrium parameters, take on universal asymptotic values, which can be measured with high accuracy in modern experiment.

The free energy of a uniaxial ferromagnet as a function of magnetization M in an external magnetic field H can be represented in the form

$$F(M, m) = F(0, m) + \frac{1}{2}m^{2-\eta}M^2 + m^{1-2\eta}v_4M^4 + m^{-3\eta}v_6M^6 + \ldots - HM, \quad (1)$$

where m is the inverse correlation radius, η is the Fisher index, and v_4 and v_6 are the effective coupling constants taking universal critical values at the Curie point.

Using expansion (1), one can easily express the nonlinear susceptibilities χ_4 and χ_6 in terms of χ, v_4, and v_6:

$$\chi_4 = \left.\frac{\partial^3 M}{\partial H^3}\right|_{H=0} = -24\xi^2 m^{-3} v_4,$$
$$\chi_6 = \left.\frac{\partial^5 M}{\partial H^5}\right|_{H=0} = 720\chi^3 m^{-6}(8v_4^2 - v_6). \quad (2)$$

Thus, the determination of the nonlinear susceptibilities in the critical region is reduced to the calculation of the universal asymptotic values of v_4 and v_6.

For weakly disordered systems, the thermodynamic quantities are determined by averaging over random impurity configurations. This averaging is most simply performed by the replica technique. The latter is based on the fluctuation Hamiltonian of the *n*-vector cubic model

$$H = \int d^3x \left[\frac{m_0^2\varphi_\alpha^2 + (\nabla\varphi_\alpha)^2}{2} + u_4^{(0)}\varphi_\alpha^2\varphi_\beta^2 + v_4^{(0)}\varphi_\alpha^4\right], \quad (3)$$

which, in the limit $n \longrightarrow 0$, reproduces the critical behavior of the impurity Ising model. This behavior is controlled by the fixed impurity point of the renormalization group equations. The point in question is a stable node in the (u_4, v_4) plane, and its coordinates are known in the highest approximation available, i.e., in the six-loop approximation [26]. It is essential that the case of a nonzero external magnetic field corresponds to the *n*-component cubic model in a uniform field directed along the principal diagonal of the hypercube. It can be shown that, for the solution that does not violate the replica symmetry, the coupling constant u_4 drops out of the equation of state in the limit $n \longrightarrow 0$. From the physical point of view, this is quite important, because, in this case, the "wrong" sign of u_4 does not lead to the instability of the effective Hamiltonian.

Thus, at the Curie point, the effective fourth-order coupling constant in Eq. (1) is equal to the coordinate v_4^* of the fixed impurity point. Hence, the asymptotic behavior of χ_4 at $T \longrightarrow T_c$ is determined by the quantity v_4^*. The situation with the nonlinear susceptibility χ_6 is more complicated. The determination of its critical asymptotic behavior involves the calculation of the effective coupling constants u_6, q_6, and v_6 for the model given by Eq. (3). These constants act as coefficients of the invariants $M_\alpha^2 M_\beta^2 M_\gamma^2$, $M_\alpha^4 M_\beta^2$, and M_α^6 in the expansion of the free energy of the cubic model. Recently, the quantities u_6, q_6, and v_6 were determined in the form of renormalized perturbative series expansions in the four-loop approximation [33]. For the $O(n)$-symmetric systems, the series of length as large as this allow one to calculate the universal values of the sixth-order coupling constant with an accuracy no lower than 1% [19, 22]. Since the expression for χ_6 involves only one of the three coupling constants, namely, v_6, we present the renormalization group expansion only for this constant. In the limit $n \longrightarrow 0$, the expansion has the form

$$\frac{v_6}{v_4^2} = \frac{9}{\pi}(2u_4 + v_4 - 2.9001567u_4^2 - 3.1830989u_4v_4 - 0.9549296v_4^2 + 5.579725u_4^3 + 10.03487u_4^2v_4 + 6.222000u_4v_4^2 + 1.389963v_4^3 - 12.5233u_4^4 - 31.7631u_4^3v_4 - 30.6484u_4^2v_4^2 - 13.8874u_4v_4^3 - 2.50173v_4^4). \quad (4)$$

Note that the quantities u_4 and v_4 differ by a factor of $\pi/4$ from their analogs u and v used in [33].

Series (4) is of the asymptotic type. However, series of this kind allow one to obtain reliable quantitative results by applying the appropriate resummation techniques. One of them is used in our calculations in [11]. At the first step, expansion (4) is transformed to a convergent series with the help of the Borel–Leroy generalized transformation

$$f(u, v) = \sum_{ij} c_{ij}u^i v^j = \int_0^\infty e^{-t}t^b F(ut, vt)dt,$$
$$F(x, y) = \sum_{ij}\frac{c_{ij}x^i y^j}{(i + j + b)!}. \quad (5)$$

Then, using the Borel transform of the initial function, we construct an auxiliary series

$$\tilde{F}(x, y, \lambda) = \sum_{n=0}^{\infty}\lambda^n\sum_{l=0}^{n}\frac{c_{l,n-l}x^l y^{n-l}}{n!}, \quad (6)$$

with the coefficients as homogeneous polynomials in the variables u_4 and v_4. To perform analytic continuation beyond the circle of convergence, Padé approximants $[L/M]$ in the variable λ are used, the value of this variable being set equal to unity at the terminal step. The described resummation procedure retains all point symmetry properties of the initial expansions [34] and provides rapid convergence of the iteration process if the Borel summability of the renormalized group series takes place.

Since the parenthetical expression in Eq. (4) is a fourth-order polynomial, we can construct four different Padé approximants: [3/1], [2/2], [1/3], and [0/4]. It is well known that the diagonal approximants ($L = M$) or approximants close to them possess the best approximating properties. However, with an increase in the denominator exponent M, the number of the approximant poles in the complex plane also increases, and

Table

b		0	1	2	3	5	10	15	20
$u_4^* = -0.50$,	[2/2]	2.056	–	–	–	2.161	2.120	2.109	2.103
$u_4^* = 1.53$	[3/1]	2.319	2.255	2.216	2.190	2.156	2.117	2.100	2.090
(6-loop)	[2/1]	1.960	2.033	2.072	2.095	2.123	2.153	2.165	2.172
$u_4^* = -0.53$,	[2/2]	2.062	–	–	–	–	2.150	2.135	2.127
$u_4^* = 1.57$	[3/1]	2.364	2.296	2.255	2.226	2.191	2.149	2.131	2.120
(6-loop)	[2/1]	1.957	2.034	2.074	2.099	2.129	2.160	2.172	2.180
$u_4^* = -0.56$,	[2/2]	1.867	–	–	–	–	1.995	1.973	1.963
$u_4^* = 1.58$	[3/1]	2.188	2.125	2.087	2.061	2.028	1.990	1.973	1.963
(5-loop)	[2/1]	1.762	1.834	1.871	1.895	1.922	1.951	1.963	1.969

when these poles fall on the positive real semiaxis or close to it, they can make the approximant unsuitable for series summation. Therefore, in the resummation of expansion (4), we use only approximants [3/1] and [2/2]. In addition, our analysis also includes approximant [2/1], which practically corresponds to the use of the three-loop approximation. The above operations are directed toward the aim of revealing the sensitivity of the numerical results to the approximation order and to obtain additional information for the optimization of the resummation procedure by choosing the optimal value of the free parameter b in the Borel–Leroy transformation.

The results of our calculations are shown in the table, which presents the effective coupling constant v_6 as a function of the parameter b. The values of v_6 are determined at the fixed impurity point using the three aforementioned Padé approximants. Since the coordinates of the fixed impurity point, u_4^* and v_4^*, are known with a limited accuracy, we calculated the universal critical value of v_6 for three sets of u_4^* and v_4^*. The first two of them ($u_4^* = -0.50$, $v_4^* = 1.53$ and $u_4^* = -0.53$, $v_4^* = 1.57$) are obtained in the six-loop approximation with the use of two different resummation strategies [26], and the third set ($u_4^* = -0.56$, $v_4^* = 1.58$) is determined from the five-loop expansions subjected to the resummation by the Padé–Borel–Leroy method [25]. The empty cells in the table mean that, for the corresponding values of b, the Padé approximant [2/2] has "dangerous" poles.

As one can see from the table, the numerical values of v_6 obtained with the three chosen Padé approximants weakly depend on the parameter b, and, for each set of u_4^* and v_4^*, one can easily determine the optimal value of b at which the three approximants yield coincident or very close results. This fact points to the high efficiency of the resummation technique used in our calculations. The analysis of the data presented in the table shows that three variants of the coordinates taken for the fixed impurity point correspond to the estimates $v_6 = 2.14$, 2.15, and 1.96, respectively. Since the coordinates u_4^*, v_4^* determined from the six-loop approximation should be considered as the most reliable ones and the processing of the divergent series (4) can hardly provide an accuracy better than to the second decimal place, we accept the following final result of our calculations:

$$v_6 = 2.1 \pm 0.2. \quad (7)$$

The chosen error limits are rather conservative, and, hence, the true asymptotic value of v_6 is certain to lie within the interval bounded by Eq. (7).

It is of interest to compare the universal critical value of v_6 for the impurity Ising model with its analog for a pure (defect-free) system. The factor that really characterizes the contribution of the effective coupling constant v_6 to the equation of state is the ratio v_6/v_4^2. Taking the average value $v_4^* = 1.55$ as the coordinate of the fixed impurity point, we obtain the following ratio for the disordered Ising model at the critical point: $v_6/v_4^2 = 0.87$. For a pure uniaxial ferromagnet, the corresponding ratio is $v_6/v_4^2 = 1.64$–1.65 [17, 18, 35–38]. Thus, the impurities reduce this ratio almost by half. Since the ratio under discussion appears in the equation of state and, hence, is available for experimental study, the measurement of v_6/v_4^2 can be used to identify the critical behavior of impurity systems.

An equally great difference is observed between the nonlinear susceptibilities of impurity and pure Ising ferromagnets. For the three-dimensional Ising model, we have $v_4^* = 0.99$ [14, 15, 17, 18]. Then, according to the first expression in Eqs. (2), the value of the universal

combination $\chi_4\chi^{-2}m^3$ calculated for an impurity ferromagnet is 55–60% greater than for a pure ferromagnet. The difference in the sixth-order nonlinear susceptibilities is even more substantial. According to Eqs. (2), for a pure uniaxial ferromagnet, we have $\chi_6\chi^{-3}m^6 = 4.5 \times 10^3$, whereas for a weakly disordered system, we have $\chi_6\chi^{-3}m^6 = 12.3 \times 10^3$. This almost threefold change in the parameter $\chi_6\chi^{-3}m^6$ under the effect of impurities can certainly be detected experimentally.

This work was supported by the Russian Foundation for Basic Research (project nos. 01-02-17048, 01-02-17794) and the Ministry of Education of the Russian Federation (project no. E00-3.2-132). A.I. Sokolov and D.V. Pakhnin are also grateful to the International Science Foundation and the St. Petersburg City Administration for financial support in the framework of individual projects (nos. p2001-90 and s2001-1002).

REFERENCES

1. A. B. Harris and T. C. Lubensky, Phys. Rev. Lett. **33**, 1540 (1974).
2. A. B. Harris, J. Phys. C **7**, 1671 (1974).
3. T. C. Lubensky, Phys. Rev. B **11**, 3573 (1975).
4. D. E. Khmel'nitskiĭ, Zh. Éksp. Teor. Fiz. **68**, 1960 (1975) [Sov. Phys. JETP **41**, 981 (1975)].
5. B. N. Shalaev, Zh. Éksp. Teor. Fiz. **73**, 2301 (1977) [Sov. Phys. JETP **46**, 1204 (1977)].
6. C. Jayaprakash and H. J. Katz, Phys. Rev. B **16**, 3987 (1977).
7. A. I. Sokolov and B. N. Shalaev, Fiz. Tverd. Tela (Leningrad) **23**, 2058 (1981) [Sov. Phys. Solid State **23**, 1200 (1981)].
8. G. Jug, Phys. Rev. B **27**, 609 (1983).
9. I. O. Maĭer and A. I. Sokolov, Fiz. Tverd. Tela (Leningrad) **26**, 3454 (1984) [Sov. Phys. Solid State **26**, 2076 (1984)].
10. I. O. Mayer, A. I. Sokolov, and B. N. Shalaev, Ferroelectrics **95**, 93 (1989).
11. I. O. Mayer, J. Phys. A **22**, 2815 (1989).
12. N. A. Shpot, Zh. Éksp. Teor. Fiz. **98**, 1762 (1990) [Sov. Phys. JETP **71**, 989 (1990)].
13. C. Bervillier and M. Shpot, Phys. Rev. B **46**, 955 (1992).
14. G. A. Baker, Jr., B. G. Nickel, and D. I. Meiron, Phys. Rev. B **17**, 1365 (1978).
15. J. C. Le Guillou and J. Zinn-Justin, Phys. Rev. B **21**, 3976 (1980).
16. S. A. Antonenko and A. I. Sokolov, Phys. Rev. E **51**, 1894 (1995).
17. R. Guida and J. Zinn-Justin, Nucl. Phys. B **489**, 626 (1997).
18. R. Guida and J. Zinn-Justin, J. Phys. A **31**, 8103 (1998).
19. A. I. Sokolov, Fiz. Tverd. Tela (St. Petersburg) **40**, 1284 (1998) [Phys. Solid State **40**, 1169 (1998)].
20. H. Kleinert, Phys. Rev. D **57**, 2264 (1998).
21. H. Kleinert, Phys. Rev. D **60**, 085001 (1999).
22. A. I. Sokolov, E. V. Orlov, V. A. Ul'kov, and S. S. Kashtanov, Phys. Rev. E **60**, 1344 (1999).
23. B. N. Shalaev, S. A. Antonenko, and A. I. Sokolov, Phys. Lett. A **230**, 105 (1997).
24. R. Folk, Yu. Holovatch, and T. Yavors'kii, Phys. Rev. B **61**, 15114 (2000).
25. D. V. Pakhnin and A. I. Sokolov, Phys. Rev. B **61**, 15130 (2000); Pis'ma Zh. Éksp. Teor. Fiz. **71**, 600 (2000) [JETP Lett. **71**, 412 (2000)].
26. A. Pelissetto and E. Vicari, Phys. Rev. B **62**, 6393 (2000).
27. A. J. Bray, T. McCarthy, M. A. Moore, *et al.*, Phys. Rev. B **36**, 2212 (1987).
28. A. J. McKane, Phys. Rev. B **49**, 12003 (1994).
29. G. Alvarez, V. Martin-Mayor, and J. Ruiz-Lorenzo, J. Phys. A **33**, 841 (2000).
30. A. Pelissetto and E. Vicari, Phys. Rep. (in press); cond-mat/0012164 (2000).
31. R. Folk, Yu. Holovatch, and T. Yavors'kii, cond-mat/0106468 (2001).
32. Yu. Holovatch, V. Blavats'ka, M. Dudka, *et al.*, cond-mat/0111158 (2001).
33. D. V. Pakhnin and A. I. Sokolov, Phys. Rev. B **64**, 094407 (2001).
34. S. A. Antonenko and A. I. Sokolov, Phys. Rev. B **49**, 15901 (1994).
35. A. I. Sokolov, E. V. Orlov, and V. A. Ul'kov, Phys. Lett. A **227**, 255 (1997).
36. P. Butera and M. Comi, Phys. Rev. E **55**, 6391 (1997).
37. A. Pelissetto and E. Vicari, Nucl. Phys. B **522**, 605 (1998).
38. M. Campostrini, A. Pelissetto, P. Rossi, *et al.*, Phys. Rev. E **60**, 3526 (1999).

Translated by E. Golyamina

JETP Letters, Vol. 75, No. 8, 2002, pp. 391–394. Translated from Pis'ma v Zhurnal Éksperimental'noĭ i Teoreticheskoĭ Fiziki, Vol. 75, No. 8, 2002, pp. 463–466.

Far Infrared Electroluminescence in Cascade Type-II Heterostructures

Yu. B. Vasil'ev*, V. A. Solov'ev, B. Ya. Mel'tser, A. N. Semenov, S. V. Ivanov, Yu. L. Ivanov, and P. S. Kop'ev

Ioffe Physicotechnical Institute, Russian Academy of Sciences, St. Petersburg, 194021 Russia

**e-mail: Yu.Vasilyev@pop.ioffe.rssi.ru*

Received March 14, 2002

Far infrared radiation from type-II heterostructures is observed. The samples used for the observations have the form of ten-period cascade structures, each period containing InAs and AlGaAsSb quantum wells separated by a variband barrier. The results of studying the vertical transport and the electroluminescence testify that the radiation is caused by transitions between the electron and hole states existing in the adjacent quantum wells.

PACS numbers: 78.60.Fi; 78.66.Fd

In the last few years, one of the topical problems of the quantum cascade laser design has been related to the generation of long-wave radiation [1]. A recent achievement consisted in the development of a quantum cascade laser on intersubband transitions with a wavelength up to 24 μm [2]. However, attempts to extend the concepts used in the design of short-wave cascade lasers to the terahertz region have remained unsuccessful. The only advancement was the observation of a rather low-power spontaneous electroluminescence with a wavelength of about 100 μm [3–5]. A modification of the quantum cascade laser is the bipolar cascade laser based on type-II heterostructures with a band discontinuity [6]. This laser combines the advantages of injection and unipolar cascade lasers. The active region of this device consists of two quantum wells, namely, InAs and GaAs wells with electrons and holes, respectively, whose energy spectra overlap. When a bias voltage is applied to the structure, electrons are injected into the InAs well, where they recombine with holes. This leads to a photon emission due to the transitions between the electron and hole levels existing in the adjacent wells. The structure of the bipolar cascade laser provides radiation with a wavelength of about 4 μm.

In this paper, we report the development of bipolar cascade type-II heterostructures in which the spacing between the 2D electron and hole layers decreases when a bias voltage is applied. These structures produce an intense radiation at voltages exceeding a certain threshold. We present the results of an experimental study of the electric and radiative characteristics of these structures. The characteristics show that the radiation observed in the experiment is associated with electron–hole recombination between adjacent wells.

The active region of the proposed device is represented by InAs and $Al_{0.1}Ga_{0.9}AsSb$ quantum wells, which are characterized by n- and p-type conduction, respectively, and separated by a variband semiconductor barrier. Unlike conventional quantum cascade lasers, the structures with variband barriers can operate without satisfying the condition requiring that the parameters of all periods be identical, because the "adjustment" of the active region levels occurs automatically through the redistribution of voltage when the tunneling conductance of the barriers varies [7].

The samples were grown by molecular beam epitaxy on (100) p^+-GaSb substrates with the use of a Riber 32 system supplied by a standard arsenic source and a cracking source of antimony. The active region of the structure was deliberately left undoped. Each period included an $Al_xGa_{1-x}AsSb$ variband barrier layer that was matched as a whole with GaSb in the lattice constant, a 17-nm-thick InAs quantum well, and a 10-nm-thick $Al_{0.1}Ga_{0.9}AsSb$ quantum well with a constant composition. The active region lay between two p^+-GaSb layers, which were doped with beryllium to 2×10^{18} cm^{-3}. The thickness of the lower layer was 0.1 μm, and that of the upper layer, 0.5 μm. The samples had the form of rectangles with side lengths of several hundred microns. To obtain the radiation, rectangular voltage pulses were supplied to the sample with the relative pulse duration equal to two and a repetition rate of 1010 Hz (the duration of one pulse was 910 μs) at $T = 4.2$ K. The radiation from the structure was detected by a copper-doped germanium photodetector. The sensitivity range of the photodetector extended from several microns to 30 μm, with maximal sensitivity at a wavelength of 24 μm. The current–voltage char-

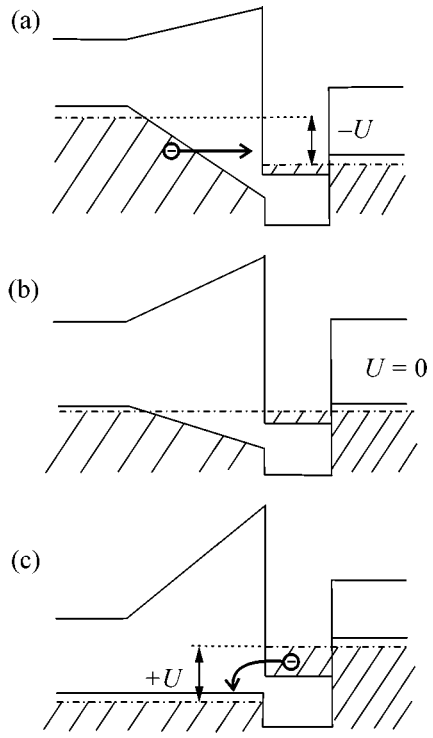

Fig. 1. Schematic band diagram of one period of the proposed structure for different polarities of the bias voltage: (a) reverse, (b) zero, and (c) forward.

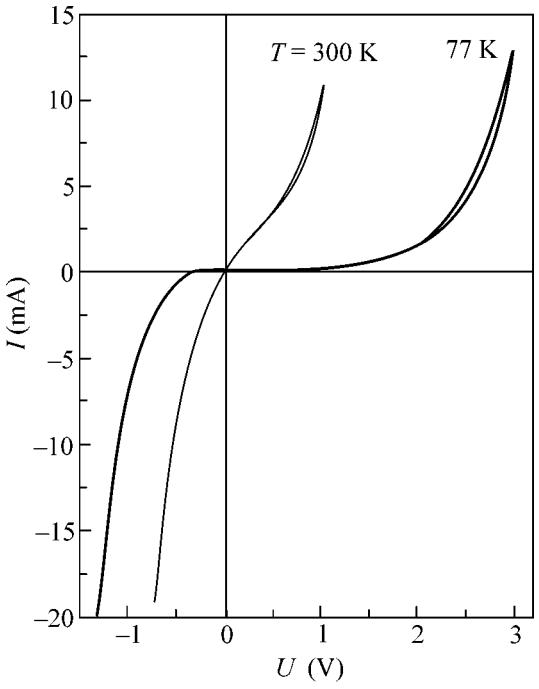

Fig. 2. Current–Voltage characteristics of the structure for two different temperatures, 77 and 300 K.

acteristics were recorded by a characteriograph in the pulsed mode of operation, simultaneously with the radiation, at different temperatures.

Figure 1 schematically represents the band diagram of one period of the structure for different polarities of the bias voltage. The major voltage drop occurs at the barriers, because the tunneling conductance of the barriers is much smaller than the conductance of the layers containing the charge carriers. As in the case of a tunnel diode, the reverse bias corresponds to the situation where the negative potential is applied to the hole layer (Fig. 1a). Typical current–voltage characteristics obtained at $T = 77$ and 300 K are shown in Fig. 2. With an increase in the reverse bias, the current exponentially grows. According to Fig. 1a, this result can be explained as follows: as the reverse bias increases, the slope of the triangular barrier increases in such a way that the "effective" barrier thickness decreases, which leads to an increase in the number of states allowing the tunneling of carriers through the barriers into the adjacent layer. At the same time, the steep growth of the current with temperature shows that, at high temperatures, the major contribution to the current comes from the thermal component rather than from the tunneling one. As follows from Fig. 1c, when a forward voltage is applied, one should expect a radically different form of the current–voltage characteristics. At small positive voltages, no current should flow through the structure because of the absence of allowed states in the adjacent wells, through which the forward tunneling could occur. As the voltage increases, the slope of the variband barrier decreases and the spacing between the electron and hole layers decreases. At some threshold voltage which is approximately equal to the initial barrier height multiplied by the number of periods, the valence band of all barriers becomes completely straightened out and the electron and hole layers become separated by only a thin interface layer. In this case, if the overlap of the electron and hole wave functions is strong enough for the electron–hole recombination to occur between the adjacent wells, one should observe a sharp increase in the current. In fact, as one can see from Fig. 2, at small positive voltages, the current is practically absent, whereas it exhibits considerable growth near a voltage of 2.3 V. The latter voltage is somewhat higher than the value calculated as the product of the barrier height (which, for the structure under study, is estimated at 0.08 eV) by the number of periods. Current–voltage characteristics of this kind are observed only at temperatures no higher than $T = 77$ K, where the contribution of the thermal current is insignificant.

The sharp current increase at forward voltages exceeding the threshold value indirectly points to the appearance of electron–hole recombination. One can expect that this recombination is of a radiative character. In the experiment, the radiation was recorded by the Ge:Cu photodetector when voltage pulses were applied to the structure. Figure 3 shows the dependences of the

radiation intensity and the current strength on the forward voltage. The radiation and the current behave in the same way. One can see that, when the voltage exceeds the threshold value, both radiation and current sharply increase within a narrow voltage interval. This behavior indicates that, when the voltage is applied, the spacing between the electron and hole layers decreases and, after the electron and hole wave functions overlap, a sharp increase in the rate of radiative recombination between the layers takes place. The forward branch of the current–voltage characteristic is similar to that measured at $T = 77$ K. This means that the current–voltage characteristics of the device do not change within the temperature interval from 4.2 to 77 K, and one can expect that the radiative characteristics will also exhibit no considerable changes with a temperature increase up to 77 K.

The dependence of the radiation intensity on the current strength (the inset in Fig. 3) has two specific features. First, one can clearly see the cutoff current below which no radiation from the structure can be detected (for the sample under study, this current is equal to 2 mA and the corresponding current density is ~2 A/cm^2). Presumably, the thermal current component, which makes no contribution to the radiation, does not completely vanish even at $T = 4.2$ K. Second, the radiation intensity linearly depends on the pumping current. This means that the radiation is not related to heating, because, if this were so, a square-law dependence of the radiation intensity on the current would be observed. With an increase in the current, the signal-to-noise ratio increases and, at the maximal currents studied in the experiment (25 mA), becomes greater than 100. It is significant that, for the reverse polarity of the bias voltage, no signal was detected at the same current strength values. It is possible to roughly estimate the radiation wavelength, because the sensitivity range of the photodetector is known. This estimate agrees well with our assumption that the radiation is caused by the optical transitions between the electron and hole states of the adjacent wells. Namely, in this case, the radiation wavelength should somewhat exceed the height of the variband barrier, with allowance for the energy quantization in the quantum wells, which yields a wavelength of ~ 12 μm. Since the exact value of the variband barrier height is unknown, all estimates presented here are fairly rough. The data that are necessary to confirm our estimate can be obtained from spectral measurements, which will be the subject of another study.

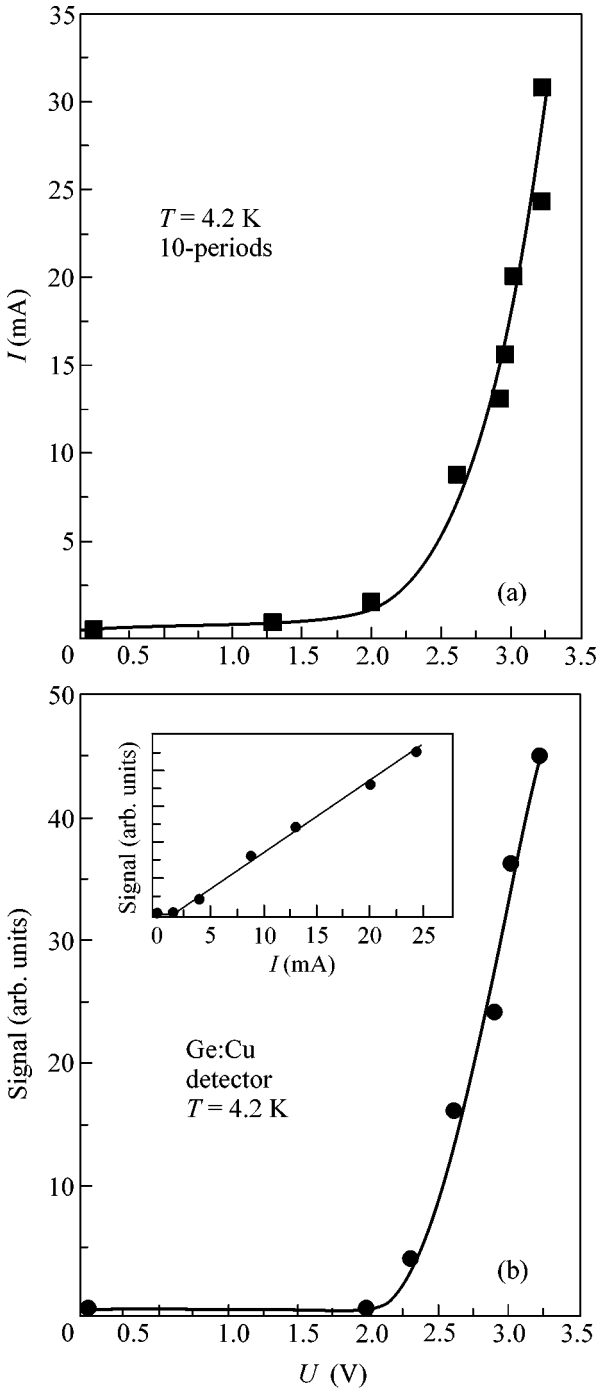

Fig. 3. Dependences of (a) the current and (b) the radiation intensity on the voltage at a temperature of 4.2 K. The inset shows radiation intensity versus current strength.

Thus, in this paper, we reported on the development of devices based on the type-II heterostructures with electrically controlled spacing between the conducting layers. The characteristics of the vertical transport were studied at different temperatures, and far infrared radiation was obtained. The results of the study show that the radiation is caused by electron–hole recombination between adjacent wells. The proposed radiator structure opens up new possibilities for the development of far infrared lasers.

This work was supported by the Russian Foundation for Basic Research (project no. 00-02-17045), the

CRDF (no. RP1-2270), and the program "Physics of Solid Nanostructures." We are grateful to R.A. Suris for useful discussions.

REFERENCES

1. J. Faist, F. Capasso, D. L. Sivco, *et al.*, Science **264**, 553 (1994).
2. R. Colombelli, F. Capasso, C. Gmachl, *et al.*, Appl. Phys. Lett. **78**, 2620 (2001).
3. M. Rochat, J. Faist, M. Beck, *et al.*, Appl. Phys. Lett. **73**, 3724 (1998).
4. J. Ulrich, R. Zobl, V. Schrenk, *et al.*, Appl. Phys. Lett. **77**, 1928 (2000).
5. N. N. Zinov'ev, A. V. Andrianov, V. Yu. Nekrasov, *et al.*, Pis'ma Zh. Éksp. Teor. Fiz. **74**, 105 (2001) [JETP Lett. **74**, 100 (2001)].
6. B. H. Yang, D. Zhang, R. Q. Yang, *et al.*, Appl. Phys. Lett. **72**, 2220 (1998).
7. Yu. B. Vasilyev and S. D. Suchalkin, Electron. Lett. **35**, 1563 (1999).

Translated by E. Golyamina

JETP Letters, Vol. 75, No. 8, 2002, pp. 395–398. Translated from Pis'ma v Zhurnal Éksperimental'noĭ i Teoreticheskoĭ Fiziki, Vol. 75, No. 8, 2002, pp. 467–470.

Polaron Effects on Superexchange Interaction: Isotope Shifts of T_N, T_c, and T^* in Layered Copper Oxides

M. V. Eremin*, I. M. Eremin, I. A. Larionov, and A. V. Terzi

Kazan State University, Kazan, 420008 Tatarstan, Russia

**Mikhail.Eremin@ksu.ru*

Received February 21, 2002; in final form, March 14, 2002

A compact expression has been obtained for the superexchange coupling of magnetic ions via intermediate anions with regard to polaron effects on both magnetic ions and intermediate anions. This expression is used to analyze the main features of the behavior of isotope shifts for temperatures of three types in layered cuprates: the Neel temperatures (T_N), critical temperatures of transitions to a superconducting state (T_c), and characteristic temperatures of the pseudogap state of normal phases (T^*). *© 2002 MAIK "Nauka/Interperiodica".*

PACS numbers: 74.25.-q; 74.72.-h

Elucidating the nature of an unusual isotope effect in copper–oxygen superconductors is one of the most important problems on the way to ascertaining the mechanism of the pairing of charge carriers in these compounds. It is known that it was the observation of an isotope shift of the superconducting transition temperature (T_c) that was of crucial importance in ascertaining the phonon mechanism of pairing in conventional (low-temperature) superconductors. The fact that an isotope effect exists in high-temperature superconductors built of copper–oxygen planes has long been beyond question; however, the relative smallness of the coefficient (for example, $\alpha_{T_c} \sim 0.056$ for $YBa_2Cu_4O_8$ upon replacing ^{16}O with ^{18}O, instead of the standard value 0.5) and the specific features of its behavior in other compounds upon changing the number of holes in copper–oxygen planes do not fit the Bardeen–Cooper–Schrieffer (BCS) scenario. At the same time, the majority of authors of articles related to the isotope effect (see the recent review [1]) correctly point out that, nevertheless, phonon modes, in some mysterious way, affect the superconducting transition temperature. In this context, we believe that the facts of observing an isotope effect for the characteristic temperature of the pseudogap state of underdoped cuprates (so-called pseudogap onset temperature T^*) gain great importance. Thus, according to [2], the isotope exponent upon replacing ^{16}O with ^{18}O corresponding to T^* is $\alpha_{T_c} = 0.061$. It was natural that this fact suggested a common origin of α_{T_c} and α_{T^*} [2].

We believe that another and even more important similarity in the dependence of the order parameters of the superconducting and pseudogap phases on the *d*-type wave vector (that is, $\cos q_x - \cos q_y$) explained had been under the assumption that the transitions to both these phases are associated with short-range potentials [3]. It seems that superexchange interaction, screened Coulomb repulsion, and interaction of holes mediated by optical phonons are the most significant of these. The isotope shift of T_c and T^* due to interaction mediated by optical phonons was discussed in a few works (see, for example, [4, 5]), and that for T^* was considered in [6]. Below, we will focus our attention on polaron corrections to the superexchange coupling of copper spins (J) and demonstrate that a number of features in the behavior of the isotope shift of T_c upon changing the number of holes in the CuO_2 plane can be quite reasonably explained even within the framework of the purely superexchange mechanism of pairing.

First, we emphasize the following important fact. Within the scenario [3], the superconducting transition temperature $T_c \sim 2J - G$, whereas the characteristic temperature of the pseudogap phase $T^* \sim J + G$ [3, 7]. Here, G is the parameter of the screened Coulomb interaction of holes on the nearest copper sites, which partially includes the correction due to interaction mediated by optical phonon modes. If it is granted that the isotope shift is associated with the phonon renormalization of G, the shifts of T_c and T^* would be of opposite sign, which is in contradiction with the experimental results [2]. In this connection, it is believed that the scenario of phonon renormalization of the parameter J is more reasonable to suggest as the source of positive isotope shifts of T_c and T^*.

The renormalization of J within the Hubbard model was investigated in detail by Kugel' and Khomskiĭ [8]. It is evident from the above estimates $T_c \sim 2J - G$ and $T^* \sim J + G$ that the small increase in J proportional to the phonon frequency found in this work gives the correct sign of the isotope shifts but does not provide the required magnitude of the shifts. This can be most sim-

ply demonstrated with the example of the isotope shift of the Neel temperature in related high-T_c compounds. As was already indicated in [1], the Kugel' and Khomskiĭ correction gives the correct sign of the isotope shift of the Neel temperature (T_N) in La_2CuO_4 upon replacing ^{16}O with ^{18}O; however, even the most overrated estimates give a value that is six times lower than the experimental one.

We believe that the main reason for the quantitative disagreement between the theory [8] and the experiment [1] is in the fact that the Hubbard model is not suitable for the compounds we are interested in. As was already stressed in [9], the energies of electron transfer from oxygen to a magnetic ion (Δ_c) in the majority of copper oxides are smaller than the energy of electron transfer from copper to copper (Δ_a). However, the Hubbard model gives correct estimates only when $\Delta_a \geq \Delta_c$.

The Hamiltonian in the form

$$\hat{H} = \sum \varepsilon_a a_\sigma^+ a_\sigma + \sum \varepsilon_c c_\sigma^+ c_\sigma + \sum U_a n_\uparrow^a n_\downarrow^a + \sum U_c n_\uparrow^c n_\downarrow^c + \sum t_{ac}(a_\sigma^+ c_\sigma + c_\sigma^+ a_\sigma) \quad (1)$$

is best suited to the description of superexchange interaction explicitly taking into account the cascade hopping of electrons over oxygen. As applied to high-T_c superconductors, it is rather frequently named the Emery Hamiltonian. Here, t_{ac} is the hopping integral between neighboring copper and oxygen sites, and U_a and U_c are the parameters of electron Coulomb repulsion. We will estimate the corrections to the superexchange parameter J due to polaron effects at copper (a) and oxygen (c) sites in the fashion of [8], supplementing Eq. (1) with the electron–phonon coupling operator

$$\hat{H}_{ep} = \sum_{a,\,b,\,c} g_i n_i (p_q + p_{-q}^+). \quad (2)$$

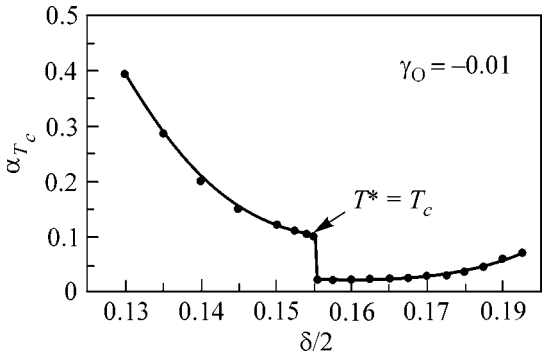

Exponent of the isotope shift of T_c upon replacing ^{16}O with ^{18}O as a function of the number of holes per one copper site. The symbols in the curve correspond to the points at which T_c and T^* were calculated.

Here, p_q and p_{-q}^+ are phonon annihilation and creation operators, and g_i is the coupling parameter connected with the polaron stabilization energy (E_i) at site i by the equation $E_i = g_i^2/\hbar\omega_i$, where ω_i are local vibrational frequencies.

In the physical context, this calculation corresponds to a simplified Holstein model, where the migrating charge locally interacts with breathing modes, forming electron–vibrational states with dispersionless optical phonons. In this connection, it is pertinent to note that conduction in the compounds under consideration is exactly of the polaron type and is accomplished mainly via oxygen ion sites [10].

This calculation is performed most simply by the method of canonical transformations. The matrix of the unitary transformation of the initial Hamiltonian is found by excluding the odd terms with respect to hopping integrals with an accuracy up to sixth-order perturbation theory. The calculation, whose mathematical details will be given in a more detailed article, gives the following result:

$$J = J_0\left\{1 + \frac{3\hbar}{(\Delta_{ca})^2}\left[E_a\omega_a \coth\left(\frac{\hbar\omega_a}{2k_BT}\right) + E_c\omega_c \coth\left(\frac{\hbar\omega_c}{2k_BT}\right)\right]\right\}, \quad (3)$$

where $\Delta_{ac} = \varepsilon_a - \varepsilon_c + U_a - U_c$ means the energy of transfer from oxygen to copper, and the corrections proportional to $E_a\hbar\omega_a/\Delta_{ac}U_a^2$ and $E_a\hbar\omega_a/U_a^3$ are not given because of their smallness for the compounds under consideration. J_0 is the parameter of superexchange interaction of copper spins via the intermediate oxygen atom in the absence of phonons [9, 11]. Note that the appearance of temperature factors in our equation is generally characteristic of the problems on transitions in transition metal compounds with the participation of quasilocal vibrations [12]. At the same time, it should be born in mind that polaron effects break down at $T \sim \omega$ and the concepts used here become inapplicable.

The results of our calculations are given in the figure. The system of integral equations for the mean field parameters corresponding to the transition to the pseudogap phase was solved self-consistently. We identify the pseudogap phase with the phase of sliding charge-density waves. This system was written in detail in [3] and is not given here.

For the description of the superexchange coupling parameter upon replacing some isotopes for other ones at $\hbar\omega \gg k_BT$, it is convenient to introduce parameters γ_{Cu} and γ_O by writing

$$J = J_0\left[1 + \gamma_{Cu}\left(\frac{\Delta M_{Cu}}{M_{Cu}}\right) + \gamma_O\left(\frac{\Delta M_O}{M_O}\right)\right]. \quad (4)$$

It follows from Eq. (3) that, upon replacing ^{16}O with ^{18}O,

$$\gamma_O \approx -\frac{3}{2}\left(\frac{E_a \hbar\omega_a}{\Delta^2_{Cu-O}}\right), \quad (5)$$

whereas, upon replacing ^{63}Cu with ^{65}Cu,

$$\gamma_{Cu} \approx -\frac{3}{2}\left(\frac{E_c \hbar\omega_c}{\Delta^2_{Cu-O}}\right). \quad (6)$$

Substituting here (in electronvolts) $\Delta_{Cu-O} = 1.5$ [13] and standard values $\hbar\omega_a = 0.05$, $E_a = 0.4$ [10, 14], and using the relationship $\Delta T_N/T_N \approx \Delta J/J$ characteristic of layered cuprates (see [1]), we find that the Neel temperature should decrease by 0.2% upon replacing ^{16}O with ^{18}O in $YBa_2Cu_3O_{6.383}$. According to measurements in La_2CuO_4 [15], the shift $\cong$0.6%. If, however, it is assumed, following [1], that $E_a = 1.2$ eV, our estimate will coincide with the experimental value. We hope that this explanation of the isotope shift of T_N will stimulate further experimental investigations of this important problem. Our estimated value $\gamma_O \approx -0.014$ is overrated. The value $\gamma_O \approx -0.01$ is better suited for comparison of the calculated α_{T_c} with experiment; see the figure.

It is relevant to note that, generally speaking, there is another possibility of changing J, which is given by Eq. (4). This possibility is associated with the change in the distance between copper ions upon replacing some isotopes with other ones. It is known that the superexchange parameters very strongly depend on the distance between the interacting ions. This mechanism explains well the increase in T_c under the action of an external pressure on a high-T_c crystal [16, 17]. The question naturally arises in this case as to what occurs with the lattice parameters upon substituting some isotopes for other ones. Recent precision measurements in a $YBa_2Cu_4O_8$ crystal showed [18] that the lattice parameters a, b, and c in the case of ^{16}O equal (Å) 3.8411(1), 3.8717(1), and 27.2372(8), respectively, whereas these are equal to 3.8408(1), 3.8718(1), and 27.2366(8), respectively, for ^{18}O; that is, these parameters are somewhat smaller in the latter case. The positive isotope shift of the nuclear quadrupole resonance frequency of plane copper nuclei [18] is another important experimental fact, which indicates that interatomic copper–oxygen distances are smaller in the case of ^{18}O. Based on these data, one may only conclude that the change of interatomic distances upon replacing some isotopes with other ones must lead to negative shifts of T_c and T^* and will, probably, be relatively small. From the theoretical point of view, this fact seems quite understandable, because changes in interatomic distances upon substituting some isotopes with other ones are due to the lattice anharmonicity, and its effect is naturally of less importance than the effect of harmonic vibrations.

In the figure, the values of the coefficient $\alpha_{T_c} = -d\ln(T_c)/d\ln(M)$ for the replacement of ^{16}O with ^{18}O are plotted as abscissas and the numbers of holes per one copper site are plotted as ordinates. The symbols in the curve correspond to the points at which the system of self-consistent equations from [3] was solved. Because only the order of magnitude is known for the polaron energies E_a and E_c, the parameter γ_O was normalized in such a way that α_{T_c} was equal to 0.1 at the optimal level of doping. The calculated behavior of α_{T_c} is not symmetric with respect to the point of optimal doping. The physical nature of this asymmetry is associated with strong competition between *d*-SC and *id*-CDW phases in the underdoped state. On the left of this point, the isotope shift exponent increases with decreasing number of holes, approaching 0.5, whereas the value of α_{T_c} remains virtually constant, as it also does at $\delta/2$ greater than 0.16 (the so-called overdoped regime). It is this kind of asymmetry (but without a step!) in the behavior of α_{T_c} as a function of the number of holes that was found recently in measurements [19]. The authors of this work mentioned already that, if only conventional interaction via the phonon field were responsible for the isotope effect and the unusual drop of α_{T_c} in the optimal doping region and were related to a peak in the density of states, the curve would have been approximately symmetric with respect to the point of optimal doping. At $\delta/2$ larger than 0.16, the value of α_{T_c} would strongly increase; however, this was not found [19].

As to the isotope shift of T_c upon replacing the copper ^{63}Cu isotope with ^{65}Cu or ^{66}Cu, the fact noted in [20] that the ratio $\alpha_{T_c}(Cu)/\alpha_{T_c}(O) \approx 0.75 \pm 0.1$ does not depend on the type of the compound and on the doping level is naturally explained based on Eq. (3). The stabilization energy of a small-radius polaron (hole) at a copper site is higher than that at an oxygen site. The nearest environment of a hole at an oxygen site comprises positive copper ions, whereas the nearest environment of copper comprises negative oxygen ions. It is this fact that is the reason for the difference between γ_O and γ_{Cu}

The value of α_{T^*} calculated in this work in the region $0.1 < \delta/2 < 0.16$ turned out to be approximately constant: $\alpha_{T^*} \approx 0.01$. This is smaller than the value estimated in experiments (0.061) [2]; therefore, the effect of interaction via optical phonons on α_{T^*} discussed in [6] cannot be excluded. This is also corroborated by a number of experimental points in Fig. 2 from [19] on the right of the point of optimal doping. It is hoped that this problem will be described in a more detailed work.

Thus, the renormalization of the superexchange interaction of copper spins due to polaron effects noted in this work explains the main regularities of the isotope shift of the superconducting transition temperature

in layered cuprates both in the order of magnitude and in the sign and the character of the dependence on the number of holes. The starting equation for the renormalization of the superexchange parameter was verified using the isotope shifts of the Neel temperature of the parent compounds as an example. Our calculations were based on the scenario of competition between the superconducting phase and the charge-density-wave phase. Agreement between the calculations and experiment confirms this scenario. At the same time, our calculation predicts a rather sharp jump of the isotope exponent α_{T_c} on passing through the point of optimal doping. This effect is relatively small; however, we believe that the experimental observation of this effect will be of principal importance.

This work was supported by the Russian Program "Superconductivity," project no. 98014-1, INTAS, project no. YSF 2001/2-45, and the partially supported by was Swiss National Scientific Foundation, project no. 7SUPJ062258.

REFERENCES

1. Guo-meng Zhao, H. Keller, and K. Conder, J. Phys.: Condens. Matter **13**, R569 (2001).
2. F. Raffa, T. Ohno, M. Mali, *et al.*, Phys. Rev. Lett. **81**, 5912 (1998).
3. M. V. Eremin and I. A. Larionov, Pis'ma Zh. Éksp. Teor. Fiz. **68**, 583 (1998) [JETP Lett. **68**, 611 (1998)]; M. V. Eremin, I. A. Larionov, and S. V. Varlamov, Physica B (Amsterdam) **259-261**, 456 (1999).
4. A. Nazarenko and E. Dagotto, Phys. Rev. B **53**, 2987 (1996).
5. A. Bill, V. Z. Kresin, and S. A. Wolf, Z. Phys. **104**, 759 (1997).
6. I. Eremin, M. Eremin, S. Varlamov, *et al.*, Phys. Rev. B **56**, 11305 (1997).
7. S. V. Varlamov, M. V. Eremin, and I. M. Eremin, Pis'ma Zh. Éksp. Teor. Fiz. **66**, 726 (1997) [JETP Lett. **66**, 569 (1997)].
8. K. I. Kugel' and D. I. Khomskiĭ, Zh. Éksp. Teor. Fiz. **3**, 987 (1980) [Sov. Phys. JETP **52**, 501 (1980)].
9. M. V. Eremin, Fiz. Tverd. Tela (Leningrad) **24**, 423 (1982) [Sov. Phys. Solid State **24**, 239 (1982)].
10. X.-X. Bi and P. C. Eklund, Phys. Rev. Lett. **70**, 2625 (1993); K. A. Müller, G.-M. Zhao, K. Conder, and H. Keller, J. Phys.: Condens. Matter **10**, L291 (1998); O. V. Dolgov, H. J. Kaufmann, E. K. H. Salje, and Y. Yagil, Physica C (Amsterdam) **279**, 113 (1997).
11. P. W. Anderson, Phys. Rev. **115**, 2 (1959).
12. S. Sugano, Y. Tanabe, and H. Kamimura, in *Multipletes of Transition-Metal Ions in Crystals* (Academic, New York, 1970).
13. H. Eskes, L. H. Tjeng, and G. A. Sawatzky, Phys. Rev. B **41**, 288 (1990).
14. A. Abragam and B. Bleaney, *Electron Paramagnetic Resonance of Transition Metal Ions* (Clarendon, Oxford, 1970; Mir, Moscow, 1972), Vol. 2.
15. G. M. Zhao, K. K. Singh, and D. E. Morris, Phys. Rev. B **50**, 4112 (1994).
16. L. Jansen and R. Block, Physica A (Amsterdam) **262**, 455 (1999); **247**, 265 (1997).
17. N. M. Plakida, Pis'ma Zh. Éksp. Teor. Fiz. **74**, 38 (2001) [JETP Lett. **74**, 36 (2001)].
18. M. Mali, J. Roos, H. Keller, *et al.*, cond-mat/0112212.
19. D. J. Pringle, G. V. M. Williams, and J. L. Tallon, Phys. Rev. B **62**, 12527 (2000).
20. D. E. Morris, A. P. B. Sinha, V. Kirtikar, *et al.*, Physica C (Amsterdam) **298**, 203 (1998).

Translated by A. Bagatur'yants

JETP Letters, Vol. 75, No. 8, 2002, pp. 399–402. Translated from Pis'ma v Zhurnal Éksperimental'noĭ i Teoreticheskoĭ Fiziki, Vol. 75, No. 8, 2002, pp. 471–475.

Dynamical Nature of Chaos in Electron Systems of High-T_c Superconductors

M. V. Zverev* and V. A. Khodel

Russian Research Center Kurchatov Institute, pl. Kurchatova 1, Moscow, 123182 Russia

** e-mail: zverev@mbslab.kiae.ru*

Received March 14, 2002

A model of the fermion-condensation phase transition forming a plateau in the spectrum of single-particle excitations near the Fermi surface at $T = 0$ is used to analyze those features of the spectral functions of normal states of high-T_c superconductors which are inherent in a marginal Fermi liquid contaminated by impurities. With this model, such a behavior is shown to be due to the fermion condensate, which acts as an impurity subsystem because its energy spectrum at $T = 0$ is dispersionless. The influence of the anisotropy of condensate distribution in the Brillouin zone on the spectral functions is discussed.© *2002 MAIK "Nauka/Interperiodica"*.

PACS numbers: 74.20.Mn; 71.27.+a; 74.72.-h; 05.45.-a

Among numerous anomalies of high-T_c superconductivity, of interest are the unusual properties of the electron spectral function $A(\mathbf{p}, \varepsilon)$ defined as

$$\pi A(\mathbf{p}, \varepsilon) = -\mathrm{Im}G_R(\mathbf{p}, \varepsilon) = \frac{\gamma(\mathbf{p}, \varepsilon)}{(\varepsilon - \epsilon^0_{\mathbf{p}} - \mathrm{Re}\Sigma(\mathbf{p}, \varepsilon))^2 + \gamma^2(\mathbf{p}, \varepsilon)} \quad (1)$$

and extracted from precise angle-resolved photoemission spectroscopy (ARPES) data [1–3]. The following notation is introduced in Eq. (1): G_R is the retarded Green's function; $\gamma = -\mathrm{Im}\Sigma_R$ [the sign of $\gamma(\mathbf{p}, \varepsilon)$ is always positive]; the energy ε is measured from the chemical potential μ; and the bare spectrum $\epsilon^0_{\mathbf{p}}$ is calculated using the standard LDA scheme. These anomalies are most pronounced in the normal phase. In the region (denoted by M) adjacent to the diagonals of the Brillouin zone, the function $\gamma_M(\mathbf{p}, \varepsilon)$ varies linearly with energy, which is typical of the marginal Fermi liquid rather than of the Landau liquid [4]. As the van Hove points $(\pm\pi, 0)$ and $(0, \pm\pi)$ are approached, the electron line broadens and becomes close to Lorentzian.

It should be noted that presently available energy resolution does not exceed 10 meV. For this reason, when analyzing the experimental data, we will be mainly interested in energies $\varepsilon > T$, for which measurement errors are relatively small. The mystery is that, although the experimental dependence of $\gamma_M(\mathbf{n}, \varepsilon)$ ($\mathbf{n} = \mathbf{p}/p$) on ε at these energies is described by a nearly straight line, its extrapolation to zero energy passes not through the origin of coordinates but higher, in contrast to the prediction of the model of a marginal Fermi liquid. This is clearly seen for the $Bi_2Sr_2CaCu_2O_{8+\delta}$ compound [5]. Clearly, such a behavior is quite understandable if the system contains impurities. However, experimentally, the length of the section intercepted on the vertical axis by the above-mentioned straight line depends on n, rendering this explanation inappropriate, because the impurities are usually distributed randomly and scatter electrons elastically and isotropically. A certain anisotropy could appear in $\gamma_M(\mathbf{n}, \varepsilon)$ [6] if the impurities were localized between the planes along which electrons move, but the mechanism of such a selective localization is as yet unknown.

We will show in this letter that these anomalies can be interpreted as the manifestations of customary chaos [6] and, thus, can be caused by reasons that are unrelated to the contamination of a superconductor. As in the preceding work [7], which was also devoted to the spectral functions of high-T_c superconductors, we assume that their electron systems undergo fermion condensation. This phase transition consists of the spontaneous separation of a strongly correlated system into two subsystems. A single-particle spectrum $\epsilon(\mathbf{p})$ of one of them looks like the spectrum of an ordinary Fermi liquid. The other subsystem is a fermion condensate (FC) and represents a set of single-particle states whose energies $\epsilon(\mathbf{p})$ at $T = 0$ coincide with μ [8–12]. The FC distribution is anisotropic even in a square lattice [9, 13], because FC occupies a region C near the van Hove points. When changing the degree of doping and other parameters, the value of the dimensionless parameter η characterizing its "residential area" remains small and does not exceed 10–15%.

At $T = 0$, the zero-approximation condensate Green's function $G^{(0)}_C(\mathbf{p}, \varepsilon)$ is merely $1/\varepsilon$, while the spectral function of FC $A^{(0)}_C(\mathbf{p}, \varepsilon) \sim \delta(\varepsilon)$ has almost the same form as the spectral function of condensate in a Bose liquid (note, parenthetically, that this fact gave the name for the phenomenon of interest). The presence of

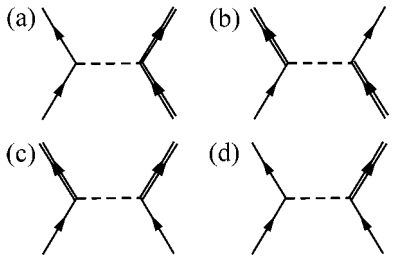

Fig. 1. Scattering diagrams contributing to the imaginary part of mass operator $\gamma_M(\mathbf{p}, \varepsilon)$ in the near-diagonal region M. Single line corresponds to a noncondensate particle, and double line corresponds to a condensate particle.

the δ function in $A_C^{(0)}$ renders the scattering of noncondensate particles from condensate absolutely elastic, as in the case of impurities. However, the number of condensate particles is conserved neither in the Bose nor in the Fermi system; being scattered, they can escape the condensate and return to it. In liquid He-4, the momentum of Bose-condensate particles is zero, and taking such transitions into account, as is known from [14], gives rise to a pole in the mass operator of noncondensate particles, thereby ruling out any correspondence between the impurity system and condensate. A different situation occurs in the Fermi systems: the condensate occupies a certain finite region in the momentum space, so that the possible singularities of Σ become smeared after integration over the condensate momenta. Consequently, if the zero approximation $A_C^{(0)}(\varepsilon) \sim \delta(\varepsilon)$ is valid, the FC distribution anisotropy will be the only fundamental difference between the FC and impurity systems. We will see below that it is this anisotropy which causes the anisotropy of the electron spectral function $A_C^{(0)}(\mathbf{p}, \varepsilon)$. To verify this, let us turn to the equation [15]

$$\mathrm{Im}\Sigma_R(\mathbf{p}, \varepsilon > T) \sim \int_0^{\varepsilon}\int_0^{\omega}\int\int |\Gamma(\mathbf{p}, \varepsilon, \mathbf{p}_1, \varepsilon_1, \mathbf{q}, \omega)|^2 \times \mathrm{Im}G_R(\mathbf{p}-\mathbf{q}, \varepsilon-\omega)\mathrm{Im}G_R(-\mathbf{p}_1, -\varepsilon_1) \times \mathrm{Im}G_R(\mathbf{q}-\mathbf{p}_1, \omega-\varepsilon_1)d\mathbf{p}_1 d\mathbf{q} d\omega d\varepsilon_1 \quad (2)$$

for the imaginary part of the mass operator Σ_R in the normal phase.

Recall that the scattering amplitude Γ in this equation must depend on momenta, otherwise fermion condensation is ruled out. The desired momentum dependence of Γ appears as the system approaches the point of second-order phase transition, which is caused, e.g., by the appearance of charge-density [16] or spin-density [13] waves in the ground state. In this case, the collapse of collective degrees of freedom is preceded by the reconstruction of a single-particle spectrum and the formation of FC.

In what follows, we will focus on the antiferromagnetic scenario of fermion condensation, for which the amplitude Γ calculated in the absence of FC has a sharp maximum at the momentum transfer equal to the antiferromagnetic vector $\mathbf{Q} = (\pi, \pi)$. The corresponding singular part of Γ is given by the formula [17]

$$N_0\Gamma(\mathbf{q} \longrightarrow \mathbf{Q}, \omega) = -\frac{\sigma_1^i\sigma_2^i}{\kappa^2 p_F^{-2}(\mathbf{q}-\mathbf{Q})^2 + \beta^2 + i\omega/\omega_0}. \quad (3)$$

Here, the density of states N_0 is the standard dimensionless multiplier, and the parameter β turns to zero at the point of antiferromagnetic phase transition.

We start our analysis of different contributions to Eq. (2) with the diagram corresponding to the scattering of noncondensate particles by the condensate (Fig. 1a). This diagram is an exact analog of the diagram describing the electron scattering by impurities in dirty superconductors. Substituting the spectral function $A_C^{(0)}(\mathbf{p}, \varepsilon) = \nu_C(\mathbf{p})\delta(\varepsilon)$ into Eq. (2), we find that the contribution γ_M^a from this diagram to γ_M at relatively small ε is given by the formula

$$\gamma_M^a(\mathbf{p}) \sim N_0^{-1}\varepsilon_F^0\int \frac{S_C(\mathbf{p}-\mathbf{p}_1)}{[\kappa^2 p_F^{-2}(\mathbf{p}-\mathbf{p}_1-\mathbf{Q})^2 + \beta^2]^2} \times \frac{\gamma_M(\mathbf{p}_1)}{[\xi_M^2(\mathbf{p}_1) + \gamma_M^2(\mathbf{p}_1)]} d\mathbf{p}_1. \quad (4)$$

The following notation is introduced in Eq. (4): $\xi_M(\mathbf{p}) = \epsilon_M(\mathbf{p}) - \mu = p_F(p - p_F)/M_0^*$, where $M/M_0^* = 1 + (\partial \mathrm{Re}\Sigma/\partial\xi_{\mathbf{p}}^0)_F$ and $S_C(\mathbf{q}) = \sum_{\mathbf{p}} \nu_C(\mathbf{p})\nu_C(\mathbf{p}-\mathbf{q})$, with $\nu_C(\mathbf{p} \notin C) = 0$.

As in the problem with impurities, γ_M^a is independent of ε. However, contrary to that problem, the momentum dependence of the integrand in the case considered is rather complicated, first, because the scattering amplitude Γ as a function of momentum transfer has a singularity and, second, because the momentum distribution in FC is anisotropic. The anisotropy manifests itself in the fact that the function $S_C(\mathbf{q})$ has two almost identical maxima of width $\sim\sqrt{\eta}\,p_F$ and height $\sim\eta p_F$ corresponding to two narrow "windows" for the momentum transfer $\mathbf{q} = (\mathbf{p} - \mathbf{p}_1)$. One of them occurs at small $q \leq \sqrt{\eta}\,p_F$, and the other occurs at small $|\mathbf{q} - \mathbf{Q}| \leq \sqrt{\eta}\,p_F$, so that $S_C(\mathbf{q}) = S_C(\mathbf{q} - \mathbf{Q})$.

When integrating over $\mathbf{p}_1$ in Eq. (4), the singular part of scattering amplitude Γ is of no importance in the first of these regions, so that Γ can be taken to be constant and factored out of the integral, after which integration over the absolute value of momentum p_1 yields

$$\gamma_M^a(\mathbf{p}) \sim \varepsilon_F^0\int S_C(\mathbf{p}-\mathbf{p}_1)d\mathbf{n}_1 \quad (5)$$

(the vector $\mathbf{p}_1$ should lie on the Fermi line). The result of integration is, in fact, isotropic. The corresponding value $\sim\eta^{3/2}$ is smaller than the standard value ($\sim\eta$) precisely because of the anisotropy of FC distribution.

The second window "opens" upon the transition of the condensate particles from one FC "spot" to another. The maximum of function $S_C(\mathbf{q})$ in this case coincides with the maximum of amplitude $\Gamma(\mathbf{q})$. When evaluating this integral, one can use the fact that the Fermi line is close to a circle centered at the edge of the Brillouin zone. Placing the origin of coordinates at this corner, we first integrate over the angles of vector $\mathbf{p}_1$ and then over the absolute value p_1 or, what is the same, over the energy ξ_1. The integral in Eq. (4) can only be taken numerically. Its value dramatically depends on the distance of vector $\mathbf{p}$–$\mathbf{Q}$ from the Fermi line; this eventually causes the anisotropy of $\gamma_M(\mathbf{n})$ (see below).

As for the contributions to γ_M from the processes depicted in Figs. 1b and 1c, the interspot transitions in this case are suppressed, the momentum transfer $\mathbf{q}$ cannot be close to $\mathbf{Q}$, and, consequently, these contributions to γ_M are isotropic and give $\sim\eta^{3/2}$.

The diagram in Fig. 1d corresponds to the creation of one of the condensate particles in the collision of a pair of noncondensate particles. This and the related diagrams are calculated by the formula

$$\gamma_M^d(\mathbf{p}, \varepsilon) \sim \eta N_0^{-1} \int \frac{P_M(\mathbf{p}-\mathbf{q}, \varepsilon)}{[\kappa^2 p_F^{-2}(\mathbf{p}-\mathbf{p}_1-\mathbf{Q})^2 + \beta^2]^2} d\mathbf{q}. \quad (6)$$

The notation $P_M(\mathbf{q}, \varepsilon)$ is introduced here for the imaginary part of a particle–hole propagator in the region M. The contribution to this integral comes from a broad range of momentum transfers $\mathbf{q}$, so that the singular component of amplitude $\Gamma(\mathbf{q})$ again becomes immaterial. Making use of the standard formula $P_M(\mathbf{q}, \varepsilon) \sim \varepsilon$ for P_M, we find that the contribution of the diagram in Fig. 1d to γ_M is proportional to the energy ε and density η and is almost independent of p [18]. This practically completes the list of contributions to γ_M, because the appearance of only FC particles together with one decaying noncondensate particle is kinematically forbidden or, at least, is strongly suppressed. As a result, the following expression is obtained for the imaginary part of the mass operator in the near-diagonal region M:

$$\gamma_M(\mathbf{n}, \varepsilon) = \gamma_0(\mathbf{n}) + s_0\varepsilon. \quad (7)$$

This result differs from that postulated in [4] by the presence of an additional energy-independent term $\gamma_0(\mathbf{n})$, i.e., by the term "governing" the dynamical chaos in the systems with FC.

Let us now consider how this picture changes if one takes into account that the states belonging to FC are damped. When analyzing the damping effects, one should bear in mind that the poles of $G_C(\varepsilon)$ at a finite temperature are shifted to the complex plane. In this case, the real ξ and imaginary γ parts of the pole are proportional to T [10, 18]. If the pole drift was the only change in the Green's function $G_C(\varepsilon)$, then the energy transfer in the scattering of noncondensate particles by FC would be on the order of γ, i.e., on the order of T, and then nothing would change in the above-mentioned picture, because only the case $\varepsilon > T$ is considered in this letter.

However, the condensate line has wings. They appear due to the fact that in the region of sufficiently high energies, $\varepsilon > T$, the condensate spectral function is almost completely determined by the decay of FC particles into three like particles. For the leading term of the expansion in powers of ε, calculation gives [7]

$$A_C(\varepsilon) \sim \beta(\eta\epsilon_F^0|\varepsilon|)^{-1/2}. \quad (8)$$

The influence of the wings of the condensate line on γ_M becomes clear from Eq. (2). At small energies, the addition of $\delta\gamma_M^w$ to γ_M is calculated using the formula differing from Eq. (4) only by one more integration over frequencies and by the multiplier

$$P_C(\omega) = \int_0^\omega A_C(\varepsilon)A_C(\omega-\varepsilon)d\varepsilon. \quad (9)$$

When taken with the opposite sign, this integral is nothing but the imaginary part of a particle–hole propagator. Substituting spectral function (8) into Eq. (9), one obtains

$$P_C(\omega) = \text{const}. \quad (10)$$

The authors of [4] postulated this result to explain the marginal behavior of the electron mass operator Σ.

A more detailed analysis shows that $P_C(\omega)$ in the systems with FC is not a strict constant, although, contrary to the theory of Fermi liquid, it does not vanish at $\omega = 0$. These variations are due to the additional terms that are omitted in Eq. (8), which is valid only at small ε. The first correction to $P_C(\omega)$ behaves like $\sqrt{\omega}$, and the corresponding contribution to γ_M is proportional to $\varepsilon^{3/2}$. Note that the contribution from the diagram with the creation of only one FC particle is also proportional to $\varepsilon^{3/2}$ and, hence, it is of the same order as this additional term.

As in the case with $P_C(\omega)$, the effective electron–electron interaction in the calculation of $\gamma_M(\mathbf{n})$ anisotropy (Fig. 2) was taken in the form of Eq. (3), and the spectrum was $\epsilon_\mathbf{p}^0 = -e_0[\cos(ap_x) + \cos(ap_y) - 2t\cos(ap_x)\cos(ap_y)]$ with the parameter $t = 0.45$ [19]. We also included the energy dependence of $\mathrm{Re}\Sigma$. This function is related to $\mathrm{Im}\Sigma$ by the Kramers–Krönig relation, which was taken in the form [20]

$$\mathrm{Re}\Sigma(\mathbf{p}, \varepsilon) - \mathrm{Re}\Sigma(\mathbf{p}, \varepsilon = 0)$$
$$= \frac{\varepsilon}{\pi} P\left[\int_0^\infty \frac{\mathrm{Im}\Sigma(\mathbf{p}, \varepsilon_1)}{\varepsilon_1(\varepsilon_1-\varepsilon)} d\varepsilon_1 - \int_0^\infty \frac{\mathrm{Im}\Sigma(\mathbf{p}, -\varepsilon_1)}{\varepsilon_1(\varepsilon_1+\varepsilon)} d\varepsilon_1\right]. \quad (11)$$

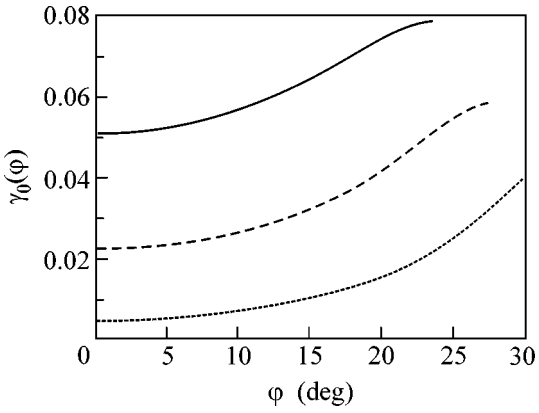

Fig. 2. Plots of the energy-independent term (in units of ε_F^0) in the imaginary part of mass operator $\gamma_0(\varphi)$ against the angle φ of deviation of vector **n** from the diagonal of the Brillouin zone. The values of condensate parameter η are (solid line) 0.13, (dashed line) 0.10, and (dotted line) 0.07. Effective interaction (3) with parameters $\beta = 0.3$ and $\kappa = 1$ was used in the calculations.

The set of Eqs. (2) and (11) was solved iteratively, with a good convergence being achieved in 8–10 steps.

When comparing the computational results with the experimental data, one should bear in mind that the halfwidth of the line (Lorentzian in the momentum space) is the only parameter that is reliably measured by ARPES on the Fermi line. Measurements yield the ratio $\mathrm{Im}\Sigma/v_F$, where $v_F = (\partial\xi_p^0/\partial p)[1 + (\partial\Sigma/\partial\xi)_F]$. The value $v_F^0 = \partial\xi_p^0/\partial p$ can be determined by the LDA calculations. The second multiplier is usually taken to be unity. However, this is not a good approximation because of the observed flattening of the single-particle spectra $\epsilon(\mathbf{p})$ in the vicinity of the van Hove points.

In summary, we have invoked the antiferromagnetic scenario of fermion condensation to demonstrate that the characteristic features of chaos can manifest themselves in the electron systems of high-T_c superconductors, even if they are completely cleansed of impurities. These features are due solely to the separation of the system into two subsystems at the point of fermion condensation, one of the subsystems being a fermion condensate; i.e., the nature of this chaos is purely dynamical. Similar features of dynamical chaos are expected to be observed in the vicinity of other phase transitions, e.g., with the formation of charge-density waves, where these transitions are also preceded by the fermion condensation [16]. Indeed, precise photoemission data obtained recently for the $2HTaSe_2$ compound [21, 22] demonstrate the remarkable similarity in the behavior of $\mathrm{Im}\Sigma$ in this system and in high-T_c superconductors.

We are grateful to L.P. Gor'kov, G.E. Volovik, N.E. Zeĭn, É.E. Sapershteĭn, P.W. Anderson, A. Kaminski, J.W. Clark, G. Kotliar, A.J. Millis, and M.R. Norman for discussions. This work was supported in part by the Russian Foundation for Basic Research (project no. 00-15-96590), the NSF (grant no. PHY-9900713), and the McDonnel Center for Space Science.

REFERENCES

1. Z.-X. Shen and J. R. Schrieffer, Phys. Rev. Lett. **78**, 1771 (1997).
2. M. R. Norman, H. Ding, H. Fretwell, *et al.*, Phys. Rev. B **60**, 7585 (1999).
3. T. Valla, A. V. Fedorov, P. D. Johnson, *et al.*, Science **285**, 2110 (1999).
4. C. M. Varma, P. B. Littlewood, S. Schmitt-Rink, *et al.*, Phys. Rev. Lett. **63**, 1996 (1989).
5. A. Kaminski, M. Randeria, J. C. Campuzano, *et al.*, Phys. Rev. Lett. **86**, 1070 (2001).
6. E. Abrahams and C. M. Varma, cond-mat/0003135.
7. V. A. Khodel and M. V. Zverev, Pis'ma Zh. Éksp. Teor. Fiz. **74**, 565 (2001) [JETP Lett. **74**, 502 (2001)].
8. V. A. Khodel' and V. R. Shaginyan, Pis'ma Zh. Éksp. Teor. Fiz. **51**, 626 (1990) [JETP Lett. **51**, 553 (1990)]; Condens. Matter Theor. **12**, 222 (1997).
9. G. E. Volovik, Pis'ma Zh. Éksp. Teor. Fiz. **53**, 208 (1991) [JETP Lett. **53**, 222 (1991)]; Pis'ma Zh. Éksp. Teor. Fiz. **59**, 798 (1994) [JETP Lett. **59**, 830 (1994)].
10. P. Nozieres, J. Phys. I **2**, 443 (1992).
11. M. R. Norman, in *High Temperature Superconductivity*, Ed. by S. E. Barnes, J. Ashkenazi, J. L. Cohn, and F. Zuo (American Inst. of Physics, Woodbury, 1999), AIP Conf. Proc. **483**, 298 (1999).
12. V. Yu. Irkhin, A. A. Katanin, and M. I. Katsnelson, cond-mat/0110516.
13. M. V. Zverev, V. A. Khodel', and J. W. Clark, Pis'ma Zh. Éksp. Teor. Fiz. **74**, 48 (2001) [JETP Lett. **74**, 46 (2001)].
14. S. T. Belyaev, Zh. Éksp. Teor. Fiz. **34**, 417 (1958).
15. A. A. Abrikosov, L. P. Gor'kov, and I. E. Dzyaloshinskii, *Methods of Quantum Field Theory in Statistical Physics* (Fizmatgiz, Moscow, 1962; Prentice-Hall, Englewood Cliffs, 1963).
16. V. A. Khodel', V. R. Shaginyan, and M. V. Zverev, Pis'ma Zh. Éksp. Teor. Fiz. **65**, 242 (1997) [JETP Lett. **65**, 253 (1997)].
17. A. J. Millis, H. Monien, and D. Pines, Phys. Rev. B **42**, 167 (1990).
18. J. Dukelsky, V. A. Khodel, P. Schuck, and V. R. Shaginyan, Z. Phys. B **102**, 245 (1997).
19. T. Schneider and M. P. Sörensen, Z. Phys. B **80**, 331 (1990); **81**, 3 (1990).
20. A. B. Migdal, *Theory of Finite Fermi Systems and Applications to Atomic Nuclei* (Nauka, Moscow, 1967; Interscience, New York, 1967).
21. R. Liu, C. G. Olson, W. C. Tonjes, and R. F. Frindt, Phys. Rev. Lett. **80**, 5762 (1998).
22. T. Valla, A. V. Fedorov, P. D. Johnson, *et al.*, Phys. Rev. Lett. **85**, 4759 (2000).

Translated by V. Sakun

JETP Letters, Vol. 75, No. 8, 2002, pp. 403–405. Translated from Pis'ma v Zhurnal Éksperimental'noĭ i Teoreticheskoĭ Fiziki, Vol. 75, No. 8, 2002, pp. 476–478.

Precession Spin Relaxation Mechanism Caused by Frequent Electron–Electron Collisions

M. M. Glazov* and E. L. Ivchenko

Ioffe Physicotechnical Institute, Russian Academy of Sciences, Politekhnicheskaya ul. 26, St. Petersburg, 194021 Russia

** e-mail: glazov@coherent.ioffe.rssi.ru*

Received March 18, 2002

It is shown that the D'yakonov–Perel' spin relaxation mechanism in a two-dimensional electron gas is controlled not only by the electron-momentum relaxation that accounts for the electron mobility but also by the electron–electron collisions. The kinetic equation describing the mixing of electron spin in the **k** space was solved, and the spin relaxation time τ_s caused by frequent electron–electron collisions was determined. The time τ_s was calculated for a nondegenerate electron gas both with and without allowance for the exchange interaction. © *2002 MAIK "Nauka/Interperiodica".*

PACS numbers: 72.25.Rb

The precession mechanism of electron-spin relaxation (D'yakonov–Perel' mechanism) is due to the splitting of spin branches in the electron dispersion relation in crystals without an inversion center [1]. The presence of spin splitting is equivalent to the presence of an effective magnetic field, with the Larmor frequency $\Omega_\mathbf{k}$ depending on the magnitude and direction of electron wave vector **k**. The inverse spin relaxation time can be estimated as $\tau_s^{-1} \propto \langle\Omega^2\tau\rangle$, where the angular brackets stand for the averaging over electron energy distribution and τ is the microscopic relaxation time. In a two-dimensional system without an inversion center, e.g., in a semiconducting quantum well, the frequency $\Omega_\mathbf{k}$ is linearly related to the vector **k**. In this case, it is commonly supposed [2–5] that τ is the electron-momentum relaxation time, or the transport time. We call attention to the fact that the contribution to the inverse time τ^{-1} additively comes not only from various momentum-relaxation mechanisms but also from electron–electron collisions that have no effect on the mobility. Indeed, it makes no difference whether a change in the wave vector **k** and, hence, in the axis of Larmor precession $\Omega_\mathbf{k}$, is due to scattering by a static defect, a phonon, or by another electron.

Evidently, the time τ caused by electron–electron collisions depends on the dimensional parameters in the same manner as the *ee*-scattering time determining the rate of energy exchange between electrons [6, 7]; i.e., τ, $\tau_{ee} \sim \tau_{ee}^* \equiv \hbar k_B T\kappa^2/e^4 N$. Here, N is the two-dimensional electron concentration, κ is the dielectric constant, T is absolute temperature, and k_B is the Boltzmann constant (a nondegenerate two-dimensional electron gas is considered). However, the dimensionless coefficients in the expressions for τ and τ_{ee} are different and should be found by solving different kinetic equations. In this work, we calculate the spin relaxation time of a nondegenerate two- dimensional electron gas for the case where this time is controlled by electron–electron collisions.

The electron wave-vector and spin distributions will be described by a spin density matrix, which can conveniently be represented as a linear combination of the 2×2 identity matrix and the spin Pauli matrices; i.e., $\rho(\mathbf{k}) = f_\mathbf{k} + \mathbf{s}_\mathbf{k} \cdot \sigma$. Here, $f_\mathbf{k} = (1/2)\mathrm{Tr}[\rho(\mathbf{k})]$ is the spin-averaged distribution function, $\mathbf{s}_\mathbf{k} = \mathrm{Tr}[\rho(\mathbf{k})(\sigma/2)]$ is the average spin vector for an electron at the point **k**, and the identity matrix is omitted. In the absence of spin splitting, the spin-polarized electron gas with equilibrium energy distribution is described by the density matrix $\rho^0(\mathbf{k}) = f_\mathbf{k}^0(1 + 2\bar{\mathbf{s}} \cdot \sigma)$, where $f_\mathbf{k}^0 = \exp[(\mu - E_\mathbf{k})/k_B T]$ is the Boltzmann distribution function; $E_\mathbf{k} = \hbar^2 k^2/2m$; m is the electron effective mass; μ is the chemical potential; and $\bar{\mathbf{s}}$ is the spin per one electron, i.e., the ratio $\mathbf{S}/N$, where **S** is the total electron spin per unit area. If the spin splitting is small compared to $\hbar/\tau$, the function $\mathrm{Tr}[\rho(\mathbf{k})] = 2f_\mathbf{k}^0$ does not change, whereas the spin vector acquires the nonzero correction $\delta\mathbf{s}_\mathbf{k} = \mathbf{s}_\mathbf{k} - 2f_\mathbf{k}^0\bar{\mathbf{s}}$, which is proportional to the spin splitting. The kinetic equation for this correction has the form

$$2f_\mathbf{k}^0(\Omega_\mathbf{k} \times \bar{\mathbf{s}}) + Q_\mathbf{k}\{\delta\mathbf{s}, f^0\} = 0, \qquad (1)$$

where the first term describes spin precession about the vector $\Omega_\mathbf{k}$, and the second term is the collision integral that mixes spins in the **k** space. In the absence of exchange interaction, the collision integral has the simple form

$$Q_\mathbf{k}\{\delta\mathbf{s}, f^0\} = \sum_{\mathbf{k}'\mathbf{p}\mathbf{p}'} W_{\mathbf{p}\mathbf{p}',\mathbf{k}\mathbf{k}'}(\delta\mathbf{s}_\mathbf{k} f_{k'}^0 - \delta\mathbf{s}_\mathbf{p} f_{p'}^0), \qquad (2)$$

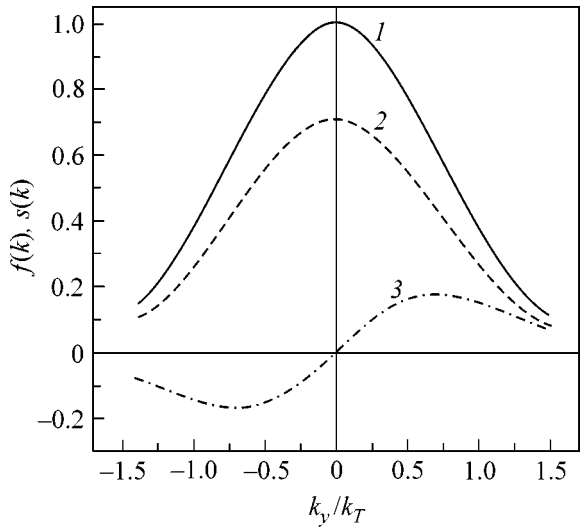

Schematic representation of electron distribution in the **k** space along the k_y axis at fixed k_x and k_z. Curve *1* is the equilibrium distribution function $f^0_{\mathbf{k}}$; curve *2* is the Boltzmann spin distribution function $s_{\mathbf{k},z} \propto \bar{s}_z f^0_{\mathbf{k}}$; and curve *3* is the k_y-odd spin distribution $\delta s_{\mathbf{k},y} \propto \Lambda_{yyz} k_y \bar{s}_z f^0_{\mathbf{k}}$ due to the precession of spin $\bar{s}_z$ about the $\Omega_{\mathbf{k}}$ axes.

where $W_{\mathbf{pp}',\mathbf{kk}'}$ is the probability of electrons **k** and **k**' being scattered, respectively, to the states **p** and **p**'. For the sake of simplicity, the sample area in the interface planes is hereafter taken to be unity. Inasmuch as the spin flip in collisions is ignored, the expression in the parentheses is obtained by substituting the spin corrections $\delta\mathbf{s}_{\mathbf{k}}$ and $\delta\mathbf{s}_{\mathbf{p}}$ for, respectively, $f_{\mathbf{k}}$ and $f_{\mathbf{p}}$ in the difference $f_{\mathbf{k}}f_{\mathbf{k}'} - f_{\mathbf{p}}f_{\mathbf{p}'}$ entering the standard collision integral of nonpolarized electrons and also by substituting corresponding equilibrium distribution functions for $f_{\mathbf{k}'}$ and $f_{\mathbf{p}'}$. Due to the rotation of electron spins about the vectors $\Omega_{\mathbf{k}}$, the averaged spin slowly relaxes following the law $dS_\alpha/dt + \tau^{-1}_{s,\alpha\beta} S_\beta = 0$, where the tensor of inverse spin relaxation times is defined as

$$\tau^{-1}_{s,\alpha\beta} S_\beta = \sum_{\mathbf{k}} \Omega_{\mathbf{k}} \times \delta\mathbf{s}_{\mathbf{k}\alpha}. \tag{3}$$

For definiteness, we will consider the removal of spin degeneracy for an asymmetrical quantum well of the GaAs/AlGaAs type grown in the [001] direction and having the point symmetry C_{2v}. In this case, the vector $\Omega_{\mathbf{k}}$ lies in the interface plane and its dependence on **k** is determined by two linearly independent coefficients [8]: $\hbar\Omega_{\mathbf{k}} = (\beta_- k_y, \beta_+ k_x)$ where the *x* and *y* axes are directed along $[1\bar{1}0]$ and [110]. Then, the projections of the vector $(\Omega_{\mathbf{k}} \times \bar{\mathbf{s}})$ can be represented in the form $\Lambda_{\alpha\beta\gamma} k_\beta \bar{s}_\gamma$, where the third-rank tensor with four nonzero components $\Lambda_{xxz} = -\Lambda_{zxx} = \beta_-/\hbar$ and $\Lambda_{yyz} = -\Lambda_{zyy} = -\beta_+/\hbar$ is introduced. This is illustrated in the figure, where the equilibrium electron distribution function, the Boltzmann distribution function for a nonequilibrium spin in the absence of spin splitting, and the spin-precession correction $\delta s_{\mathbf{k},y}$ are shown.

Let us introduce a linear operator $Q^{-1}_{\mathbf{k}}$ that is inverse of $Q_{\mathbf{k}}\{\delta\mathbf{s}\}$. Since these operators conserve the angular distributions in the **k** space, the function $F(k) \equiv (1/k_\beta) Q^{-1}_{\mathbf{k}} \{k_\beta f^0_k\}$ is independent of the azimuthal angle $\varphi_{\mathbf{k}}$. Then, the solution to Eq. (1) can be written as

$$\delta s_\alpha(\mathbf{k}) = -2\Lambda_{\alpha\beta\gamma}\bar{s}_\gamma Q^{-1}_{\mathbf{k}}\{k_\beta f^0_{\mathbf{k}}\} = -2\Lambda_{\alpha\beta\gamma} k_\beta \bar{s}_\gamma F(k).$$

Inserting it into Eq. (3) and summing over the angle $\varphi_{\mathbf{k}}$, one obtains the following for the principal values of the tensor of inverse spin relaxation times: $\tau^{-1}_{s,xx} = (\beta_+/\hbar)^2 J$, $\tau^{-1}_{s,yy} = (\beta_-/\hbar)^2 J$, and $\tau^{-1}_{s,zz} = \tau^{-1}_{s,xx} + \tau^{-1}_{s,yy}$, where the integral

$$J = \left(\frac{\hbar^2}{2mk_BT}\right)^{1/2} \int_0^\infty F(k) k^2 dk$$

is introduced.

Numerical calculation was performed for the unscreened Coulomb interaction between two-dimensional electrons. The corresponding $\mathbf{k}, \mathbf{k}' \longrightarrow \mathbf{p}, \mathbf{p}'$ scattering probability is given by

$$W_{\mathbf{pp}',\mathbf{kk}'} = (4\pi/\hbar) \times V^2_{\mathbf{k}-\mathbf{p}} \delta_{\mathbf{k}+\mathbf{k}',\mathbf{p}+\mathbf{p}'} \delta(E_k + E_{k'} - E_p - E_{p'}). \tag{4}$$

Here, $V_{\mathbf{q}} = 2\pi e^2/\kappa|\mathbf{q}|$, and the δ function provides the conservation of electron energy and momentum in collisions. This form of the potential allows Eq. (1) to be reduced to the equation for the dimensionless function $u(K) = \tau^{*-1}_{ee} F(k_T K)$, which depends on the dimensionless electron wave vector $\mathbf{K} = \mathbf{k}/k_T$, where $k_T = [2mk_BT/\hbar]^{1/2}$ and $\tau^*_{ee} = \hbar k_B T \kappa^2/e^4 N$. The function $u(K)$ satisfies the equation

$$Ke^{-K^2} = \sum_{\mathbf{K}',\mathbf{P},\mathbf{P}'} \tilde{W}_{\mathbf{PP}',\mathbf{KK}'} (u(K)e^{-K'^2} - \cos\Theta u(P) e^{-P'^2}). \tag{5}$$

Here, Θ is the angle between **K** and **P**, and the probability $\tilde{W}$ is given by Eq. (4), in which $V_{\mathbf{k}-\mathbf{p}}$ is replaced by $|\mathbf{K}-\mathbf{P}|^{-1}$ and all dimensional wave vectors are replaced by dimensionless vectors. In this case,

$$J = k_T^2 \tau^*_{ee} I, \quad I = \int_0^\infty u(K) K^2 dK. \tag{6}$$

The inhomogeneous term in Eq. (5) and the function $u(K)$ were expanded in series using the basis set $l_n(\varepsilon) = \sqrt{2}\exp(-\varepsilon)L_n(2\varepsilon)$, where $L_n(x)$ are the Laguerre polynomials and $\varepsilon = K^2$. In doing so, the identity

$$\sqrt{\varepsilon}e^{-\varepsilon} = \sum_{n=0}^{\infty}\frac{\sqrt{\pi}}{8}\frac{\Gamma(n+1/2)}{n!}l_n(\varepsilon)$$

was used for convenience (see, e.g., [9]). The series expansion of the function $u(K)$ was substituted into the right-hand side of Eq. (5), and summation (integration) over the dimensionless wave vectors was carried out using the Monte Carlo method. In this ways the problem was reduced to a set of linear inhomogeneous equations for the expansion coefficients of the function $u(K)$. The resulting value of I in Eq. (6) was found to be ≈ 0.027. Inclusion of the exchange interaction slightly increased this value to $I \approx 0.028$. This result is obtained if the term

$$Q_{\mathbf{k}}^{exch}\{\delta\mathbf{s}, f^0\} = \sum_{\mathbf{k}'\mathbf{p}\mathbf{p}'} W_{\mathbf{p}\mathbf{p}',\mathbf{k}\mathbf{k}'}^{exch}(2\delta\mathbf{s}_{\mathbf{p}} f_{p'}^0 - \delta\mathbf{s}_{\mathbf{k}} f_{k'}^0 - \delta\mathbf{s}_{\mathbf{k}'} f_k^0) \quad (7)$$

describing the exchange interaction of colliding electrons is added to the collision integral. In Eq. (7), $W_{\mathbf{p}\mathbf{p}',\mathbf{k}\mathbf{k}'}^{exch} = (2\pi/\hbar)\delta_{\mathbf{k}+\mathbf{k}',\mathbf{p}+\mathbf{p}'}\delta(E_k + E_{k'} - E_p - E_{p'})V_{\mathbf{k}-\mathbf{p}}V_{\mathbf{k}-\mathbf{p}'}$. Note that the last term on the right-hand side of Eq. (7) arises because the electron scattering cross section depends on the mutual orientation of electron spins [10]. The procedure for determining the function $u(K)$ and the value of I in the presence of contribution (7) is analogous to the procedure described above.

The time $\tau = \tau_{ee}^* I$ controls the precession mechanism of spin relaxation in the presence of electron–electron collisions:

$$\frac{1}{\tau_{s,xx}} = \left(\frac{\beta_+ k_T}{\hbar}\right)^2\tau, \quad \frac{1}{\tau_{s,yy}} = \left(\frac{\beta_- k_T}{\hbar}\right)^2\tau. \quad (8)$$

It is of interest to compare this value with the momentum relaxation time due to the scattering of two-dimensional electrons by the ionized impurities of the same concentration N: $\tau_p = (2/\pi^2)\tau_{ee}^*$ (see [11]). The ratio of these two times is $\tau_p/\tau = 2/\pi^2 I \approx 7.2$; i.e., the elastic scattering by impurities is less efficient. If the doped layer is separated from the quantum well by a spacer, the influence of elastic scattering by the Coulomb potential of ionized impurities on τ_s can be completely suppressed.

We note in conclusion that the time $\tau = \tau_{ee}^* I$ calculated without the inclusion of exchange interaction can be assigned the meaning of the electron-momentum relaxation time in a two-component plasma composed of holes with a high concentration N and electrons with a small concentration $N_e \ll N$ and with coinciding electron and hole effective masses. In such a system, the time τ is nothing more than the electron-momentum relaxation time caused by the scattering from equilibrium holes: in the electron collisions with holes, the directed electron momentum will flow to the hole subsystem and virtually relax to zero if $N_e \ll N$.

The following steps may continue this study: (a) calculation of time τ in a quantum well with a finite width, where the electron wave function is extended over this width and the interaction energy of two electrons at small distances ρ differs strongly from the $e^2/\kappa\rho$ law; (b) analysis of the spin relaxation of a degenerate electron gas taking into account the Fermi-type state filling and the screening of the Coulomb potential; and (c) passing to a three-dimensional crystal of the GaAs type with cubic (in $\mathbf{k}$) spin splitting of the conduction band.

We are grateful to L.E. Golub and V.I. Perel' for discussions. This work was supported by INTAS (grant no. 99-00015) and by programs of the Russian Ministry of Science and the Presidium of the Russian Academy of Sciences.

REFERENCES

1. M. I. D'yakonov and V. I. Perel', Fiz. Tverd. Tela (Leningrad) **13**, 3581 (1971) [Sov. Phys. Solid State **13**, 3023 (1972)].
2. M. I. D'yakonov and V. Yu. Kachorovskiĭ, Fiz. Tekh. Poluprovodn. (Leningrad) **20**, 178 (1986) [Sov. Phys. Semicond. **20**, 110 (1986)].
3. E. L. Ivchenko, P. S. Kop'ev, V. P. Kochereshko, *et al.*, Pis'ma Zh. Éksp. Teor. Fiz. **47**, 407 (1988) [JETP Lett. **47**, 486 (1988)].
4. Y. Ohno, R. Terauchi, T. Adachi, *et al.*, Phys. Rev. Lett. **83**, 4196 (1999).
5. R. S. Britton, T. Grevatt, A. Malinowski, *et al.*, Appl. Phys. Lett. **73**, 2140 (1998).
6. S. É. Esipov and I. B. Levinson, Pis'ma Zh. Éksp. Teor. Fiz. **42**, 193 (1985) [JETP Lett. **42**, 239 (1985)].
7. S. É. Esipov and I. B. Levinson, Zh. Éksp. Teor. Fiz. **90**, 330 (1986) [Sov. Phys. JETP **63**, 191 (1986)].
8. N. S. Averkiev and L. E. Golub, Phys. Rev. B **60**, 15582 (1999).
9. P. K. Suetin, *Classical Orthogonal Polynomials* (Nauka, Moscow, 1976).
10. L. D. Landau and E. M. Lifshitz, *Course of Theoretical Physics*, Vol. 3: *Quantum Mechanics: Non-Relativistic Theory* (Nauka, Moscow, 1974; Pergamon, New York, 1977), Chap. XVII.
11. S. K. Lyo, Phys. Rev. B **34**, 7129 (1986).

Translated by V. Sakun

JETP Letters, Vol. 75, No. 8, 2002, pp. 406–409. From Pis'ma v Zhurnal Éksperimental'noĭ i Teoreticheskoĭ Fiziki, Vol. 75, No. 8, 2002, pp. 479–482.

Raman Spectra of MgB_2 at High Pressure and Topological Electronic Transition[1]

K. P. Meletov[1]*, M. P. Kulakov[1], N. N. Kolesnikov[1], J. Arvanitidis[2], and G. A. Kourouklis[2]

[1] *Institute of Solid-State Physics, Russian Academy of Sciences, Chernogolovka, Moscow region, 142432 Russia*
** e-mail: mele@issp.ac.ru*

[2] *Physics Division, School of Technology, Aristotle University of Thessaloniki, GR-540 06 Thessaloniki, Greece*

Received March 18, 2002

Raman spectra of MgB_2 ceramic samples were measured as a function of pressure up to 32 GPa at room temperature. The spectrum at normal conditions contains a very broad peak at ~590 cm^{-1} related to the E_{2g} phonon mode. The frequency of this mode exhibits a strong linear dependence in the pressure region from 5 to 18 GPa, whereas, beyond this region, the slope of the pressure-induced frequency shift is reduced by about a factor of two. The pressure dependence of the phonon mode up to ~5 GPa exhibits a change in the slope, as well as a "hysteresis" effect in the frequency vs. pressure behavior. These singularities in the E_{2g} mode behavior under pressure support the suggestion that MgB_2 may undergo a pressure-induced topological electronic transition.

PACS numbers: 74.62.Fj; 74.25.Kc; 74.25.Gz

The discovery of superconductivity in MgB_2 [1] has initiated a number of studies that are related to the pressure behavior of the crystalline structure, phonon spectrum, and superconductivity transition temperature of this material [2–10]. High-pressure experiments, which traditionally are used to test the structural stability of materials, can also play an important role in the understanding of the superconductivity mechanism. The experimentally observed pressure-induced linear decrease in T_c [6–10] is in general agreement with theoretical estimations based on the BCS theory. Theoretical calculations show that MgB_2 can be treated as a phonon-mediated superconductor with very strong electron–phonon coupling of the in-plane optical E_{2g} phonon mode to the partially occupied planar boron σ bands near the Fermi surface [11, 12]. The strong coupling contributes considerably to the anharmonicity of the Raman-active E_{2g} mode which is manifested by its very broad lineshape, ranging from 460 cm^{-1} to 660 cm^{-1}, according to various calculations [11, 13–15]. The other three phonon modes of MgB_2 with symmetries B_{1g}, A_{2u}, and E_{1u} are harmonic and show insignificant electron–phonon coupling [11].

The first report on Raman scattering in MgB_2 revealed a broad asymmetric peak at ~580 cm^{-1} [16], while subsequent investigations attributed the band at the 615–620 cm^{-1} frequency range to the E_{2g} phonon mode [5, 17]. Recently, Kunc *et al.* [18] have reported Raman spectra of MgB_2 consisting of two broad peaks, which differ considerably from the previously reported Raman results [5, 16, 17], and neither of these was attributed to the E_{2g} phonon mode. The original high-pressure Raman experiment up to 15 GPa has shown a large linear pressure shift of the E_{2g} phonon frequency [5]. Further extension of the pressure range up to 44 GPa has revealed a change in the slope of the linear pressure dependence at ~23 GPa for the isotopically pure $Mg_{10}B_2$ samples [6]. Similar singularities are observed in the dependence of T_c on the relative variation of volume, V/V_0 [6], which exhibits a change in the slope of the linear dependence near the values of V/V_0 corresponding to pressures of ~20 GPa and ~15 GPa for isotopically pure $Mg^{10}B_2$ and $Mg^{11}B_2$ samples, respectively. This behavior of the pressure dependence of T_c was also observed at ~9 GPa for MgB_2 samples prepared from a natural boron-isotope mixture [10]. The observed singularities in the pressure dependence of T_c and E_{2g} phonon frequency [6, 10] were related to the Lifshitz isostructural topological electronic transition [19], since the data available at that time on the pressures dependence of the lattice parameters of MgB_2 did not show any structural phase transition at pressure up to 40 GPa [3, 4]. New high-pressure X-ray results showed that MgB_2 undergoes an isostructural phase transition in the pressure range 26–30 GPa [20].

We measured the Raman spectra of MgB_2 as a function of pressure up to 32 GPa at room temperature. The main goal of our experiments was to study carefully the pressure dependence of the E_{2g} phonon mode and to reexamine possible phase transitions in the MgB_2 system. We believe that the results obtained in the present

[1] This article was submitted by the authors in English.

study show new aspects and, in some way, complete the study of the pressure behavior of the E_{2g} phonon mode.

Ceramic samples of MgB_2 were prepared by direct synthesis from constituent elements. The initial materials were amorphous boron powder (natural mixture of isotopes, atomic mass 10.811) and pieces of metallic magnesium, both with a purity greater than 99.9%. The stoichiometric weights of the materials were placed in a molybdenum crucible and heated to 1400°C in a medium-pressure furnace under an Ar-gas pressure of ~12 bar followed by annealing for an hour. During the heating, the synthesis of MgB_2 is assumed to occur at ~900°C. The resulting product was a bronze-colored compact material with a density ~2.23 g/cm^3 and a grain size from 6 to 30 microns. The X-ray powder diffraction pattern of synthesized samples showed the hexagonal MgB_2 (**a** = 3.086 Å and **b** = 3.52 Å) to be the main constituent, with small quantities of MgO and metallic Mg. The transition temperature T_c for the samples used in this study varied between 37.5 and 39 K at normal pressure [10, 21].

Raman spectra were recorded using a triple monochromator (DILOR XY-500) equipped with a CCD liquid-nitrogen cooled detector system. The spectral width of the system was ~8 cm^{-1}, and the 514.5 nm line of an Ar^+ laser with the beam power below 10 mW, measured before the cell, was used for excitation. Small good faceted bronze-colored grains of MgB_2 with a typical size of ~20 μm were selected for Raman measurements. Measurements of the Raman spectra at high pressure were carried out in two independent pressure cycles using a diamond anvil cell (DAC) of the Mao-Bell type [22]. A 4 : 1 methanol–ethanol mixture was used as the pressure-transmitting medium, and the ruby fluorescence technique was used for pressure calibration [23]. The E_{2g} phonon frequency was obtained with an accuracy of about ~10 cm^{-1} by fitting a Gaussian function to the experimental peak after background subtraction. This background was taken as growing linearly, and the reference points used for the subtraction were the minimum (maximum) intensity of the spectrum at its low (high) frequency limits, respectively.

The Raman spectra of the ceramic samples of MgB_2, taken at normal conditions consist of a broad peak centered near ~590 cm^{-1}. This frequency value is lower than the earlier reported frequency of the E_{2g} mode [5, 17]. Probing the ceramic MgB_2 samples with the use of high spatial resolution of the micro-Raman system provided us with the possibility of identifying small crystalline grains of MgB_2, whose Raman spectra represents a typical E_{2g}-mode peak which differs drastically from that of possible inclusions.

The Raman spectra of MgB_2 for various pressures up to ~29 GPa at room temperature are shown in Fig. 1. The initial spectrum at 1.1 GPa (Fig. 1a) contains a broad (FWHM ~ 250 cm^{-1}) peak near ~600 cm^{-1}, which

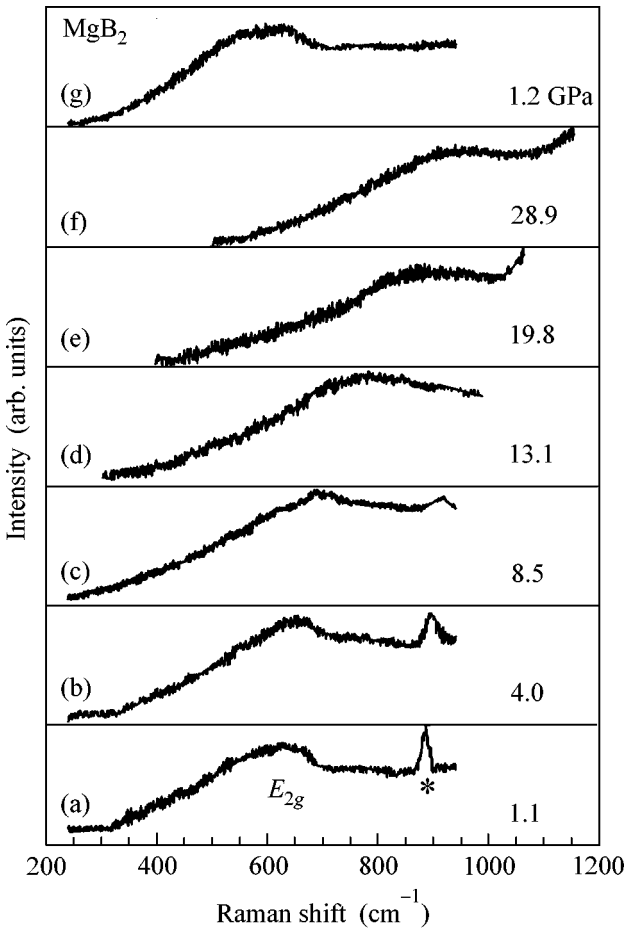

Fig. 1. Raman spectra of MgB_2 for various pressures up to ~29 GPa at room temperature. Asterisk indicates a methanol–ethanol mixture peak.

is assigned to the Raman-active E_{2g} mode. The relatively sharp peak near ~880 cm^{-1} is associated with a methanol–ethanol mixture peak. The intensity of this peak gradually drops with an increase in pressure and vanishes at ~12 GPa upon mixture solidification. When pressure increases, the E_{2g} peak shifts to higher energy (Figs. 1b–1f) and somehow broadens, while its Raman intensity does not change noticeably. The release of pressure down to 1.2 GPa (Fig. 1g) restores the main features of the initial Raman spectrum.

The pressure dependence of the E_{2g}-mode frequency, worked out for various pressure runs, is shown in Fig. 2. The open circles show the data for increasing pressure to ~20 GPa, while the closed circles are related to the decrease of pressure to ~1.2 GPa.

The data marked by open squares are recorded at the subsequent upstroke pressure cycle from ~1.2 GPa to ~32 GPa performed immediately after the release of pressure without disassembling the DAC. The shaded areas near ~5 GPa and ~18 GPa separate the regions where the pressure behavior of the E_{2g}-phonon frequency can be fitted to a linear dependence with

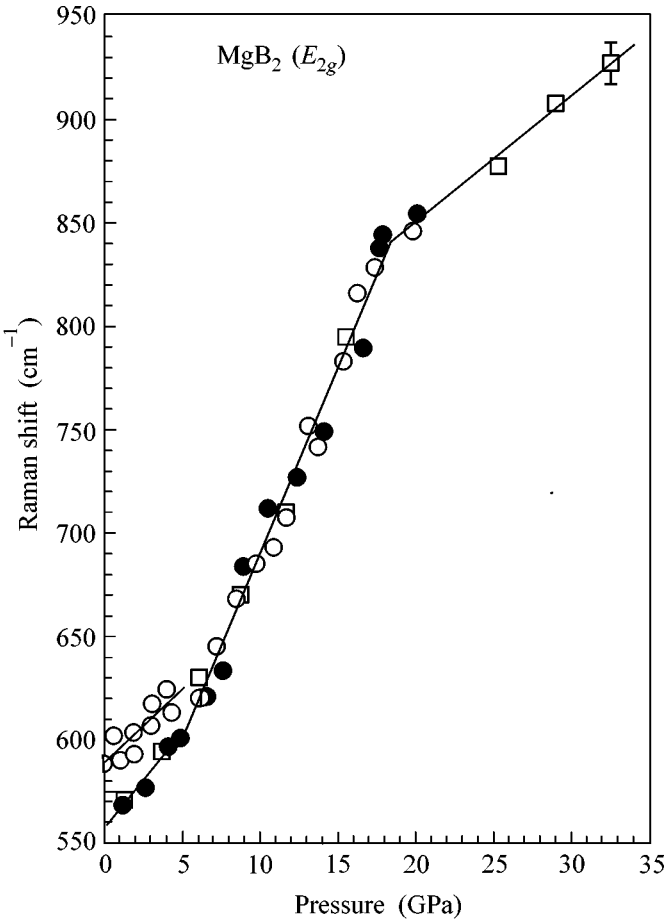

Fig. 2. Pressure dependence of the frequency of the E_{2g} phonon in MgB_2. The open (closed) symbols are related to an increase (decrease) in pressure. The shaded areas show the pressure regions where the changes in the slopes of linear pressure shift were observed.

different slopes $\partial\omega/\partial P$. The largest slope $\partial\omega/\partial P$ = 18 cm^{-1}/GPa, is found for the region $5 \le P \le 18$ GPa, while for $P > 18$ GPa the slope $\partial\omega/\partial P$ is 6 cm^{-1}/GPa. The most intriguing behavior is observed in the pressure region 1 bar–5 GPa, where the route (open cycles in Fig. 2) of the two upstroke pressure cycles (new cell loading) differs from the route of the downstroke (solid cycles in Fig. 2) and upstroke (open squares) cycles without the total release of pressure in the DAC. The slopes $\partial\omega/\partial P$ of both routes are slightly different, ~7 cm^{-1}/GPa for the new loading and ~9 cm^{-1}/GPa for the recycling routes. Note that the spread of experimental data at the E_{2g}-mode frequency is consistent with the accuracy in the peak position determination, which was found to be close to ~10 cm^{-1}.

The pressure dependence of the E_{2g}-mode frequency demonstrates two singularities near ~5 GPa and ~18 GPa. These results are partly correlated with the Raman data obtained by Struzhkin *et al.*, who reported a singularity in the slope of the phonon pressure dependence near ~23 GPa for the isotopic pure $Mg^{10}B_2$ sample and near ~15 GPa in the pressure dependence of T_c for the isotopically pure $Mg^{11}B_2$ sample [6]. Taking into account that the samples in the present investigation were prepared from a natural mixture of boron isotopes, we believe that the singularity near ~18 GPa has the same origin as those observed in [6] for isotopically pure samples. As for the singularity at ~5 GPa, it seems to be a new result revealed by recording the spectra with small steps of pressure increase in this interval.

The experimental data for the pressure dependence of the E_{2g}-phonon mode are seemingly in contradiction with the X-ray data on MgB_2. Although the Raman data show distinct singularities in their pressure dependence, the pressure dependences of the *a* and *c* parameters of the hexagonal lattice are smooth and do not show any structural phase transition in the pressure region up to 12 GPa [2, 3, 5–6]. Furthermore, the X-ray results of Bordet *et al.* [4], extended to higher pressure, indicated the absence of any structural phase transitions up to ~40 GPa. However, Sun Li-Ling *et al.* [20] observed an isostructural phase transition in the pressure region 26–30 GPa accompanied by a substantial change in the unit-cell volume, while their Raman results also showed some anomalies in the E_{2g}-mode pressure behavior, the most significant of them being the appearance of a band splitting at ~30 GPa. A possible explanation for these discrepancies in the pressure behavior of MgB_2 may be related to the Lifshitz topological electronic transition [19] associated with the pressure-induced changes in the topology of a Fermi surface. In such a transition, the electron density of states at the Fermi level, as well as the electron dynamics, possess some specific features which lead to anomalies of the electron thermodynamic and kinetic characteristics. The band structure calculations for MgB_2 [11, 12] show splitting of the planar boron σ bands along the Γ–A line near the Fermi surface, which creates the conditions for the Lifshitz-type transition under high pressure. Tissen *et al.* [10] have suggested that MgB_2 undergoes the Lifshitz topological electronic transition, and this explains the cusp in the pressure dependence of T_c near 9 GPa. The same suggestion has been used to explain the changes in the slopes of the linear pressure dependences of the E_{2g}-phonon frequency and superconducting transition temperature T_c for isotopically pure $Mg^{11}B_2$ and $Mg^{10}B_2$ samples [6]. We believe that the manifestation of the electronic topological transition in the pressure dependence of the E_{2g}-phonon mode may be related to the strong electron–phonon coupling of this mode to the planar boron σ bands.

Concerning the singularity in the E_{2g}-phonon pressure dependence near ~5 GPa, we believe that this may be related to some transformation of the initial ceramic material associated with a trend towards phase homogenization under high pressure. It seems that the recovered material is more homogeneous, because its pres-

sure response and the E_{2g}-phonon frequency is lower than that of the starting material; therefore, the investigation of T_c for a high-pressure-treated ceramic sample might be interesting. In any case, we think that, in order to clarify this suggestion, further experiments with high-quality crystalline samples are necessary.

Finally, we would like to address the difference in the E_{2g}-phonon frequency reported in various Raman studies at normal conditions [5, 6, 16–18]. We think that its origin may be related to the difference in the stoichiometry of ceramic samples. For example, recent publication [21] indicates that the ceramic samples, in fact, have various stoichiometries, $Mg_{1-x}B_2$ with $0 \le x \le 0.2$, and the superconducting transition temperature T_c varies accordingly from 37 to 39 K.

In conclusion, the pressure dependence of the E_{2g} phonon-mode frequency measured as a function of pressure up to 32 GPa shows two singularities near ~5 and ~18 GPa. The singularity at ~5 GPa may be related to the pressure-induced homogenization of ceramic samples, while the singularity at ~18 GPa may be related to a Lifshitz topological electronic transition [19].

This work was supported by the General Secretariat for Research and Technology, Greece.

REFERENCES

1. J. Nagamatsu, N. Nakagava, T. Muranaka, *et al.*, Nature **410**, 63 (2001).
2. T. Vogt, G. Schneider, J. A. Hriljac, *et al.*, Phys. Rev. B **63**, 220505 (2001).
3. K. Prassides, Y. Iwasa, T. Ito, *et al.*, Phys. Rev. B **64**, 012509 (2001).
4. P. Bordet, M. Mezour, M. Nunez-Regueiro, *et al.*, Phys. Rev. B **64**, 172502 (2001).
5. A. F. Goncharov, V. V. Struzhkin, E. Gregoryanz, *et al.*, Phys. Rev. B **64**, 100509 (2001).
6. V. V. Struzhkin, A. F. Goncharov, R. J. Hemley, *et al.*, cond-mat/0106576 (2001).
7. B. Lorenz, R. L. Meng, and G. W. Chu, Phys. Rev. B **64**, 012507 (2001).
8. S. Deemyad, J. S. Shcilling, J. D. Jorgensen, *et al.*, cond-mat/0106057 (2001).
9. T. Tomita, J. J. Hamlin, J. S. Shcilling, *et al.*, Phys. Rev. B **64**, 092505 (2001).
10. V. G. Tissen, M. V. Nefedova, N. N. Kolesnikov, *et al.*, cond-mat/0105475 (2001).
11. T. Yildirim, O. Gülseren, J. W. Lynn, *et al.*, Phys. Rev. Lett. **87**, 037001 (2001).
12. T. Loa and K. Syassen, Solid State Commun. **118**, 279 (2001).
13. J. Kortus, I. I. Mazin, K. D. Belashchenko, *et al.*, Phys. Rev. Lett. **86**, 4656 (2001).
14. J. M. An and W. E. Pickett, Phys. Rev. Lett. **86**, 4366 (2001).
15. X. Kong, O. V. Dolgov, O. Jepsen, *et al.*, Phys. Rev. B **64**, 020501 (2001).
16. K.-P. Bohen, R. Heid, and B. Renker, Phys. Rev. Lett. **86**, 5771 (2001).
17. J. Hlinka, I. Gregora, J. Pokorny, *et al.*, Phys. Rev. B **64**, 140503 (2001).
18. K. Kunc, I. Loa, K. Syassen, *et al.*, J. Phys.: Condens. Matter **13**, 9945 (2001).
19. I. M. Lifshitz, Zh. Éksp. Teor. Fiz. **38**, 1569 (1960) [Sov. Phys. JETP **11**, 1130 (1960)].
20. S. L.-Ling, T. Kikegava, W. Qi, *et al.*, Chin. Phys. Lett. **18**, 1401 (2001).
21. M. V. Indenbom, L. S. Uspenskaya, M. P. Kulakov, *et al.*, Pis'ma Zh. Éksp. Teor. Fiz. **74**, 304 (2001) [JETP Lett. **74**, 274 (2001)].
22. A. Jayaraman, Rev. Sci. Instrum. **57**, 1013 (1986).
23. D. Barnett, S. Block, and G. J. Piermarini, Rev. Sci. Instrum. **44**, 1 (1973).

JETP Letters, Vol. 75, No. 8, 2002, pp. 410–414. From Pis'ma v Zhurnal Éksperimental'noĭ i Teoreticheskoĭ Fiziki, Vol. 75, No. 8, 2002, pp. 483–487.

Fluctuations and Landau–Devonshire Expansion for Barium Titanate[1]

A. I. Sokolov[1]* and A. K. Tagantsev[2]

[1] *St. Petersburg Electrotechnical University, St. Petersburg, 197376 Russia*

**e-mail: ais2002@mail.ru*

[2] *Ecole Polytechnique Fédérale de Lausanne, CH-1015 Lausanne, Switzerland*

Received February 21, 2002; in final form March 18, 2002

The experimentally observed temperature dependence of the quartic coefficients in the Landau–Devonshire expansion for $BaTiO_3$ is naturally accounted for within a proper fluctuation model. It is explained, in particular, why one of the quartic coefficients varies with temperature above T_c, while the second is constant. It is argued that the tetragonal phase in $BaTiO_3$ exists essentially due to thermal fluctuations, while the true Landau–Devonshire expansion with temperature-independent coefficients favors the rhombohedral ferroelectric phase. © *2002 MAIK "Nauka/Interperiodica".*

PACS numbers: 77.80.Bh; 77.84.Dy

The phase diagram of barium titanate contains three lines of phase transitions, and its structure is known to be properly reproduced by the phenomenological Landau–Devonshire theory [1]. It is accepted within the phenomenological approach that all the coefficients in the Landau free-energy expansion should be either constants or weak functions of temperature, pressure, etc., except for the quadratic term, which changes its sign when scrossing the second-order transition line or the low-temperature spinodal. For barium titanate, however, the matching with the theory of the experimentally observed temperature dependences of the nonlinear dielectric susceptibility and spontaneous polarization forces one to allow for the strong temperature dependence of some higher-order coefficients [2–4]. Being in conflict with the spirit of the Landau theory itself, the rapid temperature variation of the quartic and sextic coefficients is also quite unexpected from the microscopic point of view. Indeed, barium titanate is a displacive ferroelectric with weak anharmonicity, which can only result in the rather slow temperature dependence of the macroscopic parameters [5]. Moreover, there is one additional point showing how unsatisfactory the real situation is: because of the fast temperature variation of a certain coefficient, the sixth-order Landau–Devonshire expansion for $BaTiO_3$ with upgraded coefficients [6, 7] loses its global stability at T = 443 K, i.e., at the temperature that exceeds the cubic–tetragonal transition point T_c by only 50 K.

In this letter, we will show that the temperature dependence of the quartic Landau–Devonshire coefficients, experimentally observed in a paraelectric phase of $BaTiO_3$, can be attributed to the thermal fluctuations of polarization and naturally accounted for within the proper fluctuation model. It will be explained, in particular, why in experiments one of the quartic coefficients demonstrates a well-pronounced variation with temperature, while the second is temperature-independent. A conjecture will be put forward concerning the structure of the true Landau–Devonshire form for $BaTiO_3$ using constant (temperature-independent) coefficients, and the first-order fluctuation corrections to the sextic Landau–Devonshire coefficients for $T > T_c$ will be found.

Barium titanate is a displacive ferroelectric which undergoes first-order ferroelectric phase transitions, with the sixth-order anharmonicity and electrostriction playing an essential role in forming its phase diagram. The electrostriction is known to convert the second-order transition, appropriate to the clamped crystal, into the first-order one. Strong dipole–dipole interactions affect the vibrational spectrum of $BaTiO_3$, resulting in a large gap between transverse (soft) and longitudinal polarization modes. These main features are properly described by an effective Hamiltonian that is the natural generalization of the Landau–Devonshire free-energy expansion:

$$\begin{aligned} H = \frac{1}{2}\sum_q \left[\left(\frac{T-T_0}{C\epsilon_0} + s^2q^2\right)\delta_{\alpha\beta} + \Delta^2 n_\alpha n_\beta\right]\phi_{\alpha q}\phi^*_{\beta q} \\ + \int d^3x \left[\frac{c_{11}}{2}(u_{11}^2 + u_{22}^2 + u_{33}^2)\right. \\ + c_{12}(u_{22}u_{33} + u_{33}u_{11} + u_{11}u_{22}) \\ \left. + \frac{c_{44}}{2}(u_{12}^2 + u_{23}^2 + u_{31}^2)\right] + H_{\text{int}} + H_{\text{str}}, \end{aligned} \quad (1)$$

[1] This article was submitted by the authors in English.

$$H_{\text{int}} = \int d^3x[\beta_1(\phi_1^4 + \phi_2^4 + \phi_3^4) + 2\beta_2(\phi_1^2\phi_2^2 + \phi_2^2\phi_3^2 + \phi_3^2\phi_1^2) + \gamma_1(\phi_1^6 + \phi_2^6 + \phi_3^6) + 3\gamma_2(\phi_1^4\gamma_2^2 + \phi_1^2\phi_2^4 + \phi_2^4\phi_3^2 + \phi_2^2\phi_3^4 + \phi_3^4\phi_1^2 + \phi_3^2\phi_1^4) + 6\gamma_3\phi_1^2\phi_2^2\phi_3^2], \quad (2)$$

$$H_{\text{str}} = \int d^3x\{q_{11}(u_{11}\phi_1^2 + u_{22}\phi_2^2 + u_{33}\phi_3^2) + q_{12}[u_{11}(\phi_2^2 + \phi_3^2) + u_{22}(\phi_3^2 + \phi_1^2) + u_{33}(\phi_1^2 + \phi_2^2)] + q_{44}(u_{23}\phi_2\phi_3 + u_{31}\phi_1\phi_3 + u_{12}\phi_2\phi_1)\}. \quad (3)$$

Here, ϕ_α and $u_{\alpha\beta}$ are the Cartesian components of the fluctuating polarization and strain, $\phi_{\alpha q}$ stands for the Fourier transform of $\phi_\alpha(x)$, $n_\alpha = q_\alpha/q$, C is the Curie constant, $\Delta^2 \sim \epsilon_0^{-1} \sim sa^{-1}$ is the dipole gap in the fluctuation spectrum, and a is a lattice constant. Contrary to the original free-energy expansion, Hamiltonian (1)–(3) accounts for the inhomogeneous fluctuations of the polarization and elastic strains, making it possible to explore the fluctuation effects in $BaTiO_3$.

Dealing with the first-order phase transition, we are in a position to study the fluctuation effects in the region where thermal fluctuations of the order parameter are weak. Hence, in what follows, we limit ourselves to the calculation of the first-order fluctuation corrections to the quantities of interest. The quantities to be found are the full four-leg and six-leg vertices that are reduced, under zero external momenta, to the effective ("dressed") quartic B_i and sextic Γ_i coefficients which enter the Landau–Devonshire expansion. Among five Feynman diagrams representing the lowest-order nontrivial terms in the perturbative expansions of the vertices mentioned, only two one-loop graphs give contributions that rapidly, as $(T - T_0)^{-1/2}$, grow as they approach the transition point. These graphs have an obvious structure and may be calculated in the standard way using the propagator

$$G_{\alpha\beta}(q) = \frac{k_B T(\delta_{\alpha\beta} - n_\alpha n_\beta)}{(C\epsilon_0)^{-1}(T - T_0) + s^2q^2}, \quad (4)$$

with the longitudinal part being fully neglected. The results for the quartic couplings B_1 and B_2 are found to be

$$B_1 = \beta_1 - \frac{k_B T\sqrt{C\epsilon_0}}{10\pi s^3\sqrt{T - T_0}}(24\beta_1^2 + 4\beta_1\beta_2 + 6\beta_2^2),$$
$$B_2 = \beta_2 - \frac{k_B T\sqrt{C\epsilon_0}}{10\pi s^3\sqrt{T - T_0}}(3\beta_1^2 + 18\beta_1\beta_2 + 13\beta_2^2). \quad (5)$$

The polynomials in brackets coincide with those of the one-loop contributions to the renormalization-group β functions of the cubic ferroelectric [8, 9]. This is not surprising since, in fact, the same integrals and tensor convolutions are evaluated in both cases. The fluctuation correction to B_1 given by the first Eq. (5) is consistent with the results of Vaks [5, 10], who was the first to evaluate this correction and show that it is essential for the case of $BaTiO_3$.

To proceed, we have to estimate the "bare" coupling constants β_1 and β_2 for $BaTiO_3$ trusting the experimental data available. Aiming to extract the necessary information from experiments, one should realize that (i) what is measured are not bare but dressed couplings with the fluctuation contributions included, and (ii), in experiments, the Landau–Devonshire coefficients are measured for stress-free (not clamped) crystals. Hence, in order to estimate β_1 and β_2, we have to first express them via their analogs for a free crystal, β_1^f and β_2^f. This problem is solved by evaluation of the elastic strains caused by the nonzero uniform polarization and consequent renormalization of coefficients in the relevant Landau–Devonshire expansion [1]. All the elastic and electrostrictive moduli are known for $BaTiO_3$ [7], making corresponding calculations straightforward. The final result is as follows:

$$\beta_1 = \beta_1^f + 7.4 \times 10^8 Vm^5C^{-3},$$
$$\beta_2 = \beta_2^f - 2.3 \times 10^8 Vm^5C^{-3}. \quad (6)$$

Since, in the vicinity of T_c, the elastic and electrostrictive moduli weakly depend on temperature, similar relations should be valid for the fluctuation-modified (dressed) quartic coefficients B_1, B_2, B_1^f, and B_2^f.

At the transition point (T_c = 393 K), $B_1^f = -2.0 \times 10^8 Vm^5C^{-3}$, $B_2^f = 1.6 \times 10^8 Vm^5C^{-3}$ [6, 7] and, hence, $B_1 = 5.4 \times 10^8 Vm^5C^{-3}$, $B_2 = -0.7 \times 10^8 Vm^5C^{-3}$. It is easy to see that for $B_1 > B_2$ the rhombohedral phase has a lower free energy than the tetragonal one, provided the sixth-order form is isotropic, i.e., does not influence their competition. Hence, in the clamped crystal, the quartic form of the Landau–Devonshire expansion strongly favors the phase transition into the rhombohedral phase. The same is true for higher temperatures T = 415 K and T = 423 K, where $B_1^f = -1.3 \times 10^8 Vm^5C^{-3}$ [2], $B_1 = 6.1 \times 10^8 Vm^5C^{-3}$ and $B_1^f = -1.0 \times 10^8 Vm^5C^{-3}$ [2], $B_1 = 6.4 \times 10^8 Vm^5C^{-3}$, respectively, with B_2^f and B_2 remaining unchanged.

Now, we intend to estimate to what extent the fluctuations can modify the behavior of barium titanate in the vicinity of T_c. As seen from Eqs. (5), the quartic Landau–Devonshire coefficients should vary with tem-

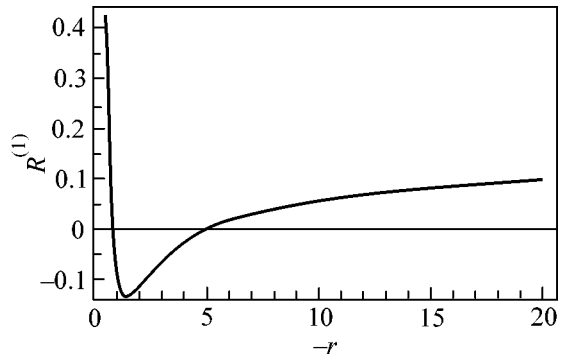

The ratio of the first-order fluctuation corrections $R^{(1)} = B_2^{(1)}/B_1^{(1)}$ as a function of the ratio of bare coupling constants $r = \beta_1/\beta_2$.

perature in a similar way, provided the fluctuation corrections to them are of the same order of magnitude. Let us compare the magnitudes of the fluctuation terms $B_2^{(1)}$ and $B_1^{(1)}$ within the domain where parameters β_1 and β_2 have relevant values and signs. The quantity characterizing the relative weights of $B_2^{(1)}$ and $B_1^{(1)}$ is their ratio, which can be found directly from Eqs. (5). The plot of the ratio $R^{(1)} = B_2^{(1)}/B_1^{(1)}$ as a function of $r = \beta_1/\beta_2$ is shown in the figure. Analyzing this function, one can find, in particular, that $\left|B_2^{(1)}/B_1^{(1)}\right|$ does not exceed 0.1 if $\dfrac{\beta_1}{\beta_2}$ lies between –28 and –2.3.

Let us further estimate β_1/β_2 in $BaTiO_3$. Since, according to experiments, B_1 varies appreciably with the temperature, the estimate for β_1 is expected to have a somewhat limited accuracy. To keep the perturbation theory more or less meaningful, one should accept that the fluctuation term $B_1^{(1)}$ is, at least, two times smaller than the value of B_1 at $T = T_c$. At the transition temperature, $B_1 = 5.4 \times 10^8 Vm^5C^{-3}$ and this coefficient was shown to increase when the temperature increases. Hence, the limitation $\beta_1 \le 10^9 Vm^5C^{-3}$ looks quite reasonable. Another quartic coefficient, B_2, does not depend on T, and the estimate $\beta_2 = B_2 = -0.7 \times 10^8 Vm^5C^{-3}$ may be considered as an accurate one. Since, in any case, $\beta_1 > B_1(T = 393\ \text{K}) = 5.4 \times 10^8 Vm^5C^{-3}$, we see that $-14 < \beta_1/\beta_2 < -8$ in barium titanate. This implies that, according to the figure, $B_2^{(1)} < 0.08 B_1^{(1)}$ and the fluctuation correction $B_2^{(1)}$ is inevitably very small. This means that B_2 is virtually independent of T and explains why in $BaTiO_3$ the Landau–Devonshire coefficient B_2^f is insensitive to temperature.

Apart from the smallness of $B_2^{(1)}$, the theory naturally accounts for the experimentally observed sign of the fluctuation contribution to B_1. Indeed, as seen from Eqs. (5), the sign of $B_2^{(1)}$ is completely controlled by the first term proportional to β_1^2: the large number of 24 provides the positiveness of the polynomial in brackets, avoiding any possibility for the rest of the terms to compete with the first one for any values of β_1 and β_2. Hence, the theory definitely predicts that the fluctuation correction $B_2^{(1)}$ is negative and, therefore, when approaching T_c from above, B_1 and B_1^f should vary downward. This conclusion is in agreement with experiments [2, 3].

As we have already seen, the experimental data available do not allow one to fix the true temperature-independent value of the Landau–Devonshire coefficient β_1. However, there are obvious requirements that enable us to improve the crude estimate for β_1 presented above. The theory developed on the basis of the first-order perturbative calculations is believed to account for the main features of the behavior of $BaTiO_3$. Hence, it should explain the variation of $B_1^f(T)$ by, at least, $10^8 Vm^5C^{-3}$ [2] and remain valid, at worst, at the semiquantitative level. It is possible to meet both requirements by only accepting that the true value of β_1 is appreciably larger than $6.4 \times 10^8 Vm^5C^{-3}$ and appreciably smaller than $1.1 \times 10^9 Vm^5C^{-3}$; i.e., it lies somewhere between $7 \times 10^8 Vm^5C^{-}$ and $10^9 Vm^5C^{-3}$. As a result, the stress-free crystal should possess the Landau–Devonshire coefficient that obeys the inequalities $-0.4 \times 10^8 Vm^5C^{-3} < \beta_1^f < 2.6 \times 10^8 Vm^5C^{-3}$.

The upper part of this interval is of particular interest. The point is that whenever β_1^f exceeds $1.6 \times 10^8 Vm^5C^{-3} = \beta_2^f$ the crystal whose fluctuations are "switched off" should undergo a phase transition to the rhombohedral phase rather than to the tetragonal one. If this were true, i.e., the inequality $\beta_1^f > \beta_2^f$ took place, the tetragonal and orthorhombic phases in barium titanate would essentially exist due to the thermal fluctuations, while the rhombohedral phase would survive only at sufficiently low temperatures, where the fluctuations are weak enough. Thus, the analysis based upon the effective Hamiltonian (1) supports the conjecture about the fluctuation stabilization of the high-temperature ferroelectric phases in $BaTiO_3$ which was first formulated within the microscopic theory [5].

This conjecture looks rather attractive. It is worthy of a more detailed discussion. It turns out that, apart from the results of the first-order calculations, there exist two additional arguments in favor of the scenario just described. The first is as follows. As we have

already seen, the lowest order correction to β_1^f is considerable and, therefore, the higher order fluctuation contributions can influence the results appreciably. The leading perturbative term shifting the first-order estimates is the second-order one, and it's sign is opposite to that of $B_1^{(1)}$. One can show that account of the positive second-order fluctuation term in the course of fitting to the experimental data [2] results in the upward shift of the estimated value of β_1^f. Hence, within the refined theory, the fluctuation origin of the tetragonal and orthorhombic phases in $BaTiO_3$ would become more plausible.

The second argument deals with the fluctuation corrections to the sixth-order coefficients in the Landau–Devonshire expansion. Let us calculate them. Evaluating the six-leg one-loop diagram, we arrive at the following expressions for Γ_i:

$$\begin{aligned}\Gamma_1 &= \gamma_1 - f(T)(120\beta_1\gamma_1 + 6\beta_1\gamma_2 + 10\beta_2\gamma_1 + 18\beta_2\gamma_2),\\ \Gamma_2 &= \gamma_2 - f(T)(5\beta_1\gamma_1 + 63\beta_1\gamma_2 + 2\beta_1\gamma_3\\ &\quad + 15\beta_2\gamma_1 + 63\beta_2\gamma_2 + 6\beta_2\gamma_3),\\ \Gamma_3 &= \gamma_3 - f(T)(18\beta_1\gamma_2 + 24\beta_1\gamma_3 + 54\beta_2\gamma_2 + 58\beta_2\gamma_3),\end{aligned} \tag{7}$$

where $f(T) = k_B T\sqrt{C\epsilon_0}\,(10\pi s^3\sqrt{T - T_0})^{-1}$.

The above formulas are written for the physical case where the polarization vector has three Cartesian components. In fact, the fluctuation terms were calculated for the generic model with the n-vector order parameter. It was done in order to reserve an opportunity for the independent check of the results obtained. Indeed, as is well known, the model with cubic anisotropy possesses a special symmetry property for $n = 2$: if one turns the field (ϕ_1, ϕ_2) by 45° in its two-dimensional space, the coupling constants will transform, but the structure of the Hamiltonian will remain unchanged. This implies some exact symmetry relations between coupling constants [11], which interrelate dressed (B_i, Γ_i) and bare (β_i, γ_i) couplings and can be used to accept (or disregard) the results of perturbative calculations in the arbitrary order. Having made such a verification, we found that the n-vector analog of Eqs. (7) does obey these symmetry relations when $n = 2$.

To estimate the magnitudes of fluctuation corrections $\Gamma_i^{(1)}$, experimental information about γ_i is necessary. The experiments, however, were carried out in the ordered (tetragonal) phase and yielded, in particular, a strong dependence of Γ_1 on temperature. This temperature dependence was already noted to be so dramatic that, being extrapolated to the paraelectric region, it makes the Landau–Devonshire form unstable for $T > T_c + 50$ K. It is hardly believed therefore that the experimental data available can be used to extract more or less reliable estimates for γ_i.

In such a situation, it is natural to analyze the general structure of the correction terms $\Gamma_i^{(1)}$ in Eqs. (7) with the hope of finding some conclusions that are insensitive to particular values of γ_i. Let us proceed by accepting that $\gamma_1 \sim \gamma_2 \sim \gamma_3$. As we have already found, in barium titanate $|\beta_2| \ll |\beta_1|$. This means that the magnitudes of $\Gamma_i^{(1)}$ are in fact determined by the terms in Eqs. (7) containing Γ_1. The numerical coefficients of these terms are seen to be markedly different. The largest one (120) stands in the expression for $\Gamma_1^{(1)}$, making Γ_1 more strongly dependent on temperature than the other two coefficients. Moreover, the structure of $\Gamma_1^{(1)}$ fixes its sign. Since $\beta_1 > 0$, $\Gamma_1^{(1)}$ is negative and the fluctuations diminish the Landau–Devonshire coefficient γ_1, provided $\gamma_1 > 0$. The positiveness of γ_1 is, in its turn, inevitable, because this coefficient is responsible for the global stability of the system outside the fluctuation region.

So, we see that, when approaching T_c, the coefficient Γ_1 decreases more rapidly than Γ_2 and Γ_3. On the other hand, as one can see, the smaller Γ_1, the more stable the tetragonal phase. Hence, the fluctuations modify the sixth-order form in the Landau–Devonshire expansion in a way that favors the transition to the tetragonal phase. It confirms the conjecture about the fluctuation stabilization of the phases lying between the cubic and rhombohedral ones in the phase diagram of barium titanate.

To conclude, we have shown that the temperature dependence of the quartic Landau–Devonshire coefficients in a paraelectric phase of $BaTiO_3$ can be explained by the fluctuation effect. The theory which was developed naturally accounts for the signs of the temperature variations of B_1 and makes it clear why the second coefficient, B_2, is temperature-independent. A conjecture was formulated that the true Landau–Devonshire form for $BaTiO_3$ with the temperature-independent coefficients favors the transition from cubic to the rhombohedral phase, and it is the thermal fluctuations that stabilize the tetragonal and orthorhombic phases and provide the space for them in the phase diagram.

This work was supported by the Russian Foundation for Basic Research (project no. 01-02-17048) (A.I.S.), the Ministry of Education of the Russian Federation (project no. E00-3.2-132) (A.I.S.), and the Swiss National Science Foundation (A.K.T.). A.I.S. has benefited from the hospitality of the Laboratoire de Céramique, Ecole Polytechnique Fédérale de Lausanne, where this research was done.

REFERENCES

1. A. F. Devonshire, Philos. Mag. **40**, 1040 (1949); **42**, 1065 (1951).
2. M. E. Drougard, R. Landauer, and D. R. Young, Phys. Rev. **98**, 1010 (1955).
3. E. J. Huibregtse and D. R. Young, Phys. Rev. **103**, 1705 (1956).
4. W. R. Buessem, L. E. Cross, and A. K. Goswami, J. Am. Ceram. Soc. **49**, 33 (1966).
5. V. G. Vaks, *Introduction to the Microscopic Theory of Ferroelectrics* (Nauka, Moscow, 1973).
6. A. J. Bell and L. E. Cross, Ferroelectrics **59**, 197 (1984).
7. A. J. Bell, J. Appl. Phys. **89**, 3907 (2001).
8. A. I. Sokolov, Pis'ma Zh. Éksp. Teor. Fiz. **22**, 199 (1975) [JETP Lett. **22**, 92 (1975)].
9. A. I. Sokolov and A. K. Tagantsev, Zh. Éksp. Teor. Fiz. **76**, 181 (1979) [Sov. Phys. JETP **49**, 92 (1979)].
10. V. G. Vaks, Zh. Éksp. Teor. Fiz. **58**, 296 (1970) [Sov. Phys. JETP **31**, 161 (1970)].
11. D. V. Pakhnin and A. I. Sokolov, Phys. Rev. B **64**, 094407 (2001).

JETP Letters, Vol. 75, No. 8, 2002, pp. 415–417. Translated from Pis'ma v Zhurnal Éksperimental'noĭ i Teoreticheskoĭ Fiziki, Vol. 75, No. 8, 2002, pp. 488–490.

Critical Behavior of Heat Capacity of the $SC(NH_2)_2$ Ferroelectric in the Region of Incommensurate Phase Transition

S. N. Kallaev, I. K. Kamilov*, A. M. Aliev, Sh. B. Abdulvagidov, and A. B. Batdalov

Institute of Physics, Dagestan Scientific Center, Russian Academy of Sciences, ul. 26 Bakinskikh Komissarov 94, Makhachkala, 367003 Russia

** e-mail: analit@dinet.ru*

Received March 19, 2002

The anomalous (nonclassical) behavior of heat capacity in the region of the second-order phase transition "initial phase–incommensurate phase" was experimentally observed in the $SC(NH_2)_2$ ferroelectric. Such a critical behavior of heat capacity above and below the temperature of incommensurate phase transition is shown to be qualitatively consistent with the fluctuation theory of *XY*-type systems. © *2002 MAIK "Nauka/Interperiodica".*

PACS numbers: 65.40.Ba; 64.70.Rh; 77.80.Bh

Heat capacity is one of the most fundamental properties that exhibit a temperature anomaly in phase transitions. To explain the anomalies of heat capacity of ferroelectrics in the region of consecutive transitions "initial phase–incommensurate phase–polar phase," one usually invokes the Landau theory because of its remarkable simplicity. However, the thermodynamic Landau model qualitatively reproduces the anomalous part of the heat capacity of the incommensurate phase only in the temperature range adjacent to the first-order transition "incommensurate phase–commensurate ferroelectric phase." Experimental studies of a number of physical properties in the region of the second-order phase transition "initial phase–incommensurate phase" demonstrate dramatic deviations from classical Landau behavior both above and below the transition. The interpretation usually amounts to comparing the measured critical indices with the corresponding theoretical values adopted in the *XY*-type model.

The deviations from the behavior predicted by the Landau theory and from regular behavior may be due not only to fluctuations but also to defects [1]. However, the defect theory has not been adequately developed for the *XY* systems and incommensurate phases in particular; it does not account for the temperature dependences and critical amplitudes of deviations in both phases, which is necessary for the description of the experiment.

To elucidate the possible nature of deviations from the Landau theory, Levanyuk *et al.* [2] developed a method for the analysis of the experimental data in the region of structural transitions on the basis of fluctuation theory. As a result, it was shown by the example of birefringence and thermal expansion coefficients of a ferroelectric crystal [2, 3] that, in the vicinity $G \ll |\tau| \ll G^{1/2}$ of the transition to the incommensurate phase at temperature T_i (G is the Ginzburg number expressed in terms of the coefficients of thermodynamic potential [4], and $\tau = T/T_i - 1$ is the reduced temperature), the diverging corrections no longer approximate the experiment for $|\tau| \le 10^{-1}$. These corrections become large for the incommensurate transitions in various crystals at reduced temperatures $|\tau|$ on the order of $G \approx 10^{-2}$ (the value of correction achieves the jump magnitude), which can be taken as the experimental estimate of the Ginzburg number G. If G is not too small, not only does the anomaly become broad but all the conclusions also become qualitative.

It is worth noting that the weakness of previous experimental studies (their authors admit this fact themselves) is that the critical index α is estimated indirectly (see, e.g., [2, 3]) and, in some cases, the accuracy of measurements does not satisfy due requirements. In this regard, the elucidation of the role of fluctuation effects in the transition to the incommensurate phases in crystals of different types is of fundamental importance. In this work, with the aim of gaining direct information on the nature of the incommensurate phase, we undertook a careful experimental investigation of the critical behavior of specific heat in the region of the structural transition to the incommensurate phase in the $SC(NH_2)_2$ ferroelectric with a one-component order parameter.

$SC(NH_2)_2$ is a well-known molecular crystal which undergoes an intricate sequence of structural phase transitions, including transitions to the polar and nonpolar phases with incommensurate and long-period structures in the region between the initial nonpolar phase D_{2h}^{16} ($T_i \approx 202$ K) and the ferroelectric phase C_{2v}^{2} ($T_c \approx 169$ K) [1]. Below the temperature $T_i \approx 202$ K, an incommensurate superstructure appears with the modulation wave vector along the *b* axis. The studies were carried out with $SC(NH_2)_2$ single-crystals (unit-cell

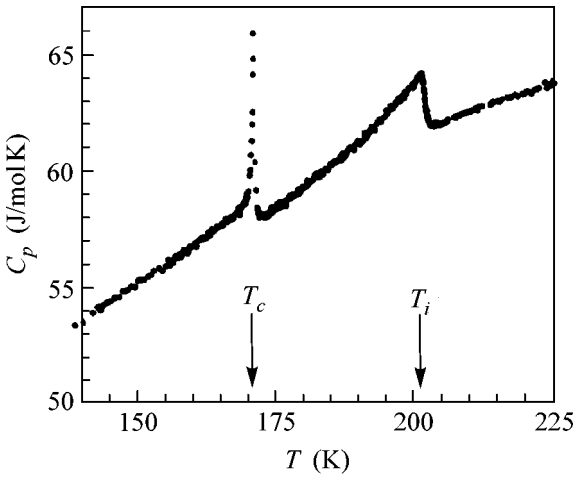

Fig. 1. Temperature dependence of the specific heat C_p of $SC(NH_2)_2$ in the region of phase transitions.

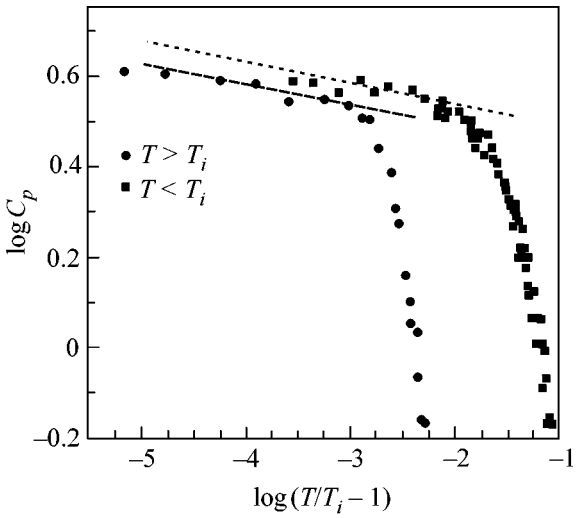

Fig. 2. Log–log plot of the anomalous part of specific heat of $SC(NH_2)_2$ against the reduced temperature $\tau = T/T_i - 1$; $T_i = 201.58$ K.

parameters $a = 7.655$, $b = 8.537$, $c = 5.520$ Å) grown from solution by the temperature lowering method. The geometric sizes of the samples were $0.50 \times 0.45 \times 0.025$ cm and their quality was monitored using an optical microscope. The studies were carried out on an automated setup for measuring the specific heat of small samples by ac calorimetry with a relative accuracy no worse than 0.1% [5]. The average temperature in the calorimeter was measured by a copper–constantan thermocouple with a wire diameter of 100 μm, and the temperature oscillations were measured by a Chromel–constantan thermocouple with a wire diameter of 25 μm. The temperature variation rate did not exceed 0.01 K/min; in the vicinity of transition, it did not exceed 0.005 K. The accuracy of stabilizing the cryostat temperature was no worse than 0.005 K. The measuring process and the processing of experimental data were controlled by the program HEAT-MASTER for the automation of thermophysical measurements.

The results of measuring the specific heat C_p of the $SC(NH_2)_2$ crystal in the temperature range of the second-order structural transition "initial phase–incommensurate phase" at T_i and the first-order transition "incommensurate phase–polar phase" at T_c are presented in Fig. 1. We will focus on the anomaly of C_p in the region of the second-order phase transition "initial phase–incommensurate phase" at $T_i = 201.58$ K. The changes in enthalpy and entropy at the transition point T_i are, respectively, $\Delta H_{trs} = 7.4$ kJ/mol and $\Delta S_{trs} = 68$ J/(mol K).

According to [2–4], the experimental temperature dependence of heat capacity can be represented as the sum of Landau and fluctuation contributions:

$$\begin{aligned} C^+ &= C_b + \lambda^+ \tau^{-1/2} \quad \text{at} \quad T > T_i, \\ C^- &= C_b + C_L + \lambda^- |\tau|^{-1/2} \quad \text{at} \quad T < T_i, \end{aligned} \tag{1}$$

where C_b is the regular part of heat capacity, C_L is the heat capacity jump at $T = T_i$ (according to Landau), λ^+ and λ^- are constants, and the ratio λ^-/λ^+ is $\sqrt{2}$ for the *XY*-type systems and $2\sqrt{2}$ for the Ising systems.

As with the temperature dependences of birefringence and thermal expansion coefficients obtained in [2, 3], Eq. (1), with $C_L = \text{const}$ and $\lambda^\pm = \text{const}$, properly approximates the experiment only if $C_b \neq \text{const}$ (this imposes a limitation on the domain of applicability of the Landau theory). We will assume that the regular part can be represented as a polynomial suitable for the description of empirical data on the thermal characteristics of solids [6] in a limited temperature range on the order of the Debye temperature:

$$C_b = c_0 + c_1 t + c_2 t^2,$$

where $t = T - T_i$. In this case, Eq. (1) approximates well the experimental dependences in the region from $1 \le t \le 70$ K and -2 K $< t \le -20$ K (Fig. 1).

According to Eq. (1), the ratio of critical amplitudes λ^-/λ^+ derived from the measurements of heat capacity ($\lambda^+ = 0.0598 \pm 0.0033$ and $\lambda^- = 0.0862 \pm 0.0038$ for $T > T_i$ and $T < T_i$, respectively) is equal to 1.441, which corresponds to the theoretical estimate $\sqrt{2}$ for the *XY*-type systems ($2\sqrt{2}$ for the Ising systems). It follows from the experimental data that the Ginzburg number is $G \approx 1\text{–}2 \times 10^{-2}$. Therefore, the corrections are small in the temperature region $|\tau| > G$, while anomalous scaling behavior can be expected at $|\tau| < |G|$.

The dependence of $\log\Delta C_p$ on $\log\tau$ above and below the transition point T_i, where ΔC_p is the singular part of the specific heat, is shown for the $SC(NH_2)_2$ crystal in Fig. 2. Experiment shows that the specific heat of $SC(NH_2)_2$ exhibits anomalous (nonclassical) behavior above T_i in the temperature range 0.02 K < $(T - T_i)$ < 0.36 K ($1.0 \times 10^{-4} < |\tau| < 0.18 \times 10^{-2}$) and below T_i in the range 0.05 K < $|T_i - T|$ < 1.82 K ($2.5 \times 10^{-4} < |\tau| < 0.9 \times 10^{-2}$), with the critical indices being, respectively, $\alpha = -0.0394 \pm 0.0099$ and $\alpha' = -0.0428 \pm 0.0094$, which is in qualitative agreement with the fluctuation theory (the Landau value is $\alpha = 0$).

Note that the value obtained for α correlates with the results of studies where the critical index α was estimated indirectly for the improper ferroelectric Rb_2ZnBr_4 by the birefringence ($\alpha = -0.05 \pm 0.02$) [2] and thermal expansion ($0 < |\alpha| < 0.07$) [3] methods.

Recall that the known calculated value for the *XY* model lies in the range $-0.04 \le \alpha < 0$ [7]. Nevertheless, our conclusions about the critical index are only qualitative because the "infinitely sharp" scaling peak is not observed experimentally.

In summary, the results of our study on the specific heat of $SC(NH_2)_2$ and the corresponding theoretical analysis, according to [2], provide evidence that there is a critical region in the vicinity of the incommensurate phase transition T_i, where the anomalous behavior agrees qualitatively with the theory making allowance for the critical fluctuations of order parameter.

This work was supported by the Russian Foundation for Basic Research (project nos. 02-02-17864, 00-07-90241, 00-15-96662, 02-07-06048) and the program "Integratsiya" (project no. IO227).

REFERENCES

1. *Incommensurate Phases in Dielectrics*, Ed. by R. Blinc and A. P. Levanyuk (North-Holland, Amsterdam, 1986), Vols. 1, 2.
2. N. R. Ivanov, A. P. Levanyuk, S. A. Minyukov, *et al.*, Ferroelectrics **96**, 83 (1989).
3. N. R. Ivanov and J. Fousek, Izv. Akad. Nauk SSSR, Ser. Fiz. **54**, 659 (1990).
4. A. Z. Patashinskiĭ and V. L. Pokrovskiĭ, *Fluctuation Theory of Phase Transitions* (Nauka, Moscow, 1982; Pergamon, Oxford, 1979).
5. Sh. B. Abdulvagidov, G. M. Shakhshaev, and I. K. Kamilov, Prib. Tekh. Éksp., No. 5, 134 (1996).
6. S. I. Novikova, *Thermal Expansion of Solids* (Nauka, Moscow, 1974).
7. S. Ma, *Modern Theory of Critical Phenomena* (Benjamin, Reading, 1976; Mir, Moscow, 1980).

Translated by V. Sakun

JETP Letters, Vol. 75, No. 8, 2002, pp. 418–422. From Pis'ma v Zhurnal Éksperimental'noĭ i Teoreticheskoĭ Fiziki, Vol. 75, No. 8, 2002, pp. 491–495.

On the Kelvin–Helmholtz Instability in Superfluids[1]

G. E. Volovik

Low Temperature Laboratory, Helsinki University of Technology, FIN-02015 HUT, Finland
Landau Institute for Theoretical Physics, Russian Academy of Sciences, ul. Kosygina 2, Moscow, 117940 Russia

Received March 19, 2002

The Kelvin–Helmholtz instability in superfluids is discussed on the basis of the first experimental observation of such an instability at the interface between superfluid ^{3}He-A and superfluid ^{3}He-B (R. Blaauwgeers, V. B. Eltsov, G. Eska *et al.*, cond-mat/0111343). We discuss why the Kelvin–Helmholtz criterion, the Landau critical velocity for nucleation of ripplons, and the free-energy consideration all give different values for the instability threshold. © *2002 MAIK "Nauka/Interperiodica".*

PACS numbers: 67.57.Np; 47.20.Ma; 68.05.-n

1. Classical Kelvin–Helmholtz (KH) instability. KH instability belongs to a broad class of interfacial instabilities in liquids, gases, plasmas, etc. [1]. It refers to the dynamic instability of the interface of a discontinuous flow, and may be defined as the instability of the vortex sheet. Many natural phenomena have been attributed to this instability. The most familiar of these are the generation of waves in the water by wind, whose Helmholtz instability [2] was first analyzed by Kelvin [3], and the flapping of sails and flags analyzed by Rayleigh [4] (see recent experiments in [5]).

Many of the leading ideas in the theory of instability were originally inspired by considerations about inviscid flows. The corrugation instability of the interface between two ideal liquids sliding along one other was first investigated by Lord Kelvin [3, 6]. The critical relative velocity $|v_1 - v_2|$ for the onset of corrugation instability is given by

$$\frac{1}{2}\frac{\rho_1\rho_2}{\rho_1+\rho_2}2(v_1-v_2)^2 = \sqrt{\sigma F}. \quad (1)$$

Here, σ is the surface tension of the interface between two liquids; ρ_1 and ρ_2 are their mass densities; and F is related to the external field stabilizing the position of the interface: typically, it is the gravitational field

$$F = g(\rho_1-\rho_2). \quad (2)$$

The surface mode (ripplon) which is excited first has the wave vector

$$k_0 = \sqrt{F/\sigma} \quad (3)$$

and frequency

$$\omega_0 = k_0\frac{\rho_1 v_1+\rho_2 v_2}{\rho_1+\rho_2}. \quad (4)$$

The excited ripplon propagates along the interface with the phase and group velocity $v_{\text{ripplon}} = (\rho_1 v_1 + \rho_2 v_2)/(\rho_1 + \rho_2)$.

However, among the ordinary liquids one cannot find an ideal one. That is why in ordinary liquids and gases it is not easy to correlate theory with experiment. In particular, this is because one cannot properly prepare the initial state; the planar vortex sheet is never in equilibrium in a viscous fluid: it is not a solution for the hydrodynamic equations if viscosity is finite. That is why it is not quite apparent whether one can properly discuss its "instability."

Superfluids are the only proper ideal objects where these ideas can be implemented without reservations and where the criterion of instability does not contain viscosity. Recently, the first experiment was performed in superfluids, where the nondissipative initial state was well determined, and a well-defined threshold was reported [7]. The initial state is the nondissipative vortex sheet separating two sliding superfluids. One of the superfluids (^{3}He-A) performs a solid-body-like rotation together with the vessel, while in the other one (^{3}He-B) the superfluid component is in the so-called Landau state; i.e., it is vortex-free and thus is stationary in the inertial frame. The threshold of a Kelvin–Helmholtz-type instability has been marked by the formation of vortices in the vortex-free stationary superfluid: this initially stationary superfluid starts to spin up by the neighboring rotating superfluid.

2. KH instability in superfluids at low *T*. The extension of the consideration of a classical KH instability to superfluids adds some new physics. First of all, it is now the two-fluid hydrodynamics with superfluid and normal components which must be incorporated. Let us first consider the limiting case of low T, where the fraction of the normal component is negligibly small and thus the complication of the two-fluid hydrodynamics is avoided. In this case, one may guess that

[1] This article was submitted by the author in English.

the classical result (1) obtained for ideal inviscid liquids applies to superfluids as well and the only difference is that the role of gravity is played by the applied gradient of magnetic field H, which stabilizes the position of the interface between ^{3}He-A and ^{3}He-B in the experiment [7]:

$$F = (1/2)(\chi_A(T) - \chi_B(T))\nabla(H^2). \quad (5)$$

Here, χ_A and χ_B are the temperature-dependent magnetic susceptibilities of the A and B phases, respectively.

However, this is not the whole story. The instability will start earlier if one takes into account that there is a preferred reference frame. It can be the frame of the container, the frame of the crystal in superconductors, or even the frame where the inhomogeneity of magnetic field H is stationary. The energy of surface excitations (ripplons) can become negative in this reference frame, and the surface modes will be excited before the onset of the classical KH instability.

Let us consider this phenomenon. We repeat the same derivation as in case of classical KH instability assuming the same boundary conditions, but with one important modification: in the process of interface dynamics, one must add the friction force arising when the interface moves with respect to the container wall. In the frame of the container, which coincides with the frame of the stable interface position, the friction force between the interface and container is

$$F_{\text{friction}} = -\Gamma\partial_t\zeta, \quad (6)$$

where $\zeta(x, t)$ is the perturbation of the interface position

$$z = z_0 + \zeta(x, t), \quad \zeta(x, t) = a\sin(kx - \omega t). \quad (7)$$

We assume that both velocities v_1 and v_2 are along the x axis, the container walls are parallel to the (x, z) plane, and that the interface is parallel to the (x, y) plane.

The friction force in Eq. (6) violates the Galilean invariance in the x direction, which reflects the existence of the preferred reference frame—the frame of the container. This symmetry breaking is the main reason for the essential modification of the KH instability. The parameter Γ in the friction force was calculated for the case where the interaction between the interface and container is transferred by the normal component of the liquid due to the Andreev scattering of ballistic quasiparticles by the interface [8]. The friction modifies the classical spectrum of surface modes:

$$\rho_1\left(\frac{\omega}{k} - v_1\right)^2 + \rho_2\left(\frac{\omega}{k} - v_2\right)^2 = \frac{F + k^2\sigma}{k} - i\Gamma\frac{\omega}{k}, \quad (8)$$

or

$$\frac{\omega}{k} = \frac{\rho_1 v_1 + \rho_2 v_2}{\rho_1 + \rho_2} \pm \frac{1}{\sqrt{\rho_1 + \rho_2}} \times \sqrt{\frac{F + k^2\sigma}{k} - i\Gamma\frac{\omega}{k} - \frac{\rho_1\rho_2}{\rho_1 + \rho_2}(v_1 - v_2)^2}, \quad (9)$$

where v_1 and v_2 are the velocities of superfluid components of the liquids with respect to the container walls.

For $\Gamma = 0$, the spectrum of ripplons acquires the imaginary part, $\mathrm{Im}\,\omega(k) \neq 0$, at the classical threshold value in Eqs. (1) and (3). However, the frame-fixing parameter Γ leads to an essentially different result: the imaginary part of the frequency becomes positive, $\mathrm{Im}\,\omega(k) > 0$, first for ripplons with the same value of the wave vector as in Eq. (3), but the ripplon frequency is now $\omega = 0$ and its group velocity is $v_{\text{group}} = d\omega/dk = 0$. The critical ripplon is stationary in the reference frame of the container; as a result, the onset of instability is given by

$$\frac{1}{2}\rho_1 v_1^2 + \frac{1}{2}\rho_2 v_2^2 = \sqrt{\sigma F}. \quad (10)$$

This criterion does not depend on relative velocities of superfluids, but is determined by velocities of each of the two superfluids with respect to the container (or to the remnant normal component). Thus, the instability can occur even if two liquids have equal densities, $\rho_1 = \rho_2$, and move with the same velocity, $v_1 = v_2$. This situation is very similar to the phenomenon of a flapping flag in wind, discussed by Rayleigh in terms of the KH instability—the instability of the passive deformable membrane between two distinct parallel streams having the same density and the same velocity (see latest experiments in [5]). In our case, the role of the flag is played by the interface, while the role of the flagpole, which pins the flag (and thus breaks the Galilean invariance), is played by the container wall.

Note that, in the limit of vanishing pinning parameter $\Gamma \longrightarrow 0$, Eq. (10) does not coincide with the classical Eq. (1) obtained when there is no pinning, i.e. when Γ is exactly zero. Such a difference between the limiting and exact cases is known in many areas of physics. In classical hydrodynamics, the normal mode of inviscid theory may not be the limit of a normal mode of viscous theory [9]. Below, we discuss this difference for the case of KH instability in superfluids.

3. KH instability and modified Landau criterion. Let us first compare both results, with no pinning ($\Gamma = 0$) and for vanishing pinning ($\Gamma \longrightarrow 0$), with the Landau criterion. According to Landau, a quasiparticle is created by the moving superfluid if its velocity with respect to the container wall (or with respect to the body moving in the superfluid) exceeds

$$v_{\text{Landau}} = \min\frac{E(p)}{p}. \quad (11)$$

Recall that the energy $E(p)$ here is the quasiparticle energy in the reference frame moving with the superfluid vacuum. In our case, there are two superfluids moving with different velocities. That is why there is no unique superfluid-comoving frame where $E(p)$ could be uniquely determined. Such a frame appears only in particular cases, where either $v_1 = v_2$ or if instead of the interface one considers the free surface of a single liquid (i.e., if $\rho_2 = 0$). In these particular cases, the Landau criterion in the form of Eq. (11) must work. The energy spectrum of the ripplons at the interface between two stationary fluids (or at the surface of a single liquid) is given by Eq. (9) with $v_1 = v_2 = \Gamma = 0$:

$$\frac{\omega^2(k)}{k^2} = \frac{1}{\rho_1 + \rho_2}\frac{F + k^2\sigma}{k}. \quad (12)$$

This gives the following Landau critical velocity:

$$v^2_{\text{Landau}} = \min\frac{\omega^2(k)}{k^2} = \frac{2}{\rho_1 + \rho_2}\sqrt{F\sigma}. \quad (13)$$

This coincides with Eq. (10) if $v_1 = v_2$ or if $\rho_2 = 0$. But this does not coincide with the classical KH result: the latter is obtained at $\Gamma = 0$ when the interaction with the reference frame of the container is lost, and thus the Landau criterion does not apply.

In the general case, where neither of the two conditions ($v_1 = v_2$ or $\rho_2 = 0$) is fulfilled, the Landau criterion must be reformulated: the instability occurs when the frequency of the surface mode in the frame of the container crosses zero for the first time: $\omega(k; v_1, v_2) = 0$. Inspection of Eq. (9) with $\Gamma = 0$ shows that for $k = k_0$ the spectrum with a negative square root touches zero just when the threshold (10) is reached. Thus, the Landau criterion in its general formulation coincides with the criterion for instability obtained for the case of nonzero friction force. As distinct from the Landau criterion in the form of Eq. (11), which is valid for a single superfluid velocity, where it suffices to know the ripplon spectrum in the frame where the superfluid(s) is (are) at rest, in the general case one must calculate the ripplon spectrum $\omega(k; v_1, v_2)$ for the relatively moving superfluids.

4. Matching zero-pinning and vanishing-pinning regimes. The difference in the result for the onset of KH instability in two regimes—with $\Gamma = 0$ and with $\Gamma \neq 0$—disappears only in the case where two superfluids move in such a way that in the reference frame of the container the combination $\rho_1 v_1 + \rho_2 v_2 = 0$. In this arrangement, according to Eq. (4), the frequency of the ripplon created by classical KH instability is zero in the container frame. Thus, under this special condition, in the two criteria, zero pinning (1) and vanishing pinning (10), must coincide; and reality, they do.

If $\rho_1 v_1 + \rho_2 v_2 \neq 0$, the crossover between the zero-pinning regime and the regime of small pinning occurs by varying the observation time. Let us consider this by the example of the experimental setup [7] with the vortex-free B phase and the vortex-full A phase in the rotating vessel. In the container frame, one has $\mathbf{v}_1 = \mathbf{v}_{sA} = 0$, $\mathbf{v}_2 = \mathbf{v}_{sB} = -\Omega \times \mathbf{r}$; the densities of two liquids, ^{3}He-A and ^{3}He-B, are the same with a high accuracy: $\rho_A = \rho_B = \rho$. In the nonzero-pinning regime, the instability occurs at the boundary of the vessel, where the velocity of ^{3}He-B is maximal, when this maximal velocity reaches the value

$$v_c^2 = \frac{2}{\rho}\sqrt{F\sigma} = \frac{1}{2}v^2_{\text{KH}} = 2v^2_{\text{Landau}}. \quad (14)$$

This velocity is by a factor of $\sqrt{2}$ smaller than that given by the classical KH equation (1) for the zero-pinning regime. On the other hand, it is $\sqrt{2}$ times larger than the Landau criterion in the form of Eq. (11) but coincides with the Landau criterion properly formulated for two superfluids.

From Eq. (8), it follows that slightly above this treshold the increment of the exponential growth of the interface perturbation is

$$\text{Im}\,\omega(k_0) = \frac{\Gamma k_0}{2\rho}\left(\frac{v_{sB}}{v_c} - 1\right), \quad \text{at} \quad v_{sB} - v_c \ll v_c. \quad (15)$$

In the vanishing-pinning limit $\Gamma \longrightarrow 0$, the increment becomes small and the discussed instability of the surface has no time to develop if the observation time is short enough. It will start only at a higher velocity of rotation when the classical threshold of KH instability, v_{KH} in Eq. (1), is reached. Thus, experimental results in this limit would depend on the observation time—the time one waits for the interface to be coupled to the laboratory frame and for the instability to develop. For a sufficiently short time, one will measure the classical KH criterion (1), while, for a sufficiently long observation time, the modified KH criterion (14) will be observed.

5. Thermodynamic instability. Let us now consider the case of nonzero T, where each of the two liquids contains a superfluid and normal components. In this case, the analysis requires the 2×2 fluid hydrodynamics. This appears to be a rather complicated problem if it is taken into account that, in some cases, the additional degrees of freedom related to the interface itself must also be added. The two-fluid hydrodynamics was used for the investigation of the instability of a free surface of superfluid ^{4}He using the relative motion of the normal component of the liquid with respect to the superfluid one [10]. We avoid all of these complications assuming that the viscosity of the normal components of both liquids is high, as it actually is in superfluid ^{3}He. In this high-viscosity limit, we can neglect the dynamics of normal components, which is thus fixed by the container walls. Then, the problem is reduced to the problem of the thermodynamic instability of the superflow in the presence of the interface.

We start with the following initial nondissipative state corresponding to the thermal equilibrium in the presence of the interface and superflows. In thermal equilibrium, the normal component must be at rest in the container frame, $\mathbf{v}_{n1} = \mathbf{v}_{n2} = 0$, while the superfluids can move along the interface with velocities $\mathbf{v}_{s1}$ and $\mathbf{v}_{s2}$ (here, the velocities are in the frame of the container).

The onset of instability can be found from free-energy considerations: when the free energy of static perturbations of the interface becomes negative in the frame of the container, the initial state becomes thermodynamically unstable. The free-energy functional for the perturbations of the interface in the reference frame of the container is determined by "gravity," surface tension, and perturbations $\tilde{\mathbf{v}}_{s1} = \nabla\Phi_1$ and $\tilde{\mathbf{v}}_{s2} = \nabla\Phi_2$ of the velocity field caused by deformation of the interface:

$$\mathcal{F}\{\zeta\} = \frac{1}{2}\int dx\Bigg(F\zeta^2 + \sigma(\partial_x\zeta)^2 + \int_{-\infty}^{\zeta} dz\rho_{s1ik}\tilde{v}^i_{s1}\tilde{v}^k_{s1} + \int_{\zeta}^{\infty} dz\rho_{s2ik}\tilde{v}^i_{s2}\tilde{v}^k_{s2}\Bigg). \tag{16}$$

For generality, we discuss anisotropic superfluids, whose superfluid densities are tensors (this occurs in ^{3}He-A). The velocity perturbation fields $\tilde{v}_{sk} = \nabla\Phi_k$, obeying the continuity equations $\partial_i(\rho_s^{ik}\tilde{v}_{sk}) = 0$, have the following form:

$$\Phi_1(x, z<0) = A_1 e^{k_1 z}\cos kx, \qquad \Phi_2(x, z>0) = A_2 e^{-k_2 z}\cos kx, \tag{17}$$

$$\rho_{s1z}k_1^2 = \rho_{s1x}k^2, \quad \rho_{s2z}k_2^2 = \rho_{s2x}k^2. \tag{18}$$

The connection between the surface deformation, $\zeta(x) = a\sin kx$, and the velocity perturbations follows from the boundary conditions.

Because of the large viscosity of the normal component, it is clamped by the boundaries of the vessel. Then, from the requirement that the mass and the heat currents be conserved across the wall, one finds that the superfluid velocity in the direction normal to the wall must be zero: $\mathbf{v}_{s1}\cdot\mathbf{n} = \mathbf{v}_{s2}\cdot\mathbf{n} = 0$. This gives the following boundary conditions for perturbations:

$$\partial_z\Phi_1 = v_{s1}\partial_x\zeta, \quad \partial_z\Phi_2 = v_{s2}\partial_x\zeta. \tag{19}$$

Substituting this into the free-energy functional (16), one obtains the quadratic form of the free energy of the surface modes:

$$\mathcal{F}\{\zeta\} = \frac{1}{2}\sum_k |\zeta_k|^2 \times (F + k^2\sigma - k(\sqrt{\rho_{sx1}\rho_{sz1}}\,v_{s1}^2 + \sqrt{\rho_{sx2}\rho_{sz2}}\,v_{s2}^2)). \tag{20}$$

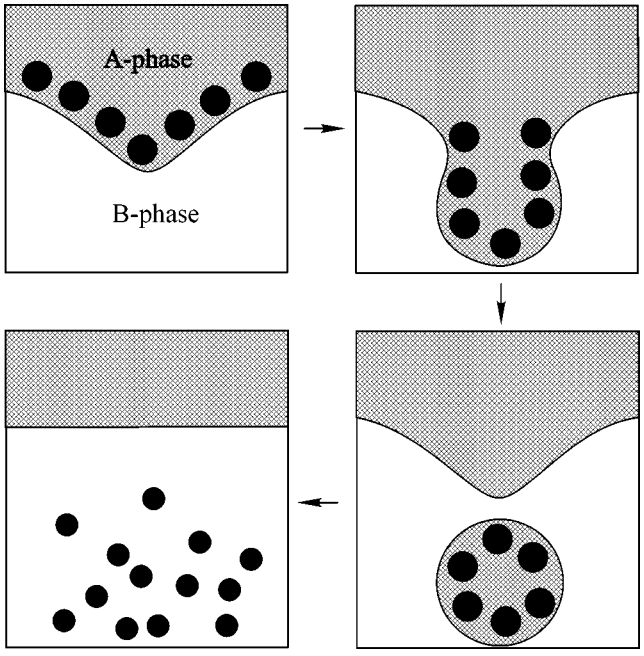

Possible scenario of vortex formation by Kelvin–Helmholtz instability of the AB interface

This energy becomes negative for the first time for the mode with $k_0 = (F/\sigma)^{1/2}$ when

$$\frac{1}{2}(\sqrt{\rho_{sx1}\rho_{sz1}}\,v_{s1}^2 + \sqrt{\rho_{sx2}\rho_{sz2}}\,v_{s2}^2) = \sqrt{\sigma F}\,. \tag{21}$$

This is the criterion (10) for the nonzero-pinning regime extended to finite temperatures. Equation (21) transforms to Eq. (10) when $T \longrightarrow 0$; the normal components of the liquids disappear, and one has $\rho_{sx1} = \rho_{sz1} = \rho_1$ and $\rho_{sx2} = \rho_{sz2} = \rho_2$.

6. Nonlinear stage of instability. Equation (21) is in excellent agreement with the onset of the surface instability measured in experiment [7]. The onset of the instability is marked by the appearance of the vortex lines in ^{3}He-B, which are monitored by NMR measurements. This demonstrates that vortices appear in the nonlinear stage of this KH instability.

The precise mechanism of the vortex formation is still unknown. One may guess that the A-phase vorticity is pushed by the Magnus force towards the vortex-free B-phase region [11]. When the potential well for vortices is formed by the corrugation of the interface (see figure), the vortices are pushed there and further enhance the growth of the potential well, until it forms a droplet of the A phase filled with vorticity. The vortex-full droplet propagates to the bulk B phase, where it relaxes to the singular vortex lines of ^{3}He-B.

Under the conditions of the experiment, the nucleation of vortices leads to a decrease of the B-phase velocity below the instability threshold and the vortex

formation is stopped. That is why one can expect that the vortex-full droplet is nucleated during the development of the instability from a single seed. The size of the seed is about one-half of the wavelength $\lambda_0 = 2\pi/k_0$ of the perturbation. The number of vortices created is found from the circulation of superfluid velocity carried by a piece of the vortex sheet of size $\lambda_0/2$, which is determined by the jump of superfluid velocity across the sheet: $\kappa = |v_{sB} - v_{sA}|\lambda_0/2$. Dividing this by the circulation quantum $\mathbf{k}$ of the created B-phase vortices, one obtains the number of vortices produced as a result of the growth of one segment of perturbation:

$$N = \frac{\kappa}{\kappa_0} \sim \frac{v_c \lambda_0}{2\kappa_0}. \quad (22)$$

It is equal to about 10 vortices per event under the conditions of the experiment, which is in a good agreement with the measured number of vortices created per event [7]. This counts in favor of the droplet mechanism of vortex formation.

In all likelihood, the experiments on KH instability in superfluids will allow one to solve the similar problem of the nonlinear stage of instability in ordinary liquids (see, for example, [12]).

The vortex formation by surface instability is a rather generic phenomenon. This mechanism has been discussed for vortex formation in the laser-manipulated Bose gases [13, 14]. It can apply to different kinds of interfaces and under very different physical conditions. In particular, vortices can be generated at the second-order phase boundary between the normal and the superfluid phases [15]. Such an interface naturally appears in the rapid phase transition to the superfluid state [16]. The instability of the free surface of a superfluid under the relative flow of the normal and superfluid components of the same liquid was recently reexamined by Korshunov [17]. He also obtained two criteria for instability: for zero and nonzero values of the viscosity of the normal component of the liquid.

I thank R. Blaauwgeers, V.B. Eltsov, N. Inogamov, N.B. Kopnin, S.E. Korshunov, M. Krusius, E.A. Kuznetsov, and E.V. Thuneberg for fruitful discussions. This work was supported by the ESF COSLAB program and by the Russian Foundation for Basic Research.

REFERENCES

1. G. Birkhoff, in *Hydrodynamic Instability: Proceedings of the 13th Symposium in Applied Mathematics, New York, 1960*, Ed. by G. Birkhoff, R. Bellman, and C. C. Lin (American Mathematical Society, Providence, 1962), p. 55.
2. H. L. F. von Helmholtz, *Monatsberichte der königl* (Akademie Wissenschaften, Berlin, 1868), p. 215.
3. Lord Kelvin (Sir W. Thomson), *Mathematical and Physical Papers*, Vol. 4: *Hydrodynamics and General Dynamics* (Cambridge Univ. Press, Cambridge, 1910).
4. Lord Rayleigh (J. W. Strutt), *Scientific Papers* (Cambridge Univ. Press, Cambridge, 1899), Vol. 1.
5. J. Zhang, S. Childress, A. Ubchaber, and M. Shelley, Nature **408**, 835 (2000).
6. L. D. Landau and E. M. Lifshitz, *Course of Theoretical Physics*, Vol. 6: *Fluid Mechanics* (Nauka, Moscow, 1986; Pergamon, New York, 1989), Sect. 62, Problem 3, p. 247.
7. R. Blaauwgeers, V. B. Eltsov, G. Eska, *et al.*, cond-mat/0111343.
8. N. B. Kopnin, Zh. Éksp. Teor. Fiz. **92**, 2106 (1987) [Sov. Phys. JETP **65**, 1187 (1987)]; A. J. Leggett and S. Yip, in *Helium Three*, Ed. by W. P. Halperin and L. P. Pitaevskii (Elsevier, Amsterdam, 1990), p. 523; S. Yip and A. J. Leggett, Phys. Rev. Lett. **57**, 345 (1986); J. Palmeri, Phys. Rev. B **42**, 4010 (1990).
9. C. C. Lin and D. J. Benney, in *Hydrodynamic Instability: Proceedings of the 13th Symposium in Applied Mathematics, New York, 1960*, Ed. by G. Birkhoff, R. Bellman, and C. C. Lin (American Mathematical Society, Providence, 1962), p. 1.
10. S. E. Korshunov, Europhys. Lett. **16**, 673 (1991).
11. M. Krusius, E. V. Thuneberg, and Ü. Parts, Physica B (Amsterdam) **197**, 367 (1994); Ü. Parts, Y. Kondo, J. S. Korhonen, *et al.*, Phys. Rev. Lett. **71**, 2951 (1993).
12. E. A. Kuznetsov and P. M. Lushnikov, Zh. Éksp. Teor. Fiz. **108**, 614 (1995) [JETP **81**, 332 (1995)].
13. K. W. Madison, F. Chevy, V. Bretin, and J. Dalibard, Phys. Rev. Lett. **86**, 4443 (2001).
14. S. Sinha and Y. Castin, Phys. Rev. Lett. **87**, 190402 (2001).
15. I. S. Aranson, N. B. Kopnin, and V. M. Vinokur, Phys. Rev. B **63**, 184501 (2001).
16. V. M. H. Ruutu, V. B. Eltsov, A. J. Gill, *et al.*, Nature **382**, 334 (1996).
17. S. E. Korshunov, Pis'ma Zh. Éksp. Teor. Fiz. **75** (8), 496 (2002) [JETP Lett. **75**, 423 (2002)].

JETP Letters, Vol. 75, No. 8, 2002, pp. 423–425. From Pis'ma v Zhurnal Éksperimental'noĭ i Teoreticheskoĭ Fiziki, Vol. 75, No. 8, 2002, pp. 496–498.

Analog of Kelvin–Helmholtz Instability on a Free Surface of a Superfluid Liquid[1]

S. E. Korshunov

Landau Institute for Theoretical Physics, Russian Academy of Sciences, ul. Kosygina 2, Moscow, 117940 Russia
e-mail: serkor@landau.ac.ru

Received March 19, 2002

We analyze the analog of the Kelvin–Helmholtz instability on the free surface of a superfluid liquid. This instability is induced by the relative motion of superfluid and normal components of the same liquid along the surface. The instability threshold is found to be independent of the value of viscosity, but turns out to be lower than in the absence of dissipation. The result is similar to that obtained for the interface between two sliding superfluids (with different mechanisms of dissipation) and confirmed by the first experimental observation of the Kelvin–Helmholtz instability on the interface between ^{3}He-A and ^{3}He-B by Blaauwgeers *et al.* (cond-mat/0111343). © *2002 MAIK "Nauka/Interperiodica".*

PACS numbers: 67.57.Np; 47.20.Ma; 68.03.Kn

1. INTRODUCTION

The Kelvin–Helmholtz instability [1] is a dynamic corrugation instability of the interface separating two liquids sliding with respect to each other. The concept of such instability was originally introduced when considering ideal liquids, and, in the presence of dissipation, it becomes ill-defined, because the relative motion of two liquids in contact with each other is no longer a solution to the hydrodynamic equations.

The simplest situation, where an equilibrium difference in velocities can be maintained at the surface of a liquid, is the relative motion of the superfluid and normal components (a counterflow) in superfluid ^{4}He. The corrugation instability of the free surface of a superfluid liquid in the presence of a counterflow along the surface was studied in [2] (in relation to the experiments of Egolf *et al.* [3]). It can be considered as an example of the Kelvin–Helmholtz instability, in which both liquids are located on the same side of the interface. An analogous instability can appear when superfluid ^{4}He slides along the atomically rough interface separating it from solid ^{4}He [4]. Such an interface is known to account for the equilibrium melting and crystallization of ^{4}He [5, 6], and, as a consequence, its behavior resembles that of the free surface of a liquid.

Recently, interest in surface instabilities of superfluids has been revived [7–9] in relation to the experiments on laser-manipulated Bose gases and the first experimental observation of the Kelvin–Helmholtz instability at the interface between two superfluids, ^{3}He-A and ^{3}He-B [10]. In particular, it has been demonstrated [9] that addition of a friction related to the motion of the interface with respect to container walls shifts the point of instability from the well-known classical threshold [1] to another value. This value does not depend on the strength of dissipation and can be reproduced in the framework of thermodynamic analysis by looking for the instability of free energy calculated in the reference frame of the normal component, which, in equilibrium, is at rest with respect to the container walls. The appearance of the same threshold in dynamic analysis was ascribed in [9] to the symmetry breaking related to the violation of the Galilean invariance by the considered friction force.

In this work, we return to the investigation of the corrugation instability on the free surface of a superfluid liquid in the presence of a counterflow [2] taking into account the viscosity of the normal component and show that, for any finite value of viscosity, the instability threshold is shifted to a viscosity-independent value, which is in agreement with the results of [9]. However, in our analysis, this phenomenon appears in the absence of the friction force violating the Galilean invariance. Therefore, the modification of the instability criterion in the presence of dissipation is not a consequence of the symmetry-breaking form of the friction, but has a more general nature.

2. DISPERSION RELATION

The calculation of the spectrum of surface oscillations in a superfluid liquid in the presence of a counterflow can be performed in the same way as the calculation of the spectrum of a gravitational wave in a normal liquid with finite viscosity [11]. For frequencies small in comparison with the frequency of the first and the second sound, the mass and the entropy densities can be

[1] This article was submitted by the author in English.

assumed to be constant. Accordingly, the conservation laws for mass and entropy are reduced to the constraints

$$\mathrm{div}\mathbf{v}_s = \mathrm{div}\mathbf{v}_n = 0, \tag{1}$$

where $\mathbf{v}_s$ and $\mathbf{v}_n$ are the superfluid and normal velocities, respectively. In this limit, the Navier–Stokes equation for a superfluid liquid can be written as [12]

$$\rho_s\left[\frac{\partial \mathbf{v}_s}{\partial t} + (\mathbf{v}_s\nabla)\mathbf{v}_s\right] + \rho_n\left[\frac{\partial \mathbf{v}_n}{\partial t} + (\mathbf{v}_n\nabla)\mathbf{v}_n\right] = -\nabla p - \rho\mathbf{g} + \eta\Delta\mathbf{v}_n, \tag{2}$$

where ρ_s and ρ_n are, respectively, superfluid and normal densities ($\rho = \rho_s + \rho_n$ being the total density); ρ is the pressure; $\mathbf{g}$ is the free fall acceleration; and η is the viscosity.

The solution to Eqs. (1, 2), satisfying the constraint $\mathrm{curl}\mathbf{v}_s = 0$ and corresponding to a small-amplitude surface wave with frequency ω and wavevector $\mathbf{q}$ parallel to the surface (we assume that, in equilibrium, the liquid is situated at $z < 0$) can be chosen in the form

$$\mathbf{v}_s^{\parallel}(\mathbf{r}, t) = \mathbf{v}_s^0 + i\mathbf{q}\gamma e^{qz}A, \tag{3}$$

$$v_s^z(\mathbf{r}, t) = q\gamma e^{qz}A, \tag{4}$$

$$\mathbf{v}_n^{\parallel}(\mathbf{r}, t) = \mathbf{v}_n^0 + i\mathbf{q}\gamma(e^{qz}B + e^{kz}C), \tag{5}$$

$$v_n^z(\mathbf{r}, t) = \gamma[qe^{qz}B + (q^2/k)e^{kz}C], \tag{6}$$

$$p(\mathbf{r}, t) = -\rho gz + i\gamma e^{qz}[\rho_s(\omega - \mathbf{v}_s^0\mathbf{q})A + \rho_n(\omega - \mathbf{v}_n^0\mathbf{q})B], \tag{7}$$

where superscript $\parallel$ refers to the component of a vector parallel to the surface; $\gamma \equiv \exp i(\mathbf{qr} - \omega\mathbf{t})$;

$$k = \sqrt{q^2 - i\frac{\rho_n}{\eta}(\omega - \mathbf{v}_n^0\mathbf{q})}, \quad \mathrm{Re}k > 0; \tag{8}$$

A, B, and C are (arbitrary) constants; and the possibility of an equilibrium counterflow (characterized by $\mathbf{v}_s^0 \neq \mathbf{v}_n^0$) is taken into account.

Substitution of Eqs. (3–7) into the boundary conditions describing the conservation of mass and entropy,

$$v_s^z - (\mathbf{v}_s^{\parallel}\nabla^{\parallel})\zeta = v_n^z - (\mathbf{v}_n^{\parallel}\nabla^{\parallel})\zeta = \frac{\partial\zeta}{\partial t}, \tag{9}$$

and mechanical equilibrium,

$$\eta(\nabla^z\mathbf{v}_n^{\parallel} + \nabla^{\parallel}v_n^z) = 0, \tag{10}$$

$$-p + 2\eta\nabla^z v_n^z = \sigma(\nabla^{\parallel})^2\zeta, \tag{11}$$

at the surface (whose deviation from the plane $z = 0$ is denoted by ζ and surface tension by σ) shows that they are compatible with each other for

$$\rho_s(\omega - \mathbf{v}_s^0\mathbf{q})^2 + \rho_n\left(\omega - \mathbf{v}_n^0\mathbf{q} + i\frac{2\eta q^2}{\rho_n}\right)^2 + \frac{4\eta^2 q^3 k}{\rho_n} = \rho gq + \sigma q^3. \tag{12}$$

The derivation of Eq. (12) does not require the assumption that viscosity is small, so it is applicable for an arbitrary value of viscosity.

3. INSTABILITY THRESHOLDS FOR ZERO AND FINITE VISCOSITY

For $\rho_s = 0$ and $\sigma = 0$, Eq. (12) is transformed to the dispersion relation of a gravitational wave on the free surface of a normal liquid [11], whereas, in the limit of $\eta = 0$, it is reduced to the equation

$$(\omega - \mathbf{vq})^2 = gq + \frac{\sigma}{\rho}q^3 - \frac{\rho_n\rho_s}{\rho^2}(\mathbf{wq})^2 \tag{13}$$

describing the spectrum of surface waves in a superfluid with the counterflow [2] derived in the framework of the nondissipative two-fluid description. Here, $\mathbf{v} = (\rho_s\mathbf{v}_s^0 + \rho_n\mathbf{v}_n^0)/\rho$ is the mass velocity and $\mathbf{w} = \mathbf{v}_n^0 + \mathbf{v}_s^0$ is the relative velocity in the superfluid. The form of Eq. (13) shows that the roots with positive and negative imaginary parts (the former correspond to growing corrugation) exist only if the right-hand side can be negative, that is, if the absolute value of $\mathbf{w}$ exceeds w_{c0} defined by

$$w_{c0}^2 = \frac{2(\rho^3 g\sigma)^{1/2}}{\rho_n\rho_s}, \tag{14}$$

with the instability taking place at $\mathbf{q} = \pm(\mathbf{w}/w)q_c$, where $q_c^2 = \rho g/\sigma$.

On the other hand, for any finite $\eta > 0$, one of the roots of Eq. (12) crosses the real axis already when

$$S(\mathbf{q}) \equiv gq + \frac{\sigma}{\rho}q^3 - \frac{\rho_s}{\rho}(\mathbf{wq})^2 \tag{15}$$

touches zero, that is, at

$$|\mathbf{w}| = w_c \equiv \left[\frac{2(\rho g\sigma)^{1/2}}{\rho_s}\right]^{1/2} = \left(\frac{\rho_n}{\rho}\right)^{1/2} w_{c0}, \tag{16}$$

with the instability appearing at the value of relative velocity *lower* than in the absence of dissipation, although at the same value of q. Note that, in the limit of zero temperature (when $\rho_s \longrightarrow \rho$), the criterion (16) coincides with the Landau criterion for the creation of ripplons in the reference frame of container walls.

For $S(\mathbf{q})$ sufficiently close to zero, the value of the root crossing the real axis is given by

$$\omega(\mathbf{q}) - \mathbf{v}_n^0\mathbf{q} \approx \frac{1}{2}\frac{\rho S(\mathbf{q})}{\rho_s \mathbf{w}\mathbf{q} + i\eta q^2}. \quad (17)$$

This shows that, for small viscosity and $\mathbf{w}$ just above w_c, the rate of instability development decreases with decreasing η, contrary to what is naturally expected.

By looking where the free energy of a corrugation, calculated in the reference frame of the normal component, is no longer positively defined (such an approach can be considered as a macroscopic generalization of the Landau criterion), the threshold for the instability of the interface between two different superfluids was found in [9] to be

$$\rho_{s1}(\mathbf{v}_{s1}^0 - \mathbf{v}_n^0)^2 + \rho_{s2}(\mathbf{v}_{s2}^0 - \mathbf{v}_n^0)^2 = 2(F\sigma)^{1/2}, \quad (18)$$

where F is a generalized restoring force, whose role in the case of a free surface is played by ρg. In the limit where the density of one of the liquids goes to zero, Eq. (18) is reduced to our criterion (16) obtained for the free surface of a single superfluid liquid.

4. CONCLUSION

In this work, we have investigated the dynamic instability of the free surface of a superfluid liquid caused by the relative motion of superfluid and normal components along the surface. The value of the instability threshold for finite viscosity, given by Eq. (16), is found to be independent of viscosity, but lower than in the absence of dissipation. The same criterion can be obtained by looking for the thermodynamic instability in the reference frame of the normal component.

An analogous modification of the instability threshold was found [9] to take place at the interface between two superfluids in the presence of friction with respect to the reference frame related to container walls,[2] which leads to violation of the Galilean invariance. Note that in our problem the same phenomenon appears in the situation where the form of dissipation does not imply the explicit selection of a particular reference frame. Nonetheless, the presence of dissipation (a finite value of viscosity) turns out to be sufficient to produce the same criterion for surface instability as in the case where the form of friction leads to the direct violation of the Galilean invariance.

The first experimental observation of the Kelvin–Helmholtz instability at the interface between ^{3}He-A and ^{3}He-B by Blaauwgeers *et al.* [10] unambiguosly demonstrated that it does indeed take place not for the classical, but for the modified value of the threshold. According to our results, the same can be expected from the instability on the free surface of superfluid ^{4}He.

I am grateful to G.E. Volovik for useful discussions. This work was supported by the program "Quantum Macrophysics" of the Russian Academy of Sciences, the program "Scientific Schools of the Russian Federation" (grant no. 00-15-96747), the Swiss National Science Foundation, and the Netherlands Organization for Scientific Research (NWO) in the framework of the Russian–Dutch Cooperation Program.

[2] The same type of dissipation was taken into account by Kagan [4] when studying the instability of the quantum interface between superfluid and solid ^{4}He.

REFERENCES

1. L. D. Landau and E. M. Lifshitz, *Course of Theoretical Physics*, Vol. 6: *Fluid Mechanics* (Nauka, Moscow, 1986; Pergamon, New York, 1989), Sec. 62, Problem 3.
2. S. E. Korshunov, Europhys. Lett. **16**, 673 (1991).
3. P. W. Egolf, J. L. Olsen, B. Roericht, and D. A. Weiss, Physica B (Amsterdam) **169**, 217 (1991).
4. M. Yu. Kagan, Zh. Éksp. Teor. Fiz. **90**, 498 (1986) [Sov. Phys. JETP **63**, 288 (1986)].
5. A. F. Andreev and A. Ya. Parshin, Zh. Éksp. Teor. Fiz. **75**, 1511 (1978) [Sov. Phys. JETP **48**, 763 (1978)].
6. K. O. Keshishev, A. Ya. Parshin, and A. V. Babkin, Pis'ma Zh. Éksp. Teor. Fiz. **30**, 63 (1979) [JETP Lett. **30**, 56 (1979)]; Zh. Éksp. Teor. Fiz. **80**, 716 (1981) [Sov. Phys. JETP **53**, 362 (1981)].
7. K. W. Madison, F. Chevy, V. Bretin, and J. Dalibard, Phys. Rev. Lett. **86**, 4443 (2001).
8. S. Sinha and Y. Castin, Phys. Rev. Lett. **87**, 190402 (2001).
9. G. E. Volovik, Pis'ma Zh. Éksp. Teor. Fiz. **75** (8), 491 (2002) [JETP Lett. **75**, 418 (2002)].
10. R. Blaauwgeers, V. B. Eltsov, G. Eska, *et al.*, cond-mat/0111343 (2001).
11. L. D. Landau and E. M. Lifshitz, *Course of Theoretical Physics*, Vol. 6: *Fluid Mechanics* (Nauka, Moscow, 1986; Pergamon, New York, 1989), Sec. 25, Problem 1.
12. L. D. Landau and E. M. Lifshitz, *Course of Theoretical Physics*, Vol. 6: *Fluid Mechanics* (Nauka, Moscow, 1986; Pergamon, New York, 1989), Sec. 140, Problem 1.

JETP Letters, Vol. 75, No. 8, 2002, pp. 426–431. Translated from Pis'ma v Zhurnal Éksperimental'noĭ i Teoreticheskoĭ Fiziki, Vol. 75, No. 8, 2002, pp. 499–504.

Problem of a Billiard in Symmetric Coordinates

S. V. Naydenov[1]*, V. V. Yanovsky[1], and A. V. Tur[2]

[1] *Institute of Single Crystals, National Academy of Sciences of Ukraine, Kharkov, 61001 Ukraine*

[2] *Centre d'Etude Spatiale Des Rayonnements, C.N.R.S.-U.P.S., 31028 Toulouse, CEDEX 4, France*

**e-mail: naydenov@isc.kharkov.com*

Received November 12, 2001; in final form, February 19, 2002

Billiards are an important geometric model in nonlinear physics. A dynamical description of a billiard in symmetric coordinates is proposed. The topological structure of a symmetric phase space and geometric criteria for the stochasticity of billiard systems are determined. © *2002 MAIK "Nauka/Interperiodica".*

PACS numbers: 05.45.Ac; 05.45.Mt; 45.20.Jj

Billiards are a simple but important physical model. They were used to justify the hypothesis for molecular chaos in statistical physics [1], to demonstrate ergodicity and mixing in dynamical systems with a few degrees of freedom in chaotic dynamics [2–5], and to develop the (semiclassical) correspondence principle in postmodern quantum mechanics [6, 7]. Practical applications of billiards [8–10] are important for the physics of resonators, wave guides, traps, detectors, etc.

A billiard has geometric nature. In the classical formulation, it corresponds to the free motion (with unit velocity $v = |\mathbf{v}| = 1$) of a pointlike particle inside the region Ω with elastic reflection from its boundary $\partial\Omega$. The geometry of $\partial\Omega$ determines a variety of dynamical regimes of a billiard, i.e., the behavior of its trajectories. Mixed regular and chaotic dynamics is typical. Among dynamical systems, the billiard has become a paradigm of determinated chaos [11]. Most problems that are reduced to billiards require a description of trajectory dynamics. Geometric trajectories intersect each other inside Ω and can be highly intricate. For this reason, the description is usually carried out in a phase space with nonintersecting trajectories. In this case, a billiard is traditionally associated with the conservative mapping [12] obtained by cross sectioning the initial flux [13] at the moments of sequential reflections from the boundary $\partial\Omega$. The phase state of this Hamiltonian system is specified by a pair of canonical variables: coordinate and momentum. These are usually local Birkhoff coordinates—the natural parameter l at $\partial\Omega$ [14] and the angle of incidence θ at the reflection point.

In this paper, a billiard is described in more equivalent (symmetric), though nonlocal, coordinates, which determine a new *symmetric* phase space Σ. The symmetric coordinates have a projective nature, and an arbitrary billiard in these coordinates reduces from the outset to a discrete dynamical system—the mapping of a special form. In this case, no auxiliary (with singularities) Poincaré sections for the billiard flux are required. The topology of Σ is closely related to the geometry of $\partial\Omega$, which directly influences the billiard stochasticity.

Let us construct a symmetric phase space Σ. For this purpose, we will not explicitly track the dynamics of geometric trajectories between their sequential collisions with the boundary $\partial\Omega$. When introducing the space Σ, the particular form of trajectories (not necessarily rectilinear rays if the motion occurs on the curvilinear surfaces or in an external field) between reflections is immaterial. The dynamics of a billiard is generally determined only by the initial state and the sequence of reflections from $\partial\Omega$. The state of the system will be specified by a pair of coordinates, s_1 and s_2, of sequential reflections at the points $\mathbf{r}(s_1)$ and $\mathbf{r}(s_2)$, where $\mathbf{r}(s) = \mathbf{r}|_{\partial\Omega}$ is a certain boundary parametrization [14] and $s \in M$. The manifold M is determined by the topology of $\partial\Omega$. For a one-dimensional, closed, simply connected boundary, $M = S^1$ (circle). Geometrically, a phase point $\mathbf{s}$ is identified with an individual segment (ray) of the billiard trajectory:

$$\mathbf{s} = (s_1, s_2) \in \Sigma = M \times M; \quad M \sim \partial\Omega. \qquad (1)$$

For the planar billiard, this is a ray between reflections. A passage from points (reflections) to rays (incident and reflected) is the projective duality operation that is useful in applications [15]. The topology of Σ for a two-dimensional billiard is the topology of a torus $T^2 = S^1 \times S^1$ (there is no edge; i.e., $\partial T^2 = \varnothing$). In terms of Birkhoff coordinates, the phase space is the lateral area of a cylinder $\Pi = S^1 \times [-\pi/2, \pi/2]$ (with edge $\theta = \pm\pi/2$). For a convex multidimensional billiard, $\Sigma = S^n \times S^n$, etc. In terms of new coordinates, a state is determined nonlocally, because it is related not to one point but to different points of reflection. It is this nonlocality that allows the symmetrization of the description of the billiard.

The motion along each billiard trajectory is possible in opposite directions (time reversibility). For this rea-

son, regardless of the direction of an arbitrary ray with either the coordinates $\mathbf{s}^t = (s_1, s_2)$ or the transposed coordinates $\mathbf{s}^{-t} = (s_2, s_1)$, the direct (and reverse) reflections provide the same billiard trajectory. Therefore, the introduced coordinates are symmetric. Along with the phase trajectory with the initial point (s_{10}, s_{20}), the symmetric trajectory with the initial point (s_{20}, s_{10}) is present in Σ. For this reason, arbitrary functions in Σ are symmetric, including the indicators $\chi_U(\mathbf{s})$ $(U \subset \Sigma)$ describing bundles of trajectories and densities of any measure μ:

$$\chi_U(s_1, s_2) = \chi_U(s_2, s_1); \quad \mu(s_1, s_2) = \mu(s_2, s_1). \quad (2)$$

The phase-space diagonal $\Delta = \{(s_1, s_2) \in \Sigma | s_1 = s_2\}$ is a line of symmetry. Symmetry (2) means that the billiard, as a dynamical system in Σ, belongs to reversible systems generalizing Hamiltonian systems [16]. The description of a billiard in symmetric coordinates becomes covariant. The dynamics remains invariant for any geometric changes $s' = z(s)$ of coordinate systems or for any reparametrization of $\partial\Omega$, because they apply to both variables s_1 and s_2 of the symmetric phase space.

Let us construct a dynamical system corresponding to the billiard in the symmetric coordinates. The incident ray with the coordinates (s_1, s_2) converts to the reflected ray $(\bar{s}_1, \bar{s}_2)$, and the reflection point s_2 converts to the exit point, $\bar{s}_1 = s_2$. The point $\bar{s}_2 = f(s_1, s_2)$ is determined by the reflection law. This is usually the law of elastic (mirror) reflection. The angle of reflection is equal to the angle of incidence, or $\bar{\theta} = \pi - \theta$ for oriented angles. There is also an anomalous law, when the sign of the total momentum, rather than that of only its normal component, changes. After the reflection, a particle becomes an antiparticle. This is the Andreev reflection [17]. In this case, $\bar{s}_2 = f_A(s_1, s_2) = s_1$. Below, billiards of both convenient and Andreev [18] types will be analyzed. For the Andreev reflection of massive particles (superconducting electrons), a macroscopic condensate acts as a physical vacuum creating particle–antiparticle pairs. The anomalous reflection of photons can be realized using the nonlinear effect of phase conjunction [19]. The sequential reflections $(s_1, s_2) \longrightarrow (\bar{s}_1, \bar{s}_2) \longrightarrow \ldots$ correspond to the iterations of *billiard* mapping:

$$B := \{\bar{s}_1 = s_2; \bar{s}_2 = f(s_1, s_2)\}. \quad (3)$$

Phase trajectories in Σ correspond to geometric trajectories upon the natural projection $\Sigma \longrightarrow \partial\Omega$. Each physical image (ray, trajectory, bundle, etc.) corresponds to a certain element in Σ (phase point, orbit, domain, or curve). The chaos dynamics and the statistical properties of billiards obey the features of a special class of *billiard mappings* (3). These features are associated with the properties of the function f.

A repeated reflection of the initially reflected ray returns us to the initial ray. Hence, the equality $f(f(s_1, s_2), s_2) = s_1$ must be satisfied. This property will be referred to as *billiard involution*; i.e., $f \circ f = id$ (id is the identity function), where f is a one-parametric (depending on the reflection point) family, $f(s_1, s_2) = f_{s_2}(s_1)$. If the motion occurs in a magnetic field or any other solenoidal field with $\mathbf{H}^*(t) \equiv \mathbf{H}(-t) \neq \mathbf{H}(t)$, the reversibility is restored under the more general condition

$$\begin{aligned} &f(f(s_1, s_2; \mathbf{H}), s_2; \mathbf{H}^*) \\ &= s_1 \longleftrightarrow f(H^*) \circ f(H) = id. \end{aligned} \quad (4)$$

In a potential field, the velocity of a particle changes and f depends on time t. The property of involution is

$$f(f(s_1, t_1; s_2, t_2), t_2 + \tau^*; s_2, t_1 + \tau) = s_1, \quad (5)$$

where

$$\tau = t_2 - t_1 = \int_{s_1}^{s_2} \frac{d\mathbf{r}}{v(\mathbf{r})} \text{ and } \tau^* = \int_{s_2}^{f} \frac{d\mathbf{r}}{v(\mathbf{r})}.$$

In particular, the motion remains rectilinear for *breathers*, i.e., billiards with the perturbed boundary $\partial\Omega = \partial\Omega(t)$ [11, 20]. For them,

$$\tau = \frac{|\mathbf{r}(s_1) - \mathbf{r}(s_2)|}{v(s_1)}; \quad \tau^* = \frac{|\mathbf{r}(f) - \mathbf{r}(s_2)|}{v(s_2)},$$

where $\mathbf{r}(s_1) = \mathbf{r}(t - \tau)$, $\mathbf{r}(s_2) = \mathbf{r}(t)$, $\mathbf{r}(f) = \mathbf{r}(t + \tau^*)$, $v(s_1) = v(t^- - \tau)$, and $v(s_2) = v(t^-)$. The "quivering" of the boundary $\mathbf{r}(t)$ is specified, and the velocity $v(t^-)$ (here, $t^- = t - 0$) of a ray at the time instant before reflection is known. Inverting the expressions for τ and τ^* by applying the implicit function theorem, we obtain the local dependences $t_2 = t(\tau)$ and $\tau^* = \varphi(t_2) = \tau^*(\tau)$. As a result, the breather involution depends only on the shift τ (time between collisions); i.e., $f(s_1, t_1; s_2, t_2) = f(s_1, s_2; \tau)$. This is a billiard with "retardation."

The particular form of f is determined by the shape of $\partial\Omega$ and the character of motion in Ω. The condition for elastic reflection $\cot\theta = -\cot\bar{\theta}$ in the Cartesian coordinates $\mathbf{r} = (x, y)$ and $n|_{\partial\Omega} = (n_x, n_y)$ (normal) gives

$$\xi(f, s_2) = R(\xi(s_1, s_2), s_2) = \frac{a(s)\xi + b(s)}{b(s)\xi - a(s)}, \quad (6)$$

where

$$\xi(s_1, s_2) = \frac{x(s_1) - x(s_2)}{y(s_1) - y(s_2)},$$

R is the rational projection transformation, $a(s) = n_x^2(s) - n_y^2(s)$, and $b(s) = 2n_x(s)n_y(s)$. Examples of such

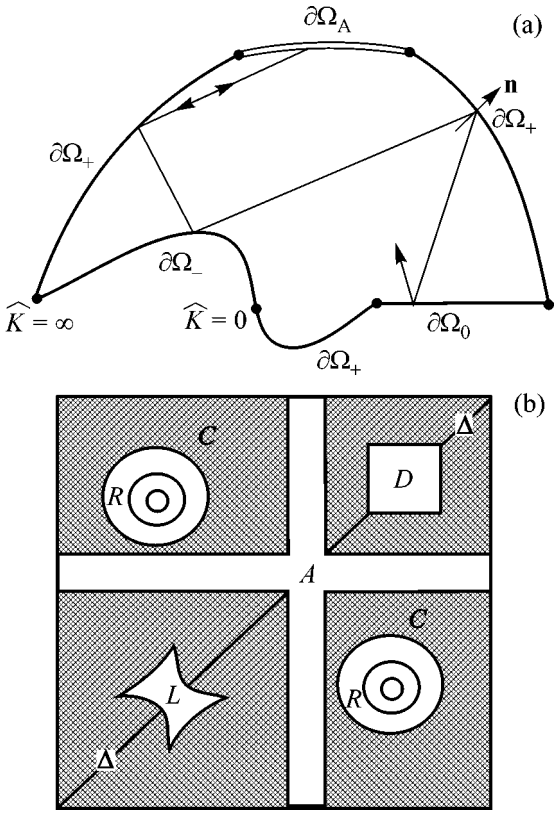

(a) Geometry of a typical billiard with a boundary containing convex, concave, rectilinear, and Andreev sections. (b) Qualitative structure of the symmetric phase space of a planar billiard presented in (a); C and R are the chaotic and regular domains, respectively; Δ is the diagonal; L is lacuna; D is the discriminant; and A is the Andreev domain. The structure is shown in the flat $I \times I$ development of a torus $\Sigma = T^2$.

involutions were obtained in [21]. They can be used to describe the dynamics of particular billiards.

It follows from Eq. (6) that the variables can be changed so that the involution becomes rational in new coordinates. Geometrically, this means that the billiard is reducible to the local projective transformations. The projectivity of involution follows from the geometric nature of a billiard.

In the symmetric coordinates, the phase-space structure most completely reflects the features of billiard geometry. The basic elements of this structure are regular R and chaotic C components and singularities P: diagonal Δ, lacunas L, discriminants D, and Andreev domains A:

$$\Sigma = \Sigma_R \oplus \Sigma_C \oplus \Sigma_P; \quad \Sigma_P = \Delta \oplus L \oplus D \oplus A. \quad (7)$$

This structure corresponds to the billiard with a typical boundary (figure). In the regular domains $\Sigma_R \subset \Sigma$, a quasiperiodic motion occurs on the invariant tori [15] or, for a planar billiard, on the invariant closed curves. In the chaotic domain Σ_C, the exponentially unstable (with respect to the perturbations of initial conditions) phase trajectories mix and the motion is ergodic. The singularities as topological obstacles separate the phase flux. The diagonal Δ contains all fixed points of billiard mapping (3), $\Delta \supseteq \mathrm{Fix}(B)$. This follows from the property $f(s, s) = s$, which means that the incident and reflected rays coincide for the tangential propagation along $\partial\Omega$. It is evident that the tangential rays cannot propagate inside Ω. The diagonal separates symmetric phase trajectories corresponding to the motions in opposite directions.

Inside the Andreev domains A, the symmetric trajectories match with each other (at the points symmetric about Δ) and the time-reversed trajectories are localized. Topologically, matching means the gluing of certain phase-space regions and is not a continuous rearrangement. This corresponds to the appearance of a gap in the excitation spectrum. In addition, the Andreev domains can be superimposed on the other components of Σ and change their topology. In particular, the intersection of A and Σ_R gives rise to a discontinuity in a regular quasiperiodic curve, because the anomalous reflection domain cannot contain more than two points of reflection for the same billiard trajectory. The symmetric phase space is particularly suitable for the description of mixed-type Andreev billiards with ordinary and anomalous reflections (figure). Whereas the orientation is conserved for the ordinary reflection [Jacobian $J(\mathbf{s}) = -f'_{s_1}(s_1, s_2)$ of mapping (3) with involution (6) is positive, $J_N > 0$], it changes for the Andreev reflection ($J_A = -1$). In the Hamiltonian coordinates, $J_{N,A} = \pm 1$. Canonical transformations must conserve the Jacobian. Therefore, the reflection must be of the same type everywhere. In the symmetric approach, only the reversibility is required, whereas the Jacobian may change, and the description will be adequate for a billiard of an arbitrary type.

Lacunas correspond to the domains of geometric shadow. These are the domains of classically forbidden rays specified by their points of intersection with $\partial\Omega$ but situated outside of Ω. Lacunas appear in billiards with the concave boundary $\partial\Omega_-$ (figure) or cusps (the tangential rays pass inside Ω). For billiards with curvature, these are the domains with oriented curvature $\hat{K} < 0$ [14] (for the outer normal) or singularities with $\hat{K} = -\infty$. Discriminants are the degeneracy domains. They are filled with "adhering" rays lying entirely or partially in the rectilinear sections of $\partial\Omega_0$ with zero curvature $\hat{K} = 0$ and with the rays falling into the corner points (tangents are outside the Ω), where $\hat{K} = +\infty$. The further propagation of such rays is indefinite and their dynamics is considered interrupted. The phase measure of the rays ending at the isolated singularities of $\partial\Omega$ is zero. The measures of lacunas and discriminants are,

respectively, $\mu(L) \propto |\partial\Omega_-|^2$ and $\mu(D) \propto |\partial\Omega_0|^2$ ($|\partial\Omega|$ is the length of a curve). The number of lacunas is equal to the total number of concave components and cusps, and the number of discriminants is equal to the number of rectangular sections and corner points. The boundaries of singular domains are determined from the following geometric equations for the points $(s_1, s_2) \in \Sigma$:

$$\partial L := \begin{cases} (\mathbf{r}(s_1) - \mathbf{r}(s_3), \mathbf{n}(s_3)) = 0 \\ (\mathbf{r}(s_2) - \mathbf{r}(s_3), \mathbf{n}(s_3)) = 0; \end{cases} \quad \hat{K}(s_3) < 0; \tag{8}$$

$$\partial D := (\mathbf{r}(s_1) - \mathbf{r}(s_2), \mathbf{n}(s_3)) = 0; \quad \hat{K}(s_3) = 0; \tag{9}$$

$$\partial A := \mathbf{r}(s_2) \in \partial\Omega_a; \quad \mathbf{r}(s_1) - \mathbf{r}(s_2) \in \Omega, \tag{10}$$

where $(\cdot, \cdot)$ is the scalar product. Conditions (8) and (9) determine the bundles of rays tangential to $\partial\Omega_-$ and $\partial\Omega_0$, respectively. Setting $\mu(\Sigma) = 1$, we obtain $\mu(\Sigma_P) = 1 - \mu(\Sigma_R) - \mu(\Sigma_C)$. The phase-space volume of the components can be calculated in the Euclidean metric on the development $I \times I$ of the torus (figure). The boundaries of lacunas (8) and discriminants (9) are determined strictly geometrically. Therefore, their phase dimension $\mu_{L,D}$ depends only on the shape of $\partial\Omega$ and does not change upon the uniform inflation of a billiard.

We emphasize that the lacunas and discriminants are the attributes of a symmetric phase space. These elements are indistinguishable and absent in the phase space with Birkhoff-type coordinates. The nonlocal elements not involved in the Hamiltonian dynamics (rays in the shadow domain or those with an indefinite evolution) are projected onto the edge of an asymmetric phase space (onto the bases of a cylinder $\partial\Omega$ in the case of a 2D billiard) and prove to be "invisible." In Σ, the projectivity of the billiard restores their equivalence. The corresponding L and D domains appear together with the destruction of a portion of the diagonal Δ to change explicitly the topology of Σ (after gluing, "holes" appeared with the sheets of the projective plane). Thus, the singularities hidden for the classical Birkhoff or related coordinates become resolved in the symmetric approach. The appearance of these singularities is closely related to the chaotic properties of billiards.

Singularities variously influence the chaotic properties of a billiard. These properties can be analyzed using the general concepts of chaotic dynamics of the dynamical systems and mappings (see, e.g., [5, 6, 12, 13]), including billiards. The Andreev domains suppress chaos. The appearance of lacunas leads to the destruction of "whispering-gallery" trajectories (near Δ) and to the appearance of chaos. An increase in the size of L enhances chaos, because the number of hyperbolic periodic trajectories involving the points of $\partial\Omega_-$ increases. This is also evident from the physical point of view, because the collisions of chaotic trajectories with $\partial\Omega_-$, where they disperse, become more frequent as the size of the geometric shadow increases.

It is natural to suggest the following geometric criterion for chaos. (i) The Lyapunov exponent in the phase space of a billiard is positive for any nonzero measure of lacunas. (ii) As the sizes of lacunas change, the Lyapunov exponent changes monotonically upon increasing their phase-space volume:

$$\mu_L > 0 \longrightarrow \lambda_B > 0; \quad \frac{d\lambda_B}{d\mu_L} > 0, \tag{11}$$

where λ_B is the Lyapunov exponent [6]. In billiards, which are measure-conserving mappings, this exponent is always nonnegative (or zero in the integrable billiards). Criterion (11) is consistent with the condition [4] for the stochasticity of a billiard formed by circle arcs: the complement of each arc with respect to the complete circle must lie inside Ω. This condition means that the arc junctions are cusps and, therefore, they generate lacunas in Σ. The disappearing lacunas are replaced by regular trajectories. It should be emphasized that criterion (11) relates the positiveness of the lacuna measure to the positiveness of the Lyapunov exponent outside the lacunas, i.e., in the remaining part of the phase space accessible to dynamics. It is important that, when applying this criterion, one can estimate not only the presence of the corresponding billiard but also the degree of its stochasticity. Moreover, this criterion holds true for billiards of higher dimensionalities.

Note that the chaotic component can also exist in an everywhere convex billiard, for which lacunas are absent, $\mu(L) = 0$. Another feature of such a billiard is that it has regular phase trajectories passing near and along the diagonal Δ of the symmetric phase space. These trajectories correspond to the whispering-gallery trajectories in the geometric space. The trajectories of this type are most pronounced for the billiard in a circle, where they fill the whole symmetric phase space and fiber it into the multitude of invariant curves parallel to the diagonal Δ. The billiard in a circle is the degenerate case (all periodic trajectories have neutral stability). It is worth noting that the appearance of lacunas destroys all whispering-gallery trajectories.

Whereas the appearance of lacunas always induces chaos, the increase of discriminants variously changes it. In particular, the Lyapunov exponent of a "stadium" increases ($l < d$) or decreases ($l > d$) through extending its rectilinear sides ($\partial\Omega$ is the circle diameter) [3]. Randomization occurs upon "scattering" by the curvilinear components of $\partial\Omega$. The rectilinear segments do not scatter parallel rays but enhance spreading (focusing) of already scattered (focused) rays, thus playing the role of instability "amplifiers." Discriminants are phase images of these segments. As D increases, the defocusing on convex boundary $\partial\Omega_+$ should increase. However,

the increase in μ_D picks up a part of the accessible phase space. This retards the randomization. As a consequence, the following criteria can be formulated, respectively, for the enhancement (attenuation), "drop," and "saturation" of stochasticity:

$$\frac{d\lambda_B}{d\mu_D} \gtrless 0; \quad \lim_{\mu_D \to 0}\left|\frac{d\lambda_B}{d\mu_D}\right| = \infty; \quad \lim_{\mu_D \to \mu_D^*}\frac{d\lambda_B}{d\mu_D} = 0. \quad (12)$$

In the condition for saturation, $\mu_D^* = \sum_i l_i^2/(\sum_i l_i)^2$ is the limiting size of discriminants at $|\partial\Omega| \longrightarrow \sum_i l_i$ for the billiard boundary $\partial\Omega$ including rectilinear components with length l_i.

A jumpwise change of stochastic properties with the appearance of discriminants occurs, e.g., upon passing from the billiard in a circle ($l = 0$ and $\mu_D = 0$) to a stadium ($\mu_D = 2l^2$). Using the expressions from [22] for the Kolmogorov–Sinai entropy, H_{KS}, coinciding with the Lyapunov exponent averaged over the phase space, $H_{KS} \approx \langle\lambda_B\rangle_\Sigma$, we arrive at the relationships $\partial\lambda_{stad}/(\partial\mu_D) \approx \text{const}\ \mu_D^{-3/4} > 0$ for $l \ll d$ and $\partial\lambda_{stad}/(\partial\mu_D) \approx -1/\sqrt{2\mu_D}((1 - 2\mu_D)/2\pi)\ln 2\pi(1 - 2\mu) < 0$ for $d \ll l$. As $\mu_D \longrightarrow 0$, one has $\partial\lambda_{stad}/(\partial\mu_D) \longrightarrow +\infty$. The saturation of the instability exponent corresponds to the rectification of the boundary, $\partial\Omega \longrightarrow \partial\Omega_0$, upon extending $l \gg d$, when $\mu_D^* = 1/2$ and $\partial\lambda_{stad}/(\partial\mu_D) \longrightarrow 0$. This example clearly demonstrates the validity of general relationships (12).

Note that, as the relative fraction of scattering $\partial\Omega_-$ and neutral $\partial\Omega_0$ boundary components increases, the rates of filling the phase space Σ with lacunas and discriminants are different. One can easily verify that the discriminants are symmetric along and across the diagonal Δ and always shaped like squares in the torus development (figure). They increase quadratically: $\mu_D = \sum_i |(\partial\Omega_0)_i|^2$, whereas lacunas ($\hat{K} < 0$) extend exponentially $\sim\exp[\ln(1 - \hat{K})]$ transverse to Δ with an increase in $|\partial\Omega_-|/|\partial\Omega|$. This is due to the scattering character of the concave components. The exponential decoupling of the correlations upon their power-law decrease in negative-curvature defocusing billiards can also be assigned to this difference. With a change in D, the transition to a completely regular dynamics is possible for some $\partial\Omega$ (e.g., when a billiard inside the segment of a circle attains half the circle). The monotonicity $d\lambda_B/d\mu_L > 0$ or $d\lambda_B/d\mu_D \gtrless 0$ can be found numerically and analytically for various billiard families. The usefulness of utilizing this information is enhanced by the possibility of geometrically calculating the shape and sizes of lacunas and discriminants from the shape of the billiard boundary, i.e., in fact, without using the dynamic properties of trajectories.

Thus, the topological structure of the symmetric phase space of a billiard directly influences its stochasticity. All 2D billiards of different types can be topologically classified. They are equivalent to the compact orientable and nonorientable 2D manifolds. The character of the dynamics depends on this topology. It is also possible to show that the kinetic symmetric description of a billiard (invariant distributions) is directly determined by the dynamics (involution). The commutativity of observables corresponding to the symmetric phase variables (in contrast to the noncommutative momentum and coordinate operators) provides new possibilities of describing quantum chaos in billiard systems. For this reason, the choice of symmetric coordinates introduces important physical meaning to the theory. This approach can be naturally generalized to the multidimensional and curvilinear geometry.

We are grateful to Academicians V.G. Bar'yakhtar and S.V. Peletminskiĭ for stimulating discussions and valuable remarks, and to the referee for valuable comments, which enabled us to improve the manuscript.

REFERENCES

1. N. S. Krylov, *Works on the Foundation of Statistical Physics* (Akad. Nauk SSSR, Moscow, 1950).
2. Ya. G. Sinaĭ, Dokl. Akad. Nauk SSSR **153**, 1261 (1963); Usp. Mat. Nauk **25**, 141 (1970).
3. G. Benettin and J. M. Strelcyn, Phys. Rev. A **17**, 773 (1978).
4. L. A. Bunimovich, Zh. Éksp. Teor. Fiz. **89**, 1452 (1985) [Sov. Phys. JETP **62**, 842 (1985)]; Chaos **1**, 187 (1991).
5. R. Z. Sagdeev, D. A. Usikov, and G. M. Zaslavsky, *Nonlinear Physics: from the Pendulum to Turbulence and Chaos* (Nauka, Moscow, 1988; Harwood, Chur, 1988).
6. H. G. Schuster, *Deterministic Chaos* (Physik-Verlag, Weinheim, 1984; Mir, Moscow, 1988).
7. T. Guhr, A. Muller-Groeling, and H. A. Weidenmuller, Phys. Rep. **299**, 189 (1998).
8. C. Ellegaard, T. Ghur, K. Lindemann, *et al.*, Phys. Rev. Lett. **75**, 1546 (1995).
9. H. Alt, H. D. Graf, R. Hofferbert, *et al.*, Phys. Rev. E **54**, 2303 (1996).
10. J. U. Nocel and A. D. Stone, Nature **385**, 45 (1997).
11. *Proceedings of the International Conference on Classical and Quantum Billiards*, J. Stat. Phys. **83**, 1 (1996).
12. G. D. Birkhoff, *Dynamical Systems* (American Mathematical Society, New York, 1927; Izd. "Udmurtskiĭ Universitet", Izhevsk, 1999).
13. I. P. Kornfel'd, Ya. G. Sinaĭ, and S. I. Fomin, *Ergodic Theory* (Nauka, Moscow, 1980).

14. B. A. Dubrovin, A. T. Fomenko, and S. P. Novikov, *Modern Geometry—Methods and Applications* (Nauka, Moscow, 1986; Springer-Verlag, New York, 1984).
15. V. I. Arnold, *Mathematical Methods of Classical Mechanics* (Nauka, Moscow, 1974; Springer-Verlag, New York, 1989).
16. J. A. G. Roberts and G. R. W. Qwispel, Phys. Rep. **216**, 177 (1992).
17. A. F. Andreev, Zh. Éksp. Teor. Fiz. **46**, 1823 (1964) [Sov. Phys. JETP **19**, 1228 (1964)].
18. I. Kosztin, D. L. Maslov, and P. M. Goldbart, Phys. Rev. Lett. **75**, 1735 (1995).
19. B. I. Stepanov, E. V. Ivakin, and A. S. Rubanov, Dokl. Akad. Nauk SSSR **196**, 567 (1971) [Sov. Phys. Dokl. **16**, 46 (1971)].
20. A. Yu. Loskutov, A. B. Ryabov, and L. G. Akinshin, Zh. Éksp. Teor. Fiz. **116**, 1781 (1999) [JETP **89**, 966 (1999)].
21. S. V. Naydenov and V. V. Yanovsky, Teor. Mat. Fiz. **126**, 110 (2001).
22. N. Chernov, J. Stat. Phys. **88**, 1 (1997).

Translated by R. Tyapaev

JETP Letters, Vol. 75, No. 8, 2002, pp. 432–438. Translated from Pis'ma v Zhurnal Éksperimental'noĭ i Teoreticheskoĭ Fiziki, Vol. 75, No. 8, 2002, pp. 505–512.

Polarization Optics of Biphotons

A. V. Burlakov and M. V. Chekhova*

Faculty of Physics, Moscow State University, Vorob'evy gory, Moscow, 119899 Russia

** e-mail: postmast@qopt.phys.msu.su*

Received March 21, 2002

The works devoted to studying the polarization properties of a two-photon light generated upon spontaneous parametric down-conversion in the collinear frequency-degenerate regime are briefly overviewed, with emphasis on the studies carried out by us over a period from 1999 to 2001 within the framework of the project "Polarization Optics of Biphotons" of the Russian Foundation for Basic Research. In particular, the polarization state of a two-photon light was analyzed and its pictorial mapping onto the Poincaré sphere was proposed. The experiments on polarization transformations of a two-photon light were performed; based on these transformations, a method was suggested for ternary quantum information coding. A two-photon state with the orthogonal photon polarizations was synthesized experimentally from the two beams of identically polarized correlated photons, and the spectral properties of this state were investigated. Finally, a method was suggested for measuring the polarization state of a two-photon light in the collinear frequency-degenerate case ("tomography"). © *2002 MAIK "Nauka/Interperiodica"*.

PACS numbers: 42.50.Dv

1. INTRODUCTION

At present, two-photon fields generated, e.g., upon the spontaneous parametric down-conversion (SPDC) [1] attract attention as an example of entangled states in optics. The light radiated in the SPDC consists of so-called biphotons, namely, pairs of photons with correlated moments of creation, frequencies, wave vectors, and polarizations. The state vector of such a pair cannot be represented as the product of state vectors of individual photons (called signal and idler photons). The state vector of the light radiated in the SPDC can be written as

$$|\Psi\rangle = |0, 0\rangle + \int d\alpha F(\alpha)|\alpha\rangle|\tilde{\alpha}\rangle, \qquad (1)$$

where the variable α may stand for the frequency, wave vector, and polarization, and the states $|\alpha\rangle$ and $|\tilde{\alpha}\rangle$ are conjugate. For example, in the case of frequency expansion, these are $|\omega\rangle$ and $|\omega_p - \omega\rangle$, where ω_p is the pump frequency. The first term in Eq. (1) far exceeds the second term in amplitude and corresponds to the vacuum state, which is inevitably present in the SPDC radiation.

Of special interest is the case of collinear frequency-degenerate biphoton fields, so we will focus on this in our review. Besides being of fundamental interest, this case is also important in the context of using biphoton fields in quantum information transmission. Emphasis will be on the polarization properties of biphoton fields, because the polarization of light allows its quantum state to be formulated in terms of dichotomic variables and, thus, serves as a basis for the optical methods of quantum information transmission.

2. POLARIZATION STATES OF A BIPHOTON FIELD

Let us consider the state of a two-photon light radiated upon the collinear frequency-degenerate SPDC. For the sake of simplicity, we will consider the idealized situation where the field contains only a single spatial and spectral mode. The arbitrarily polarized state of this field has the form [2]

$$|\psi\rangle = c_1|2, 0\rangle + c_2|1, 1\rangle + c_3|0, 2\rangle, \qquad (2)$$

where $|m, n\rangle$ symbolizes the state with m photons in the polarization mode x and n photons in the orthogonal polarization mode y. The vacuum component $|0, 0\rangle$ is omitted in Eq. (2), because it is of no interest in our consideration. The first and third terms in Eq. (2) can be determined from the SPDC experiment with type-I phase matching, and the second term can be determined from SPDC with type-II matching. Due to the normalization condition $|c_1|^2 + |c_2|^2 + |c_3|^2 = 1$ and the arbitrariness in choosing the phase of the wave function, state (2) can be characterized by four real parameters d_1, d_3, φ_2, and φ_3: $c_i = d_i \exp\{i\varphi_i\}$, $\varphi_1 = 0$, $\Sigma d_i^2 = 1$, and φ_2, $\varphi_3 \in [0, 2\pi]$. Much as the polarization state of a classical polarized light can be mapped into a point on the Poincaré sphere (S^2 in R^3), the state of a two-photon light (2) can be mapped into a point on the sphere S^4 in R^5. Accordingly, the vector $\mathbf{e} = (c_1, c_2, c_3)$ can be called the biphoton polarization vector.

There is a more pictorial way for the geometric interpretation of the polarization state of a two-photon light. One can show that state (2) can be uniquely represented as

$$|\Psi\rangle = \frac{a^\dagger(\vartheta, \varphi)a^\dagger(\vartheta', \varphi')|vac\rangle}{\|a^\dagger(\vartheta, \varphi)a^\dagger(\vartheta', \varphi')|vac\rangle\|}. \quad (3)$$

Here, $a^\dagger(\vartheta, \varphi)$ and $a^\dagger(\vartheta', \varphi')$ are the operators of photon creation in an arbitrary polarization mode; for example, $a^\dagger(\vartheta, \varphi) = \cos\frac{\vartheta}{2}a_x^\dagger + e^{i\varphi}\sin\frac{\vartheta}{2}a_y^\dagger$, where $a_{x,y}^\dagger$ are the operators of photon creation in the linear polarization modes x or y, and $\varphi, \varphi' \in [0, 2\pi]$ and $\vartheta, \vartheta' \in [0, \pi]$ are, respectively, the azimuthal and polar angles on the Poincaré sphere. The transformations from $\{\vartheta, \vartheta', \varphi, \varphi'\}$ to $\{d_1, d_3, \varphi_2, \varphi_3\}$ have the form

$$d_1 = \frac{\sqrt{2}\cos(\vartheta/2)\cos(\vartheta'/2)}{\zeta}, \quad d_3 = \frac{\sqrt{2}\sin(\vartheta/2)\sin(\vartheta'/2)}{\zeta}, \quad \varphi_3 = \varphi + \varphi',$$

$$\cos\varphi_2 = \frac{\cos\varphi\sin(\vartheta/2)\cos(\vartheta'/2) + \cos\varphi'\sin(\vartheta'/2)\cos(\vartheta/2)}{d_2\zeta}, \quad (4)$$

$$\sin\varphi_2 = \frac{\sin\varphi\sin(\vartheta/2)\cos(\vartheta'/2) + \sin\varphi'\sin(\vartheta'/2)\cos(\vartheta/2)}{d_2\zeta},$$

where

$$\zeta = \sqrt{1 + \cos^2\frac{\vartheta - \vartheta'}{2} - \sin\vartheta\sin\vartheta'\sin^2\frac{\varphi - \varphi'}{2}}.$$

The inverse transformation can be written as

$$\varphi, \varphi' = \frac{\varphi_3}{2} \pm \arcsin\sqrt{\frac{2d_1d_3 - d_2^2 + \sqrt{d_2^4 + 4d_1^2d_3^2 - 4d_1d_3d_2^2\cos(2\varphi_2 - \varphi_3)}}{4d_1d_3}},$$

$$\vartheta, \vartheta' = \arccos\frac{d_1^2 - d_3^2 \pm 2\sqrt{[d_2^2 - d_1d_3\cos(2\varphi - \varphi_3)]^2 - d_1^2d_3^2}}{1 + d_2^2 - 2d_1d_3\cos(2\varphi - \varphi_3)}. \quad (5)$$

Therefore, every state of the degenerate biphoton field can be mapped into two points on the Poincaré sphere and specified by four parameters θ, θ', φ, and φ'. For example, the state $|2, 0\rangle$ is mapped into a "double" point on the sphere, and the state $|1, 1\rangle$ is mapped into two points at the opposite ends of the same diameter (Fig. 1). The Stokes vector of a biphoton light is equal to the sum of Stokes vectors **S**, **S**' of, respectively, the states $a^\dagger(\vartheta, \varphi)|vac\rangle$ and $a^\dagger(\vartheta', \varphi')|vac\rangle$, and the degree of polarization is equal to the cosine of the half-angle between the vectors **S** and **S**'.

3. POLARIZATION TRANSFORMATIONS OF A BIPHOTON FIELD

The arbitrary polarization transformations of state (2) belong to the Lie group $SU(3)$ and are specified by eight parameters [2]. These transformations cannot be accomplished by the linear polarization transformers that are ordinarily used in the experiment (phase plates or their combinations, rotators, interferometers, etc.), because these transformers correspond to the $SU(2)$ group and are characterized by only three parameters. This is clearly seen from Fig. 1; the above-mentioned transformations can be represented as the simultaneous rotation of both points on the Poincaré sphere so that they do not change the relative positions of the points. However, the transformations of this type can easily be implemented experimentally. This was accomplished in [3], where, from all states of (2), three mutually orthogonal states

$$|\Psi_+\rangle = \frac{|2, 0\rangle + |0, 2\rangle}{\sqrt{2}} \equiv |+, -\rangle,$$

$$|\Psi_-\rangle = \frac{|2, 0\rangle - |0, 2\rangle}{\sqrt{2}} \equiv |+45°, -45°\rangle, \quad (6)$$

$$|\Psi_0\rangle = |1, 1\rangle \equiv |x, y\rangle.$$

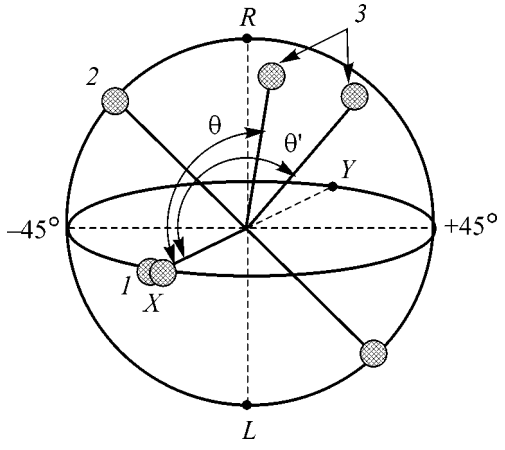

Fig. 1. Mapping of the state (3) of an arbitrarily polarized biphoton (two correlated arbitrarily polarized photons) onto the Poincaré sphere. (*1*) Is the $|2, 0\rangle$ state, i.e., a pair of correlated photons linearly polarized along the X axis; (*2*) is the state of two correlated orthogonally polarized photons; and (*3*) is the biphoton state with an arbitrary polarization.

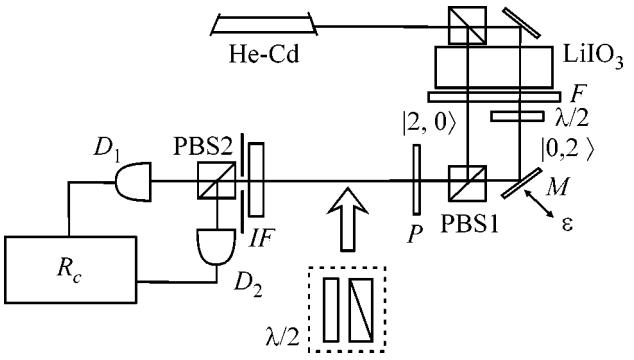

Fig. 2. Scheme of the experiment on polarization transformations of a biphoton field. The pump radiation is led into the interferometer through a nonpolarizing beam splitter. Crystal $LiIO_3$ is placed in both interferometer arms. Filter *F* suppresses the pump radiation. A λ/2 plate in one of the arms turns the polarization through 90°. Mirror *M* is equipped with a piezoelectric feed; its displacement changes the phase between the $|2, 0\rangle$ and $|0, 2\rangle$ components of the biphoton state vector at the interferometer output. Beam splitters PBS1 and PBS2 are polarizing; the first of these delivers, without loss, the $|2, 0\rangle$ and $|0, 2\rangle$ biphotons to the interferometer output channel, and the second measures the correlation between the numbers of photons in the *X* and *Y* modes [$|c_2|^2$ in the state (2)]. Phase plate *P* accomplishes the polarization transformations. The interference filter *IF* and the aperture select the collinear frequency-degenerate scattering. The block in the bottom of the figure serves for measuring $|c_1|^2$ and $|c_3|^2$ in the state (2).

were chosen. They are depicted in Fig. 1 by the pair of points at the opposite ends of the diameter; the degree of polarization is zero for all these states, and they can be transformed into each other using linear polarization elements. The first of these states corresponds to a pair of photons, one of which is right-hand circularly polarized and the other is left-hand polarized. The second state corresponds to a pair of photons, one of which is linearly polarized at an angle of 45° to the *X* axis and another is polarized at an angle of –45° to the *X* axis. The third state corresponds to a pair of photons polarized, respectively, along the *X* and *Y* axes. It has been demonstrated in [3] that this state can be obtained from the Ψ_+ or Ψ_- state. The scheme of the corresponding experiment is shown in Fig. 2. The cw pumping (helium–cadmium laser radiation with a wavelength of 325 nm) is fed into the input of an interferometer with a lithium iodate crystal in both its arms. The SPDC with collinear type-I phase matching in the crystal produces two-photon radiation in the $|2, 0\rangle$ state in both arms. After the crystal, the pump radiation is cut off by a filter. A half-wave plate in one of the arms turns the polarization through 90° to transform the beam state into $|0, 2\rangle$, and both beams impinge, without loss, on a polarizing beam splitter PBS1. Mirror *M* in the interferometer can be shifted using a piezoelectric feed, so that the biphoton field at the interferometer output is

$$|\Psi\rangle = \frac{|2, 0\rangle + e^{i\varepsilon}|0, 2\rangle}{\sqrt{2}}, \qquad (7)$$

where the phase ε can be changed by shifting mirror *M*. The state Ψ_+ or Ψ_- is produced if, respectively, ε = 0 or π. This state is converted to Ψ_- using the appropriate phase plate *P* (λ/4 plate oriented at an angle of π/4 in the first case, and λ/2 plate oriented at an angle of π/8 in the second case). The resulting state is detected by a polarizing beam splitter PBS2 and a pair of photodetectors (avalanche photodiodes) D_1 and D_2, from which the photocurrent pulses are led to a photocount coincidence circuit. The coincidence counting rate is proportional to $|c_2|^2$ [see Eq. (2)]. The completeness of the transformation (for certain plate positions, the states $|2, 0\rangle$ and $|0, 2\rangle$ are absent at the output) can be checked as follows. If a special unit consisting of an *X*(*Y*)-polarizing polaroid and a π/8 half-wave plate are placed ahead of the beam splitter, the coincidence counting rate will be proportional to $|c_1|^2$ ($|c_3|^2$). The number of coincidences obtained in the experiment is given in Fig. 3 as a function of the angle of plate rotation. One can see that, for the plate positions corresponding to the maximum of $|c_2|^2$, $|c_1|^2$ drops practically to zero. Note that the phase ε is fixed and equal to π for both curves shown in Fig. 3. To demonstrate the dependence of state (7) on the phase ε, measurements were also made with a fixed position of plate *P* and a fixed displacement of mirror *M*. The resulting curve is shown in Fig. 4.

The setup shown in Fig. 2 was used to synthesize, without loss, "type-II biphotons," i.e., pairs of correlated, orthogonally polarized photons, from the two beams of type-I biphotons, i.e., pairs of identically polarized photons. It should be noted that the two-photon light in this experiment was weak to the extent that the different photon pairs, radiated at random time instants, practically never overlapped at the interferometer output. The observed effect was a manifestation of the two-photon interference or "the interference of independent biphotons" [4]: if the two-photon light is produced in two different regions illuminated by the coherent pumping, the probability amplitudes of pair creation may either add to or be subtracted from one another. Interestingly, this effect can be observed even if the interferometer arms in Fig. 2 are not balanced to within the coherence length of two-photon light, as it should with classical interference. For example, the difference in arm lengths in the experiment was 2 cm, while the SPDC radiation coherence length was about 20 μm. The only necessary condition is that the difference in arms should not exceed the pumping coherence length (in our case, about 15 cm).

The states Ψ_+, Ψ_-, and Ψ_0, like the states $|2, 0\rangle$, $|1, 1\rangle$, and $|0, 2\rangle$, form the orthogonal basis in the space of biphoton polarization states. They can easily be

transformed into each other using the phase plates; as indicated above, a half-wave plate set at an angle of 22.5° to the X axis transforms Ψ_- into Ψ_0, while the quarter-wave plate set at an angle of 45° to the X axis transforms Ψ_+ into Ψ_0. The transformation from Ψ_+ to Ψ_- is accomplished by a quarter-wave plate set at an angle of 0° to the X axis.

The analogous orthogonal basis can be constructed in the space of polarization states (2). The elements of this basis transform into each other using only a single phase plate. Such basis states were obtained in [5]; they are also related to the nonpolarized states and corresponded to the pairs of orthogonally polarized photons (in Fig. 1, they would be mapped into diametrically opposite points on the sphere).

Based on the polarization states of two-photon light (6) and their transformations, one can develop a ternary code for quantum information transmission. This would increase the density of quantum information recording, as compared to the standard qubit coding. If the information is coded using biphotons, whose state is given by Eq. (2) in the three-dimensional space and, hence, is analogous to a three-level system or a particle with spin 1, then N biphotons (qutrits) will encompass not 2^N states, as in the case of N qubits, but 3^N states. The qutrit coding was first demonstrated in [6], though for the nondegenerate (two-beam) SPDC. The single-beam regime is more convenient for quantum information transmission, because it allows one to pass both correlated photons through the same optical fiber. A possible scheme of quantum cryptography based on the ternary coding was suggested in [7].

In [8], the anticorrelation effect was observed for synthesized type-II biphotons. The idea of this effect (which was first observed in [9]) is as follows. The signal and idler photons radiated into different spatial or polarization modes (their frequencies must necessarily be identical) are led to different inputs of a 50% beam splitter. At the outputs of the beam splitter, two detectors, D_1 and D_2, are placed together with the coincidence circuit, so that the coincidence may occur upon the detection of an idler photon by the detector D_1 and a signal photon by the detector D_2 or vice versa. Due to the interference of the corresponding probability amplitudes, the coincidence counting rate drops virtually to zero (more precisely, to the counting rate of accidental coincidences) upon balancing optical paths of the signal and idler photons before the beam splitter. In [9], it was suggested that this effect be used for measuring short group delays between photons. The coincidence counting rate R_c as a function of the time delay τ between the signal and idler photons before the beam splitter takes the form of a "dip" given by the expression [8]

$$R_c \sim 1 - \left|g^{(1)}(2\tau)\right|, \qquad (8)$$

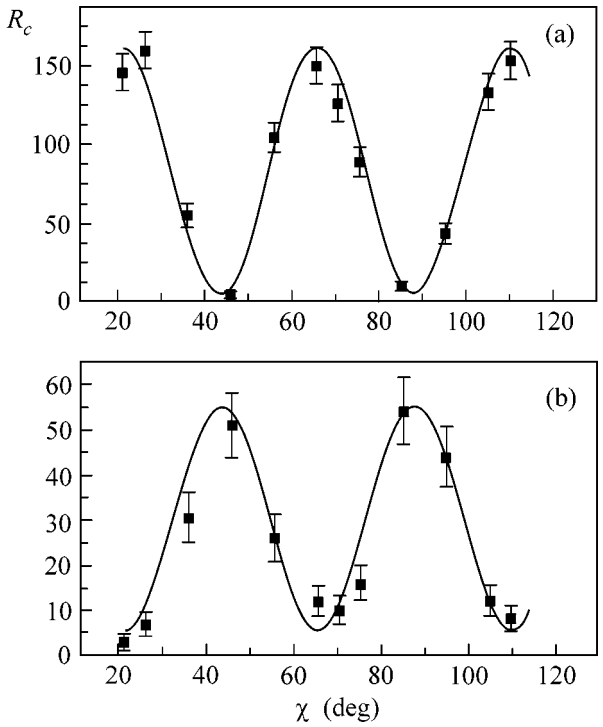

Fig. 3. Plots of the number of coincidences in the scheme shown in Fig. 2 against the rotation angle of the λ/2 plate: (a) without the additional block ($|c_2|^2$ is measured); (b) with the additional block, in which the polarizer selects the X polarization ($|c_1|^2$ is measured).

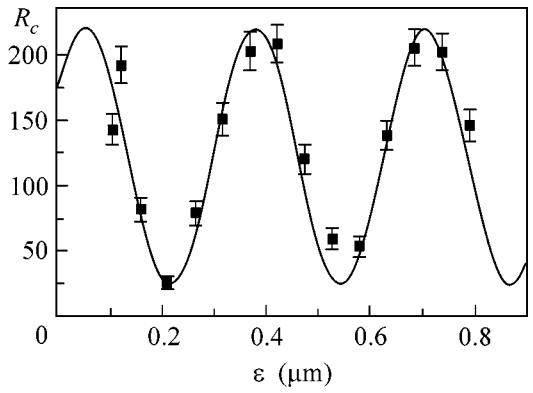

Fig. 4. Plot of the number of coincidences in the scheme shown in Fig. 2 against the displacement of mirror M.

where $g^{(1)}(\tau)$ is the first-order correlation function of the two-photon light. Inasmuch as this function is determined only by the spectrum, the dip shape depends only on the spectrum of two-photon light. As a result, the anticorrelation effect for the $|1, 1\rangle$ state synthesized from the $|2, 0\rangle$ and $|0, 2\rangle$ states shows itself as a narrow dip, as in the case of type-I biphoton light (as a rule, the spectrum for the type-I phase matching is broader than for the type-II matching). However, if the anticorrela-

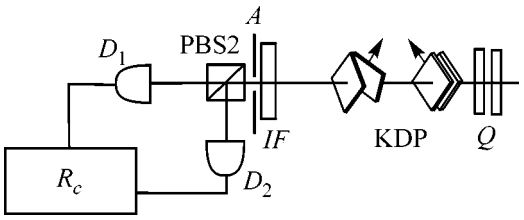

Fig. 5. Scheme for measuring the shape of an anticorrelation dip in the $|1, 1\rangle$ state synthesized from the $|2, 0\rangle$ and $|0, 2\rangle$ states. The optical axes of quartz plates Q are set at an angle of 45° to the X axis; four KDP plates are oriented so that they do not introduce, in the absence of rotation, delay between photons linearly polarized at 45° to X. The rotation of the plate pair allows smooth variation of this delay.

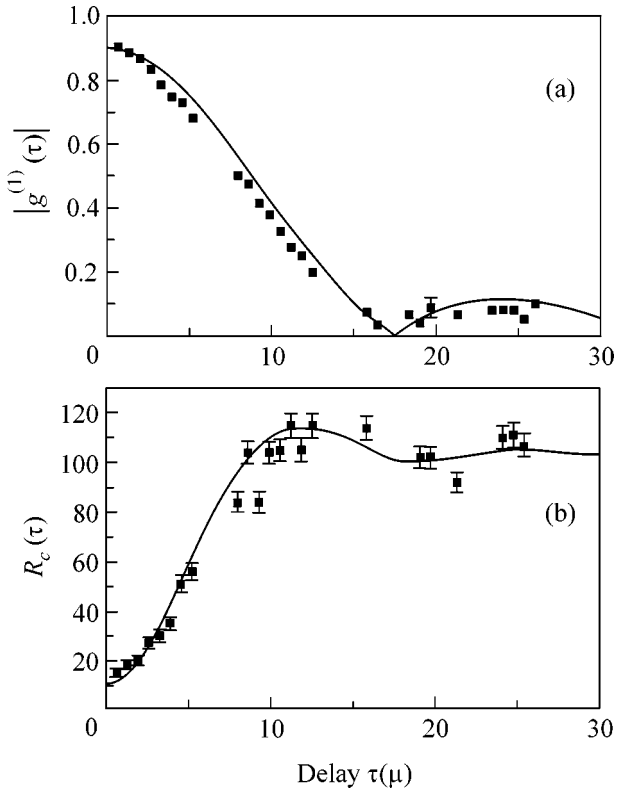

Fig. 6. The shapes (a) of the first-order correlation function and (b) of the anticorrelation dip for the synthesized $|1, 1\rangle$ state.

tion effect is observed for the synthesized state with orthogonally polarized twin photons, the time delay τ can be introduced by the polarization method, which can be done much easier than in the case of different spatial modes.

In [8], the anticorrelation effect was observed by slowly changing the delay between the signal and idler photons of a pair in the state ψ_- using four KDP plates of thickness 1.17 mm, two of which were fixed (their optical axes were oriented at an angle of 45° to the X axis), while the other two plates could be rotated about their optical axes tilted at an angle of –45° to the X axis (Fig. 5). In addition, the delay could be introduced discretely using crystal quartz plates.

Because measurements were performed for the photon pairs in the state ψ_- (linearly polarized at 45° to the X axis), the polarizing beam splitter passed or reflected each of the twin photons with a probability of 50%; i.e., the conditions for the observation of the anticorrelation effect were fulfilled. The coincidence counting rate was measured as a function of delay τ (Fig. 6). To check relationship (8), the first-order correlation function $g^{(1)}(\tau)$ was also measured. To do this, one of the interferometer arms was shut off, and the system of quartz and KDP plates functioned as a polarization interferometer for the horizontally polarized radiation from another arm. The signal intensity detected by each of the detectors showed an interference pattern upon turning the KDP plates. The value of $|g^{(1)}(\tau)|$ was determined from the visibility of the interference pattern. The results of measurements are shown in Fig. 6. The solid line corresponds to the theoretical curve constructed using Eq. (8); the function $|g^{(1)}(\tau)|$ was calculated as a Fourier transform of the SPDC spectrum, which, in turn, was calculated on the basis of the parameters of lithium iodate crystal.

One can see that, in accordance with Eq. (8), the anticorrelation dip is twice as narrow as $|g^{(1)}(\tau)|$. For a lithium iodate crystal of length 15 mm, its width was 30 fs.

4. POLARIZATION TOMOGRAPHY OF A BIPHOTON FIELD

To determine the polarization state of biphoton field (2), standard polarization measurements, such as, e.g., the measurement of Stokes parameters, are insufficient. The state of biphoton light (2) is primarily characterized by the fourth moments with respect to the field. As shown in [10], complete information about the fourth moments of polarized light is contained in the so-called fourth-order coherence matrix

$$K_4 = \begin{pmatrix} A & D & E \\ D^* & C & F \\ E^* & F^* & B \end{pmatrix},$$

whose elements are the normally ordered fourth moments of the form

$$A \equiv \langle a_x^{\dagger 2} a_x^2 \rangle, \quad B \equiv \langle a_y^{\dagger 2} a_y^2 \rangle, \quad C \equiv \langle a_x^\dagger a_y^\dagger a_x a_y \rangle,$$

$$D \equiv \langle a_x^{\dagger 2} a_x a_y \rangle, \quad E \equiv \langle a_x^{\dagger 2} a_y^2 \rangle, \quad F \equiv \langle a_x^\dagger a_y^\dagger a_y^2 \rangle.$$

Here, A, B, and C are real and D, E, and F are complex numbers. In the general case of a mixed biphoton field state, all nine real numbers specifying this matrix must be known (if the total number of photons or the total

energy is known, it is sufficient to know eight numbers). However, for the pure state (2), it is sufficient to know only the three real elements A, B, and C and any two of the complex elements D, E, and F [2]. For example, if A, B, C, D, and F are known, then the parameters of state (2) are expressed as follows:

$$d_1^2 = \frac{A}{A+B+2C}, \quad d_3^2 = \frac{B}{A+B+2C},$$
$$d_1 d_2 e^{i\varphi_2} = \frac{\sqrt{2}D}{A+B+2C}, \tag{9}$$
$$d_3 d_2 e^{i(\varphi_3-\varphi_2)} = \frac{\sqrt{2}F}{A+B+2C}.$$

The mixed state of a biphoton field can be imagined as the classical fluctuations of amplitudes c_i in Eq. (2). To describe such a state, one should use the density matrix whose nine elements are in one-to-one correspondence with the elements of K_4.

In [11], a set of 16 measurements was suggested for the characterization of a *double-mode* biphoton field.[1] Note that the matrix, whose elements were measured in [11], transforms into the matrix K_4 from [10] after passing to the single-mode description. Following [11], one can propose a scheme for measuring the polarization state of a single-mode two-photon light (Fig. 7). In this scheme, a biphoton beam is first divided into two beams using a nonpolarizing beam splitter, whereupon the measurements analogous to those suggested in [11] are performed for the two output beams: for each of them, the combination of a half-wave plate, quarter-wave plate, and a vertically oriented linear polarizing filter is mounted. Then, for a certain set of plate positions, the coincidence counting rate is measured for the photocounts of two detectors placed behind the polarizing filters. However, because of the symmetry of both beams (due to the single-mode character of two-photon light) and also because one is dealing with a pure (rather than mixed) state, it suffices to perform only seven measurements instead of sixteen, as was suggested in [11].[2] A full set of measurements is given in the table, where the plate orientations and the measured quantities are presented. Note that this set is not unique; when choosing measurements, we tried to ensure that the measured correlation function would contain the smallest possible number of elements of the coherence matrix. One can see that only one quarter-wave plate and two half-wave plates are sufficient for the full set of measurements, or, if the polarizers can be rotated, it is sufficient to place only one quarter-wave plate for one of the beams.

Note that, although the pure polarization state of a beam is characterized only by four parameters, polarization tomography involves seven measurements rather than four. This is due to the fact that, first, the total number of biphotons is unknown, so that this number $(A + B + 2C)/2$ should also be measured, and the result should be normalized to it. Second, it is seen from the table that each of the last four measurements yields either the real or the imaginary part of the complex quantities F and D, which corresponds to the cosines or sines of phases in state (2). Since the phases φ_2 and φ_3 are defined on the interval $[0, 2\pi]$, one must know both the cosines and sines of these phases.

If the biphoton-field state is mixed, then the set of measurements listed in the table should be comple-

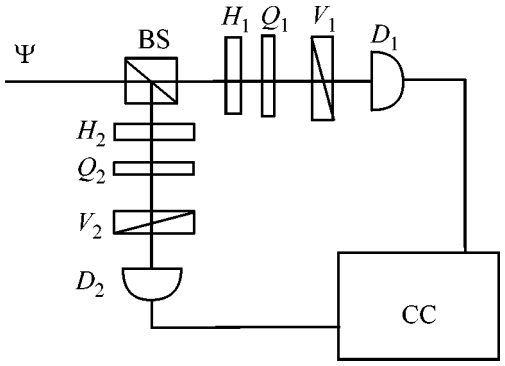

Fig. 7. Scheme of a setup for the polarization tomography of a single-mode biphoton light. A nonpolarizing beam splitter BS divides the input beam into two output beams. In each of them are placed one half-wave plate (H_1, H_2), one quarter-wave plate (Q_1, Q_2), and a polarizing filter transmitting only the vertically polarized light (V_1, V_2). Detectors D_1 and D_2 detect the radiation of output beams, and their output signals are fed into the coincidence circuit CC. The coincidence counting rate, as measured at different positions of the phase plates (table), allows a full set of biphoton field parameters to be measured (2).

Set of measurements in polarization tomography of the state of single-mode biphoton light

Measurement no.	Position				Measured quantity
	H_1	Q_1	H_2	Q_2	
1	0°	0°	0°	0°	B
2	45°	0°	45°	0°	A
3	45°	0°	0°	0°	C
4	22.5°	0°	0°	0°	$\frac{1}{2}(B + C - 2\mathrm{Re}R)$
5	0°	45°	0°	0°	$\frac{1}{2}(B + C - 2\mathrm{Im}F)$
6	45°	0°	22.5°	0°	$\frac{1}{2}(A + C - 2\mathrm{Re}D)$
7	0°	45°	45°	0°	$\frac{1}{2}(A + C - 2\mathrm{Im}D)$

[1] To pass from a single-mode to a double-mode description, it suffices to assume that the signal and idler photons either have different frequencies or their scattering angles are different.

[2] For a mixed single-mode state, nine measurements is required.

mented by two measurements corresponding to the real and imaginary parts of the moment E.

5. CONCLUSIONS

This article is a brief overview of the works carried out from 1999 to 2001 within the framework of the Russian Foundation for Basic Research (project no. 99-02-16419 "Polarization Optics of Biphotons"). The related problems have also been discussed in this work. We have considered the polarization state of a two-photon light in single spatial and frequency modes, as well as the transformations and measurements of this state. As a prospect for further investigations, one may suggest the generalization to the case of the mixed state of a biphoton field. The study of the polarization state of a multiphoton light of interest is also. Finally, the fundamental results can serve as a basis for applied developments; for instance, the possibility of using polarization states of a biphoton light in designing ternary quantum cryptographic protocols are being discussed.

We are grateful to S.P. Kulik and A.A. Zhukov for discussions. This work was supported by the Russian Foundation for Basic Research (project nos. 99-02-16419 and 00-15-96541).

REFERENCES

1. D. N. Klyshko, *Photons and Nonlinear Optics* (Nauka, Moscow, 1980).
2. A. V. Burlakov and D. N. Klyshko, Pis'ma Zh. Éksp. Teor. Fiz. **69**, 795 (1999) [JETP Lett. **69**, 839 (1999)].
3. A. V. Burlakov, M. V. Chekhova, O. A. Karabutova, *et al.*, Phys. Rev. A **60**, R4209 (1999).
4. A. V. Burlakov, D. N. Klyshko, S. P. Kulik, and M. V. Chekhova, Pis'ma Zh. Éksp. Teor. Fiz. **69**, 788 (1999) [JETP Lett. **69**, 831 (1999)].
5. B. T. Tsegaye, J. Söderholm, M. Atature, *et al.*, Phys. Rev. Lett. **85**, 5013 (2000).
6. K. Mattle, H. Weinfurter, P. G. Kwiat, and A. Zeilinger, Phys. Rev. Lett. **76**, 4656 (1996).
7. H. Bechmann-Pasquinucci and A. Peres, Phys. Rev. Lett. **85**, 3313 (2000).
8. A. V. Burlakov, M. V. Chekhova, O. A. Karabutova, and S. P. Kulik, Phys. Rev. A **64**, 041803(R) (2001).
9. C. K. Hong, Z. Y. Ou, and L. Mandel, Phys. Rev. Lett. **59**, 2044 (1987); Y. H. Shih and C. O. Alley, Phys. Rev. Lett. **61**, 2921 (1988).
10. D. N. Klyshko, Zh. Éksp. Teor. Fiz. **111**, 1955 (1997) [JETP **84**, 1065 (1997)].
11. D. James, P. Kwiat, W. Munro, and A. White, Phys. Rev. A **64**, 052312 (2001).

Translated by V. Sakun